NORTHWESTERN UNIVERSITY

# Large-Strain Deformation Mechanics of Charge-Containing Polymer Membranes

A DISSERTATION

SUBMITTED TO THE GRADUATE SCHOOL

IN PARTIAL FULFILLMENT OF THE REQUIREMENTS

for the degree

DOCTOR OF PHILOSOPHY

Field of Materials Science and Engineering

By

Shawn H. Chen

EVANSTON, ILLINOIS

September 2018

# Abstract

Large-Strain Deformation Mechanics of Charge-Containing Polymer Membranes

Shawn H. Chen

The use of polymeric membranes have become ubiquitous in our daily lives. From simple chip bags to million-dollar cockpits, these membranes find diverse applications in packaging, protective coating, electronic device, gas and liquid separation, and medicine. The 2-dimentional geometry of the membranes offered unique mechanical and interfacial properties that often surpass those in their bulk counterparts. While the diminishing dimensions of the membranes provide enhanced materials properties and superb versatility for wide-reaching applications, they also bring forth new challenges in the characterization and design of novel membrane systems.

The primary focus of this dissertation is the development of novel methods to robustly characterize the mechanical properties of polymer thin films relevant to the application context. This work begins with a brief discussion on the current research on charge-containing polymers. An examination on the development of a non-traditional biaxial inflation mechanical test is subsequently introduced, and marks the foundation of this work. A series of sulfonated pentablock copolymers used for water purification is thoroughly investigated using a combination of X-ray scattering, biaxial inflation, and transport experiments. It is found that the softening effect of polymer sulfonation can be mitigated by reducing the volume fraction of the charged domain without detrimentally affecting transport properties. Additionally, membrane compliance can be further reduced by increasing the packing density

of the uncharged domains. Process-dependent membrane morphology of these pentablock copolymers is explored using x-ray scattering techniques. Water transport properties were found to be independent of membrane morphology, and guides our understanding of the processing-structure-property relationships in these block ionomers.

Next, a polyelectrolyte complex coacervate system was investigated to provide a better understanding of charge effects on the mechanical strength and relaxation behavior of complex network systems in low-salt environments. At these limiting conditions, the deformation behavior deviates from those predicted by the time-temperature and time-salt superposition methods. A fractional model used to describe power-law relaxation behavior is introduced, and the effect of counter ions on charge-pair interactions in a transient network system is discussed.

Finally, the mechanics of polycarbonate thin films were investigated using a combined wrinkling-cracking methodology to provide insight into ductile fracture behavior of polymer bi-layers that are geometrically relevant for flexible electronics. The supported bi-layer structure enables the distribution of stress across the entire sample well after reaching the critical fracture strain, and minimizes the propagation of cracks. The findings here can better inform future design and optimization of materials for protective coatings, impact mitigation, and wearable electronics.

# Acknowledgments

First and foremost, to my advisor, Prof. Ken Shull: Without your patience, guidance and unwavering support, I would not be here today. Thank you for being available whenever I knocked on your doors, and for stimulating conversations when I needed encouragements while allowing me to explore my interests independently. I truly appreciate your wisdom, thoughtfulness, positive outlook, and infinite patience. These are qualities I will continue to strive for beyond my graduate career.

To my committee members: Prof. Wesley Burghardt, Prof. David Dunand, and Dr. Zhang Jiang, for their insightful discussions, coursework, and guidance.

To my mother, Shelley for your love and support in all my pursuits, and for trusting me to make my own decisions; my brother and sister-in-law, Johnson and Katy, for being my home away from home and making sure I was well nourished.

I am thankful for all of the Shull group members, both past and present: Chya Yan, Elizabeth, Lauren, Lindsay, and Madeline, thank you all for welcoming me into the group in my first year, and for sharing your group wisdom and advice. Evan, thank you for being patient in answering all of my novice MATLAB and math questions although we've never met in person, and for laying a solid foundation for me to build much of my work. Yaoyao, thank you for all the invaluable scientific discussions in the office, and for being such a joy to work with in the lab. Kazi, thank you for inspiring me with your tireless work ethics, and for the weekend road-trip from Florida. Qifeng, thank you for being a wealth of knowledge on all things lab related, and for listening to all of my research ideas and helping me find the right solution when challenges arose. David, Matt, Meredith, and Tom, for keeping the lab tidy and the office full of life. We may complain about being crowded at times, but I will miss all the jokes, the lively conversations, and cookies we've shared. I hope I had left a positive grad school experience for you the same way my predecessors did for me. Josh,

thank you for being the calm and light in my moments of stress and doubt (and for being there for all the fun parts, too). I will cherish all the adventures we've shared massacring valentine lobsters, riding our bikes through the pothole-ridden streets of Chicago, tasting art on a plate (or no plate), punching the snot out of each other during the Krav Maga test, and countless home-made hot-pots.

To all of my other mentors and collaborators: Dr. Edwin Chan at NIST, for your mentorship and career advice; To Steven Weigand, Joseph Strzalka, and the rest of the staff at Sectors 5 and 8 at the Advanced Photon Source, for their help and expertise with x-ray experiments and analysis; to Dr. Bruce Lindvall, for striving to make the lives of all grad students better. I would also like to extend my appreciation to the wonderful staff in the MatSci department office for all their work in keeping the department running strong.

Lastly, I would like to thank my friends at Northwestern, without whom my life would have been much more stressful: Sam, Dolo, Gavin, Stephanie, and Patrick, for sharing your valuable lunch time and grad school wisdom with me; Say, Hayk, Charlotte, and Amit for the endless hilarity, BBQ, and impromptu dance parties. To my roommates: Karl, my oldest* friend at grad school, for listening, going on walks, and toxic baking; Sarah, for your thoughtfulness, kindness, and tenacity, and for commiserating with me during my low points; Shay, for providing me with a much needed break with a game or two. To the Crew: Garrett, thank you for not being afraid to ask the difficult (and sometimes weird) questions, both in lab and in life; Ha-Kyung, thank you for being a role model, a confidant, and a source of encouragement and positivity; Karen, without your love and support this dissertation would not have been possible. Thank you for being my support system, and for being there through all the trials and triumphs. Truly, the most memorable experiences are ones that are shared, and I'm glad I got to share it with you all.

This work was funded by a NSF Polymers Program grant (DMR-1410968) and under the financial assistance of an award 70NANB14H012 from U.S. Department of Commerce,

National Institute of Standards and Technology as part of the Center for Hierarchical Materials Design (CHiMaD). Additionally, this work made use of the following resources: Keck-II facility of the NUANCE Center at Northwestern University, which has received support from the Soft and Hybrid Nanotechnology Experimental (SHyNE) Resource (NSF NNCI-1542205); the MRSEC program (NSF DMR-1121262) at the Materials Research Center; the International Institute for Nanotechnology (IIN); the Keck Foundation; and the State of Illinois, through the IIN; the Advanced Photon Source, a U.S. Department of Energy (DOE) Office of Science User Facility operated for the DOE Office of Science by Argonne National Laboratory under Contract No. DE-AC02-06CH11357; the DuPont-Northwestern-Dow Collaborative Access Team (DND-CAT) located at Sector 5 of the Advanced Photon Source (APS). DND-CAT is supported by Northwestern University, E.I. DuPont de Nemours & Co., and The Dow Chemical Company.

# Contents

# List of Tables

# List of Figures

# Chapter 1

# Introduction

## 1.1 Research Overview

The goal of this work is to provide insight on the mechanical properties of thin film materials under conditions often overlooked, and to apply experimental treatment that are relevant in the context of membrane application. Although many engineering mechanical tests available today can overcome the limitations of characterizing thin films, this research aims to further elucidate the nonlinear mechanical response and creep behavior of thin films, and to examine the effects of solvent quality, charge concentration, and polymer morphology.

With this in mind, Chapter 2 opens with a general overview of ion-exchange membranes (IEMs), with specific considerations as charge-containing polymers for water treatment applications. Subsequently, the large strain deformation theory is discussed to pave the groundwork for a significant part of this work.

Chapter 3 provides an examination of a non-traditional biaxial inflation mechanical test central to this research. A series of sulfonated pentablock copolymers is thoroughly investigated using a combination of swelling, biaxial inflation, and transport experiments as a function of block size, block chemistry, and sulfonation level. Process-dependent membrane morphology of these pentablock copolymers is further explored in Chapter 4. Grazing-incidence small-angle X-ray scattering (GISAXS) and Small-angle X-ray scattering (SAXS) were used to characterize the morphology and the average distance between charge centers as a function of solvent species. Correlation between the structural results from the X-ray experiments with transport properties reveal the transport mechanism in these materials and nuances in material processing.

Chapter 5 builds upon the membrane mechanical test developed in Chapter 3 to characterize the mechanical response of polyelectrolyte thin films in salt-containing aqueous media. Biaxial inflation enables the characterization of polyelectrolyte complex relaxation at the low-salt regime . The experimental results were modeled using fractional Maxwell model to better predict the relaxation behavior of these complex network solids at the limit of low-salts.

Finally in Chapter 6, I discuss a collaborative project with Dr. Edwin Chan at the National Institute of Standards and Technology, in which I explore ductile fracture behavior of polycarbonates using a combined wrinkling and cracking methodology. The mechanisms of ductile fracture in polymers is still not well understood. The goal of the research project is to better understand key mechanical properties such as stiffness, strength, and ductility to provide design guidelines for mechanically strong and fracture-resistant engineering materials. A combined wrinkling–cracking (WC) methodology is employed to characterize the elastic and fracture properties of a stiff film deposited onto an elastomeric substrate. Taking advantage of the elastic mismatch between a rigid coating and a soft substrate, this technique captures the mechanical properties of ultra-thin ($<$ 200 nm) films. Here, the mechanical properties of polycarbonate (PC) thin films are characterized as a function of film thickness.

While a large portion of this thesis focuses on the characterization of charge-containing materials for water treatment applications, the findings presented here highlight the many creative approaches in material characterization that can be extended to studying a multitude of material systems.

# Chapter 2

# Background

The first half of this thesis focuses on the mechanical characterization of charge-containing polymers membranes in aqueous environments that are relevant to material applications. Consequently, this chapter will provide a brief overview of ion-exchange membranes (IEMs), with specific considerations as charge-containing polymers for water treatment applications. Subsequently, the large strain deformation theory is discussed to pave the groundwork for a significant part of this work, building on the previous work of large strain deformation of Dr. Evan Laprade and Dr. Rong Long. An equibiaxial membrane inflation characterization technique will also be introduced.

## 2.1 Ion-Exchange Membranes

Ion exchange membranes (IEMs) have evolved significantly in the recent decade[1–5] from simple materials in the laboratory to industrial products with significant commercial success and impact, such as Nafion used in fuel cells[1,6–8]. IEMs use further extends into the desalinization of sea water, gas separation, and chemical recovery in industrial effluents, to name a few[9–12]. In many cases, IEMs transport ions across a conductive polymeric membrane while blocking the passage of water or other solvents. Most of these applications require operation in liquid environments, which can lead to membrane swelling and other irreversible changes to the mechanical strength of the membrane[13–15].

There are two basic types of ion-exchange membranes: anion exchange membranes (AEMs) and cation exchange membranes (CEMs). Anion exchange membranes are semipermeable membranes generally made from ionomers and designed to conduct anions while being impermeable to gases such as oxygen or hydrogen. Their primary applications include

fuel recovery and gas separation in which separation of reactants and transport of anions is necessary. AEMs are that are based on quaternary ammonium groups and hydrocarbon polymer backbone have good resistance against oxidation, chlorine, and alkali degradation, but they suffer from $CO_2$ poisoning, and typically have lower thermostability and ion conductivity compared to CEMs. Cation exchange membranes, also known as proton exchange membranes (PEMs) are electrolyte or ionomeric materials that allow only the transport of protons, the primary function of proton exchange membrane fuel cells and water electrolyzers. These membranes are commonly used in water treatment and automotive, stationary and portable power as solid electrolyte in electrochemical cells that require selective transport of cations across the cell junction[9]. PEMs that are based on fluorinated polymer and sulfonic acid groups such as Nafion dominate the market for proton exchange membrane fuel cells (PEMFC) because of their excellent proton conductivity and durability. In this work, we will focus primarily on proton exchange membranes.

Although the ionic conductivity of proton exchange membranes are of the utmost importance to when considering product performance, the mechanical properties of these membranes which are often overlooked play a significant role in membrane performance and longevity[3,16]. Reducing swelling induced volume change is required for improved cyclability and device endurance[17]. Roughness and local charge effects can also affect the efficiency of the membranes. In particular, wastewater treatment membranes are susceptible to biofouling and particle build-up, which drastically reduce water flux[18–21]. So not only do these membranes need to maintain high ionic conductance, but they also need to have high mechanical strength to support large pressure differentials in many separation processes, as well as good resistance against fouling, poisoning and other reactive chemical intermediates used during separation[9,22].

There is significant interest in the development and improvement of hydrocarbon based PEMs for widespread commercialization due to the following reasons: Firstly, perfluorinated

Nafion is expensive; if a non-fluorinated polymer electrolyte that employ a cheaper sulfonated polymer backbone is used, a huge cost reduction can be attained. Secondly, the design, operating conditions, and process control all depend on the type of PEMs used. A hydrocarbon based PEM can enable the applications of PEMs in new fields.

### 2.1.1 Relevant Parameters for PEMs

Before a detailed discussion of potential ion-exchange membrane systems, it is necessary to define some terminologies relevant to the evaluation of these materials. In this section, the definitions and measurement methods of conductivity, permeability, water uptake, and ion exchange capacity (IEC) will be presented. Depending on the designed application, the performance of a membrane can be described by its ionic conductivity or solvent permeability. A simple method was devised by Zawodzinski and coworkers[23,24] by which a membrane was in between two electrodes and a value of resistance was measured. The conductivity can be calculated from the measured resistance following:

$$\sigma = \frac{L}{AZ'} \tag{2.1}$$

where L is the distance between electrodes, A is the cross sectional area of the membrane, and Z' is the real contribution of the impedance response. Although this measurement captured only the in-plane conductivity as opposed to the through-plane conductivity that is perhaps more relevant to actual operation, this simple method nevertheless acted as a preliminary screening test for new material systems.

For PEMs designed for water transport and treatment, water permeability or flux is commonly used to benchmark membrane performance[25–27]. Most fundamentally, the diffusion

of the liquid through a membrane can be described using Darcy's Law for permeability[28]:

$$\kappa = \frac{\mathrm{Q d_m}}{\mathrm{A} \Delta \mathrm{P V_m}} \tag{2.2}$$

where $\kappa$ is the coefficient of permeability (moles/m$\cdot$ s$\cdot$ Pa), Q is the volumetric flow rate ($\mathrm{m^3/s}$), A is the surface area of the liquid transport ($15\,\mathrm{cm^2}$), $\mathrm{V_m}$ is the molar volume of liquid water ($18\,\mathrm{cm^3/mole}$), $\Delta$P is the applied pressure difference, and $\mathrm{d_m}$ is the hydrated membrane thickness. The collective diffusion coefficient is[29]:

$$D_c = \frac{k_B T}{6\pi\eta\xi_h} \tag{2.3}$$

where $\eta$ is the viscosity and $\xi_h$ is the hydrodynamic screening length, which can be viewed as the effective pore size of the network. The collective diffusion coefficient, $D_c$, and Darcy's permeability coefficient, $\mathrm{D_p} = \mathbf{P}\eta\mathrm{V_m}$, are related as[29]:

$$D_p = \frac{k_B T}{6\pi\xi_h}\frac{1}{E} \tag{2.4}$$

with

$$E = \frac{2G\,(1-\nu_\infty)}{(1-2\nu_\infty)} \tag{2.5}$$

For $\nu_\infty = 0.25$, $E$ is equivalent to 3 times the shear modulus, $G$. The shear modulus can be represented in terms of the hydrodynamic screening length[30]:

$$G = k_B T/\xi^3 \tag{2.6}$$

Combining all this together, with $\xi_h = \xi$, we get:

$$D_p = \frac{\xi^2}{18\pi} \tag{2.7}$$

or

$$\mathbf{P} = \frac{\xi^2}{18\pi\eta V_m} \tag{2.8}$$

If we define a prefactor, $a_0$, with a magnitude in the angstrom range, we can set $\xi = a_0\phi_p^{-3/4}$. With $a_0 \approx 0.5$ nm:

$$\mathbf{P} = a_0^2\frac{\phi_p^{-1.5}}{18\pi\eta V_m} \tag{2.9}$$

or

$$D_p = a_0^2\frac{\phi_p^{-1.5}}{18\pi} \tag{2.10}$$

Taking this form, the permeability of the material can be described easily using the volume fraction of the polymer, $\phi_p$. Depending on the method of characterization and the industrial traditions, water transport can be assessed in a multitude of ways. Some common units found in literature include $\mathrm{cm}^2/\mathrm{s}$ ($\mathbf{P} * \mathrm{RT}$)[31], $\mathrm{m}^2$ (Darcy's permeability coefficient, $\mathrm{D_p} = \mathbf{P}\eta\mathrm{V_m}$)[32], and $\mathrm{m}^2/\mathrm{s}\cdot\mathrm{Pa}$ (specific water permeability, $\mathbf{P} * \mathrm{V_m}$)[33]. Despite a lack of consistency from field to field, these results are all ways to represent membrane performance. A further discussion of membrane permeability can be found in Chapter 3.

Most of the current commercially available PEMs require the membrane to be hydrated in order to achieve satisfactory proton conductivity. Excessive swelling or drying can often lead to detrimental deterioration of the mechanical properties, especially at elevated temperature[34,35]. Water act as the mobile phase that facilitates proton conduction in current PEM technology, and is a necessity for membrane operation. However, too much water can lead to plasticization of the material and depression of the $T_g$.Therefore, assessment of the

membrane water uptake is a crucial in describing the performance of PEMs. Water uptake is represented as the mass ratio of the absorbed water to the dry membrane, following:

$$Water\ uptake\,(\%) = \frac{m_{wet} - m_{dry}}{m_{dry}} \times 100 \tag{2.11}$$

where $m_{wet}$ and $m_{dry}$ are the mass of fully hydrated and dry membranes.

Both conductivity and water uptake dependent strongly on the concentration of ion-conducting moieties in the polymer. The total amount of active sites or functional groups in the ion-exchange membrane is represented as the ion exchange capacity (IEC) with units of milliequivalents per gram of polymer (mequiv/g or mmol/g). This parameter is measured by acid-base titration. Higher IEC tends to result in higher conductivity, since there are more active sites at which ions can be transported, at the cost of increased swelling, as these same sites can bind water molecules. Therefore, a balance between conductivity and water uptake must be kept in order to maintain the structural integrity of the membrane.

### 2.1.2 Membranes for Water Purification

There are many ways to produce clean, potable water, but traditional methods such as thermal distillation and vacuum distillation are often expensive and inefficient. Pressure driven processes such as reverse osmosis (RO) shown in Figure 2.1 and nano-filtration (NF) rely on an applied pressure to separate salts from water through a semipermeable membrane[9,36,37]. Unlike micro-filtration and ultra-filtration membranes, which rely on pore sizes to selectively filter out unwanted solutes via pore flow, reverse osmosis membranes rely on solution-diffusion, such as ionic-transport and charge separation, to produce clean water. Current industry standard for RO semipermeable membranes revolve around thin-film composites, which exhibit exceptional water transport and salt rejection properties[22]. These membranes are fabricated through a process called interfacial polymerization (IP), in which

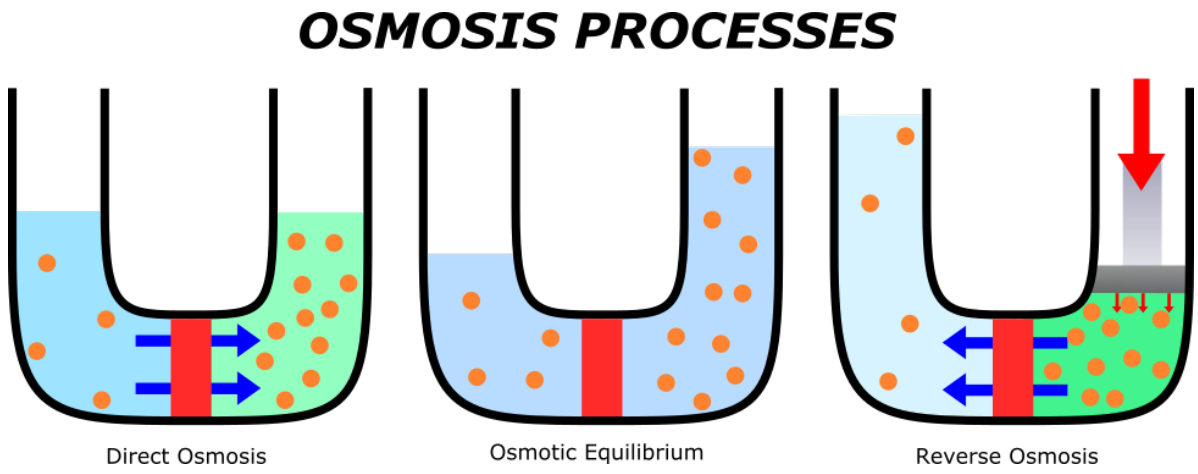


Figure 2.1: Schematic showing the differences between direct osmosis and reverse osmosis processes. In direct osmosis, the difference in chemical potential between the two sides of the membrane drives the solvent across to the more concentrated side until the system reaches osmotic equilibrium. In reverse osmosis, an external pressure is applied to drive separation across a semipermeable membrane, forcing the solvent to move from the concentrated side to the dilute side in a reverse fashion.

two immiscible solutions of aqueous polyamide and organic chloride acid are mixed together to form a thin film, generally on top of a porous polysulfone supporting layer.

Figure Figure 2.2 depict the interfacial polymerization between trimesoyl chloride (TMC) and m-phenolyenediamine (mPD) to form a polyamide thin used in RO. The simplicity of IP makes it easy to scale up fabrication of membranes, making reverse osmosis economically viable to treat water on a large scale. However, polyamide-based RO membranes are limited in their mechanical strengths due to poor thickness and roughness control[37].

Steps have been taken to address surface roughness through the use of a layer-by-layer spin-coating deposition process or other surface treatment techniques that have been shown to produce ultra-smooth surfaces[38,39]. However, the layer-by-layer process is time consuming, and can only produce in small quantities. Surface treatment also leads to additional costs. As a result, such a fabrication method requires huge overheads and additional operating costs to scale-up, and thus have not yet been adapted commercially.

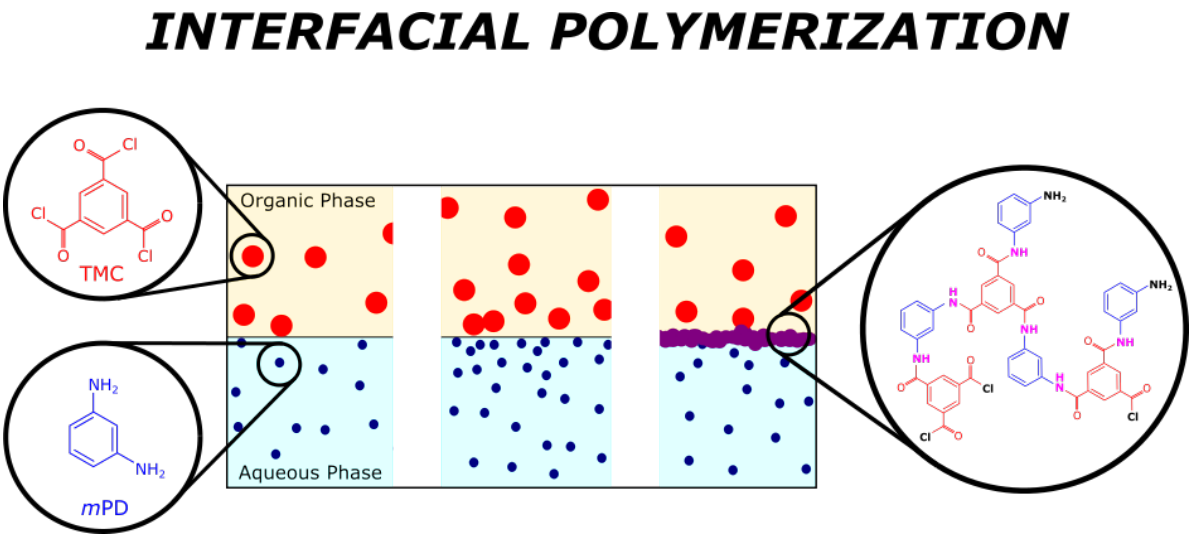


Figure 2.2: Illustration of interfacial polymerization between trimesoyl chloride (TMC) and m-phenolyenediamine (mPD).

Fouling is another major challenge for membranes used in wastewater treatment and solvent recovery applications[12,21]. Recent work has focused on developing new processing and post-processing techniques to ameliorate particulates and microbes build up at the membrane surfaces that reduce transport and shorten membrane longevity[16,20,21,40].

Despite being second in consideration after ion and solvent transport, factors such as mechanical strength, surface roughness, and chemical resistance are still all important. These material properties are intricately related to the complicated nano and microscale structures of the polymer composite that give rise to unique ionomeric properties. Thus, in order to address the current global water shortage crisis, we must develop proper processing methods to engineer new material systems with anti-fouling enhancements, improved chemical resistance, and desirable mechanical properties, without sacrificing ion and water transport properties.

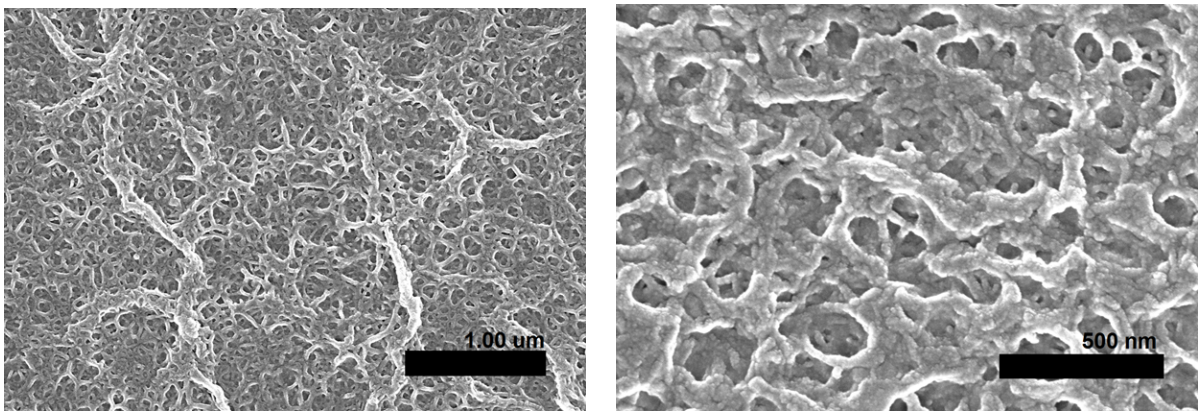


Figure 2.3: SEM micrographs of polyamide thin films produced via interfacial polymerization.

### 2.1.3 Sulfonated Block Copolymers

Among the wide variety of new materials capable of conducting charge, ion-containing block copolymers have garnered increasing attention. More specifically, the polar ionic species enable ion selectivity and conductivity, while the nonpolar species provide mechanical stability and chemical resistivity. The charged and uncharged domains further drives microphase separation, resulting in a multitude of self-assembled hierarchical structures. By controlling the chemistry, molecular weight, and volume fraction, the material can be tuned to to exhibit desirable ionomeric properties or structural morphology.

One promising material class with the potential to replace fluorinated membranes currently used as the industrial benchmark are sulfonated block copolymers. Typical sulfonated block copolymers contain a sulfonated end-block and a neutral block providing mechanical stability. As discussed previously, this basic design suffers from mechanical deterioration at increasing levels of sulfonation. However, without sufficient ion-conducting moieties, the membrane cannot conduct charge.

There are many advantages to using sulfonated block copolymers over other sulfonated high-performance polymers. Although sulfonation of commercially available polymers such

as polyether or polysulfone[1,6,41] is a suitable method to obtain IEMs, the products often suffer from inconsistent degrees of sulfonation and depend on sensitive reaction conditions. Moreover, a higher degree of sulfonation leads to high swelling of the materials, which can be undesirable as it leads to a loss of mechanical strength. The use of block copolymers can ameliorate the swelling of the ion-conducting segments, as the non-ionic segments act to pin the ion channels and reduce swelling effects[42,43]. In most cases, polystyrene blocks are strategically selected to be sulfonated to transport ions, while the non-sulfonated segments provide mechanical stability to the material. Since swelling of the ion-conducting segments is less of a concern in multi-block copolymer systems, high degree of sulfonation relative to those of complex polymers can be achieved. The structural tunability of the system also gives insight into the molecular underpinnings of order-disorder transitions approximated by Flory-Huggins Theory and self-consistent field theory.

In Chapters 3 and 4, a sulfonated pentablock copolymer is investigated. In contrast to most typical sulfonated block copolymer materials, the pentablock is uniquely designed, with only the mid-block sulfonated instead of the end-blocks. The polymer backbone is first synthesized from a living anionic polymerization technique. The isoprene mid-blocks are then hydrogenated, followed by selective sulfonation of the central styrene block to form a (t-butylstyrene – hydrogenated isoprene – sulfonated styrene – hydrogenated– t-butylstyrene) pentablock structure[44]. The end-block tert-butylstyrene (tBS) provides good mechanical strength, while the hydrogenated isoprene (HI) introduces flexibility to the structure. The sulfonated styrene (SS) block form an interconnected ion exchange network that allows for the passage of water. Together, the isoprenic and styrenic end-blocks provide good mechanical strength and flexibility in both wet and dry environments. The use of multi-block copolymers can ameliorate swelling issues of the ion-conducting segments without sacrificing transport and mechanical properties, as additional segments can act to pin the ion channels and further improve membrane stability.

Choi et al.[42] investigated the effect of ionic content on the water uptake, water transport, and structural morphology of these pentablocks. The water transport rates for Nexar pentablock copolymers in Figure 2.4 reveal that the material does not transport water at IEC below 1.5. Additionally, although the water transport property is further improved at increasing IECs, the membrane swells further and reduces mechanical strength.

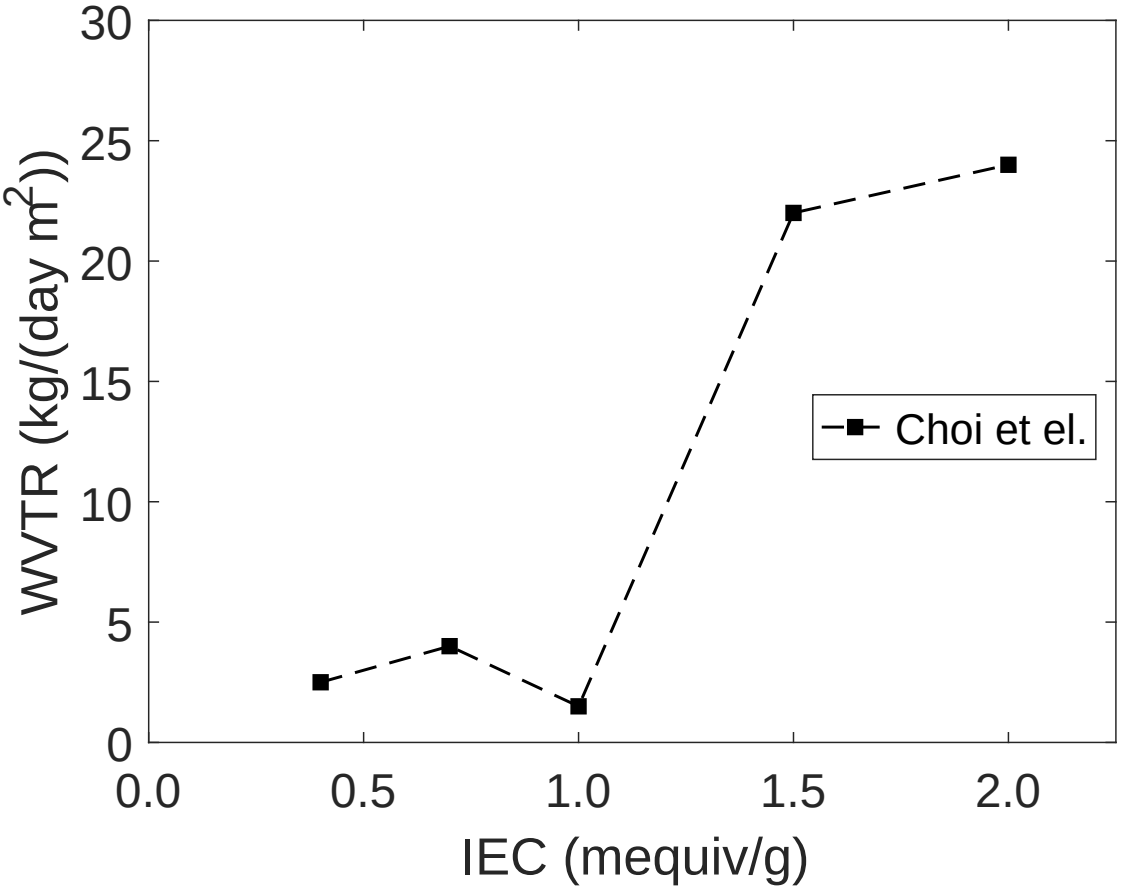


Figure 2.4: Water transport rates for Nexar pentablock copolymers at various levels of sulfonation, represented in ion exchange capacity (IEC). Adapted from Choi et al.[42]

In ion exchange membranes, the water uptake influences important membrane parameters such as ionic resistance and permselectivity, as discussed above. Water uptake also influences the membrane mechanical properties; high values of water uptake are desired for

high conductivity but a compromise has to be made in order to maintain its mechanical properties. Water uptake in an anion exchange membrane depends on the nature of the material, fixed charge concentration and degree of crosslinking.

Numerous studies[45,46] have experimented with the wide selection of tunable parameters of block copolymers, but the mechanisms leading to the formation of ionic domains which depend on sulfonation level[47], solvent polarity[48], and non-ionic block chemistry[9,49], are still not fully understood. Moreover, investigation into the mechanical properties of these material under hydrated conditions are still lacking.

Despite significant advancements, predicting the nanoscale structure in charged polymers remains a challenge due to the intricate ionic correlations with influence at many length scales. With the establishment of powerful x-ray scattering techniques and non-traditional mechanical tests, the structure and the mechanical properties of ion-exchange membranes, particularly ion-containing block polymer membranes, can be fully characterized[50–53]. The performance and stability of relevant ionomeric polymer thin films may be improved by developing a more accurate understanding of the dependence of sulfonation level, degrees of polymerization, block chemistry, post-processing methods, and casting solvents on the dynamics, structural evolution, and formation of ion-exchange membranes.

## 2.2 Large Strain Theory

Advancements in membrane science and technology have led to numerous creative solutions in addressing increasing global demands for clean water, renewable energy, and medicine. As a result, polymeric membranes now form a large part of the commercially important commodity plastics available today. These materials are often lightweight, optically transparent, and mechanically superior to their bulk counterparts. However, despite the growth of new thin-films materials available in the engineering toolbox, the characterization of thin-film me-

chanical properties, especially a reliable method to predict the large-strain time-dependent behavior, is still lacking. In order to accurately analyze the properties of these materials processes by which many polymeric thin films are manufactured, as well as to ascertain the response of the resulting part to service life loading conditions, a constitutive law that properly accounts for the large, inelastic deformation behavior of these materials is required. Such behavior is known to exhibit strain rate, temperature, and pressure dependent yield, as well as true strain softening and hardening after yield. As less sample volume is required for testing, the prohibitive cost associated with polymer design and optimization can be lessened, leading to an explosion of new materials in the age of nanotechnology[54–57].

### 2.2.1 Biaxial Membrane Inflation

As thin films become increasingly more prevalent, the way we characterize these materials must evolve. Traditional impact measurement techniques such as the pendulum[58] and ballistics tests[59,60] are unsuitable for studying thin films as they have predefined limits to sample geometries and require large sample volume. Other techniques such as indentation[61] and tensile tests[62] may be more applicable to thin films, but they provide an incomplete description of the rate-dependent responses and deformation mechanisms that facilitate material recovery. For this work, a equibiaxial membrane inflation technique developed by Dr. Evan Laprade is used for characterizing the large strain deformation behavior of polymer thin films.

Issues such as pinholes, membrane buckling and delamination are challenges that need to be addressed to improve the mechanical durability of IEMs[3,22]. From an ion-transport perspective, crack propagation through the thickness direction is more relevant, as surface roughness and defects may cause sharp cracks to form readily at the active layer. However, it is difficult to introduce sharp pre-cracks in the thickness direction of thin-films in tradi-

tional *ex-situ* membrane tests. Moreover, membranes used in fuel cell and water treatment applications are constrained from in-plane straining geometry[14]. Therefore, in order to study the constitutive properties of free standing membranes, the strength of membranes under applied load, and the numerical analysis of membranes in diffusion media, non-traditional mechanical tests need to be employed.

For structural polymeric materials, crazes or micro-fatigue cracks often precede the formation of cracks of catastrophic size, and membrane functionality might suffer drastically from leakage before catastrophic ruptures fully develop. Therefore, the failure criterion for characterizing PEMs should not be complete rupture of the specimen, as is typically characterized in uniaxial tensile tests. Instead, membrane failure should be defined as leakage from membrane creep or fatigue. Since it is evident that crazes or cracks may be sufficient to allow leakage or drastic decrease in performance[47,63], it is reasonable to apply a pressure-loaded membrane inflation test.

In this membrane inflation geometry, the equibiaxial stress state induced within the central region of the pressurized membrane simulates the biaxial stress state within a fuel cell or a water desalinization membrane tube[64–66], in which the membrane is constrained from in-plain straining and the stresses of primary interest are inherently biaxial. The deformation behavior of a polymer membrane is geometrically complex, and the large strains and non-linear time-dependent mechanical behavior of the material can result in a dramatic difference between macroscopic and microscopic responses. Long and coworkers[67] have provide a full analytical treatment of the large strain deformation of hyperelastic membranes under an equibiaxial stress. This treatment marks the foundation of the work presented in Chapters 3 and 5.

Typically, large deformation mechanics is characterized using local strain measurements on a flat circular membrane held in a clamp at its circumference and inflated using pressurized

air to form a to a spherical bubble. The inflation geometry confines the material to a state of plane stress, and a state of equibiaxial tension is achieved at the top of the bubble.

This technique has been widely used to characterize membranes of rubbers and polymers melts[64,68–73], and more recently ultra-thin films[74–77]. The equations governing the large deformation of free standing membrane under pressure, P, are these four ordinary differential equations (ODEs)[67]:

$$\frac{d\lambda_\xi}{d\rho} = \frac{\lambda_\xi \left(T_\phi - T_\xi\right) cos\alpha - \lambda_\xi \left(\partial T_\xi / \partial \lambda_\phi\right) \left(\lambda_\xi cos\alpha - \lambda_\phi\right)}{\lambda_\xi \left(\partial T_\xi / \partial \lambda_\xi\right)} \tag{2.12}$$

$$\frac{d\alpha}{d\rho} = \frac{P\rho\lambda_\xi\lambda_\phi - \lambda_\xi T_\phi sin\alpha}{\rho\lambda_\phi T_\xi} \tag{2.13}$$

$$\frac{d\lambda_\phi}{d\rho} = \frac{\lambda_\xi cos\alpha - \lambda_\phi}{\rho} \tag{2.14}$$

$$\frac{dz}{d\rho} = \lambda_\xi sin\alpha \tag{2.15}$$

These four ODEs describe the equilibrium configuration and geometric relations of the membrane under large strain. $T_\xi$ and $T_\phi$ are the longitudinal and latitudinal line tensions of a deformed membrane, with units of force/length. Parameter $\rho$ is the floating variable that defines a point on an undeformed membrane, with limits of $0 \leq \rho \leq R_m$, where 0 is the center and $R_m$ the radius of the membrane. There are several boundary conditions that must be satisfied to solves these ODEs in our biaxial membrane inflation experiment. Firstly, the undeformed membrane is clamped on the edges. Next, the stretch in two principle directions, $\xi$ and $\phi$, should be the same as the bubble is symmetry around the pole. Lastly, under an applied pressure, the maximum displacement of the membrane occurs at the apex. With these in mind, the boundary conditions can be defined as:

$$\lambda_\phi(\rho = R_m) = 1 \tag{2.16}$$

$$z(\rho = R_m) = 0 \tag{2.17}$$

$$\lambda_\xi(\rho = 0) = \lambda_\phi(\rho = 0) = \lambda_0 \tag{2.18}$$

$$\alpha(\rho = 0) = 0 \tag{2.19}$$

$$z(\rho = 0) = -\delta \tag{2.20}$$

To ensure a solution can be found, the stretch ratio, $\lambda_0$, and the product of the small strain Young's modulus and thickness, $Eh$, are allowed to float. The model assumes the membrane is a purely elastic material and $Eh$ must be a constant. By allowing $Eh$ to float, the viscoelastic character such that a time-dependent modulus is incorporated into the analysis. The shape of the inflated membrane follows the strain energy density function, W, for an incompressible neo-Hookean material[67]:

$$W = \frac{E}{6}\left(\lambda_\xi^2 + \lambda_\phi^2 + \left(\frac{1}{\lambda_\xi \lambda_\phi}\right)^2 - 3\right) \tag{2.21}$$

where $\lambda_\xi$ and $\lambda_\phi$ are the principle stretches. For a pressurized spherical vessel, the stress at the bubble apex, $\sigma_{apex}$, is directly related to the pressure difference and the radius of curvature[78]:

$$\sigma_{apex} = \frac{PR}{2t_m} \tag{2.22}$$

where P is the pressure inside the bubble, R is the radius of curvature, and $t_m$ is the membrane thickness. The membrane thickness can be further calculated if we assume incompressibility[65,79]:

$$t_m(\varepsilon) = t_0 e^{-2\varepsilon_{apex}} \tag{2.23}$$

Since the material is assumed to be incompressible, the stretch ratio in the thickness direction is equivalent to $1/\lambda_\xi\lambda_\phi$. The average area strain, $\varepsilon_{A,avg}$, is given by:

$$\varepsilon_{A,avg} \equiv \frac{A_m}{\pi R^2} - 1 = \left(\frac{\delta}{R}\right)^2 \tag{2.24}$$

where $A_m$ is the area of the deformed membrane. Laprade and coworkers[76] applied this treatment to triblock copolymers and found that the maximum error of 8% occurs at $\delta/R \sim 1$ for calculating the apex strain using the above method. Therefore, a correction to the calculated $\varepsilon_{A,avg}$ can be made to get an accurate prediction of the apex strain:

$$\varepsilon_{apex} = q\varepsilon_{A,avg} \tag{2.25}$$

where $q$ is a fitting parameter obtained from additional calibration experiments. Previous work has determined $q$ experimentally by tracking the membrane thickness using magnetic probes[72] or by tracking the membrane deformation using fluorescent QD grids[47], revealing a value of $q = 1.2$. This is the value used in the present work.

These measurements can be quite time-consuming, as they are complicated and prone to error. In particular, the analysis derived by Bloksma[78] made simplifying assumptions that results in overestimation of the stresses at the apex. By relaxing constraints on elasticity to allows viscoelasticity, the analysis can be amended. Most inflation tests assume spherical shape of the bubble. However, this is only valid at moderate strains, and at larger strains

the bubble takes on an elliptical shape. has been shown to be accurate at moderate strains only. At larger strains, the bubble assumed an elliptical shape with a axis ratio that deviates from unity[67]. By applying a correction factor of $q = 1.2$, this simplification assumption can be resolved.

# Chapter 3

## Water Transport and Mechanical Response of Block Copolymer Ion-Exchange Membranes for Water Purification

Few ion exchange membranes with high ionic conductivity can maintain good mechanical integrity under high humidity conditions. Often times trade-offs between transport and mechanical properties have to be made, but only to yield minimal improvements in membrane performance. Therefore, identifying polymer architectures that achieve minimum performance metrics in a wide range of properties is critical to the advancement of ion exchange membrane science.

In this chapter, the mechanical response and water transport properties of a series of ***ABCBA*** pentablock copolymer membranes designed to transport water was investigated. A membrane inflation experiment was used to measure the mechanical response of a thin film under load in an aqueous environment. We found that the creep resistance of the block copolymers originates from glassy ***A*** blocks of either poly(p-methyl styrene) or poly(t-butyl styrene), and water permeability is attributed to the polystyrene ***C*** block that is partially sulfonated. An enhancement to the membrane creep resistance in the wet state was made by replacing the poly(t-butyl styrene) ***A*** blocks with poly(p-methylstyrene). Additional improvements to creep resistivity is achieved by decreasing the molecular weight of the polyelectrolyte ***C*** block. Both of these modifications increased the creep resistance of the membranes in a wet state while retaining a high degree of water permeability.

Material in this chapter is reproduced from the article "Water Transport and Mechanical Response of Block Copolymer Ion-Exchange Membranes for Water Purification" authored by Shawn Chen, Carl Willis, and Kenneth R. Shull, *Journal of Membrane Science,* 544, 388-396, 2017[77].

## 3.1 Introduction

Among the variety of materials exhibiting ionomeric properties, ion containing block copolymers have garnered increasing attention[22]. Block copolymers are important for the large volume of applications in thermoplastic elastomers and pressure sensitive adhesives, and they provide the unique opportunity to control the macroscopic mechanical properties by tuning the self-assembled morphologies and packing structures at the nanoscopic scale[80]. Sulfonated block copolymers are a subclass of these materials developed for use in ion-conducting membrane applications[45,46], including ion-exchange membranes for fuel cells[7,8] and water filtration membranes[18,36]. In addition to exhibiting ionomeric properties desirable for water and ion transport, sulfonated block copolymers have many advantages over other sulfonated high-performance polymers. Many of these advantages arise from the ability to control the morphology of the materials by controlling the detailed composition and volume fractions of the different copolymer blocks[7].

Sulfonated pentablock copolymers commercially known as Nexar® Polymers are an example of an interesting class of materials designed to achieve a balance between high mechanical strength and high water permeability. Figure 3.1 shows the chemistry of the basic sulfonated pentablock system. In this design, only the middle styrenic block is sulfonated, whereas the outer blocks are present to provide mechanical strength. The polymer backbone is first synthesized from a living anionic polymerization technique. The isoprene mid-blocks are then hydrogenated, followed by selective sulfonation of the central styrene block to form a (tBS – HI – SS – HI – tBS) pentablock structure[44]. The end-block tert-butylstyrene (tBS) provides good mechanical strength, while the hydrogenated isoprene (HI) introduces flexibility to the structure[42]. The sulfonated styrene (SS) block forms the ionic domains responsible for the ion and water transport properties of the material. Other systems of sulfonated styrene block copolymers typically adopt a di-block design[41,63,80], in which a sul-

fonated block responsible for water and ion transport is attached to a second block that provides mechanical strength. The use of multi-block copolymers can ameliorate swelling issues of the ion-conducting segments without sacrificing transport and mechanical properties, as additional segments can act to pin the ion channels and further improve membrane stability.

(a)

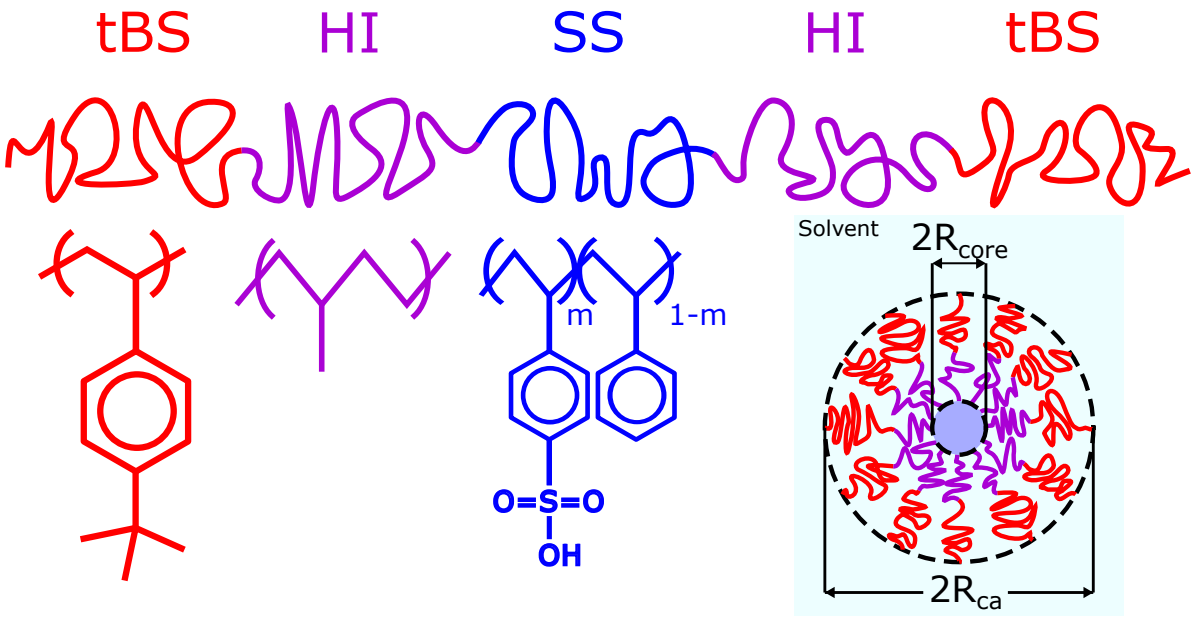


Figure 3.1: Schematic of the sulfonated pentablock copolymer. The inset is an idealized micelle in CH/toluene solvent, with a SS core and a swollen tBS/HI corona, adapted from Choi *et al.*[42]

In this work, the mechanical and water transport properties of a system of ionomeric block copolymers is investigated. The mechanical properties are investigated with a biaxial membrane inflation technique. The technique is extremely useful for materials optimization as very small amounts of sample are needed. The experimental setup enables testing while the membrane is in its hydrated state, a condition of obvious relevance for applications in water purification.

When immersed in water, sulfonated styrene (SS) blocks swell, merging with one another and forming a continuous pathway through which water is able to diffuse (Figure 3.2). While a variety of equivalent expressions can be used to define the permeability, $k_m$, we use the following form motivated by Darcy's law describing pressure driven flow in a porous medium, where the water transport rate is proportional to the pressure gradient and inversely proportional to the fluid viscosity, $\eta$ :

$$k_m = \frac{Qh\eta}{A\Delta P} \tag{3.1}$$

Here $Q$ is the volumetric flow rate ($m^3/s$), $A$ is the membrane area, $\Delta$P is the applied pressure difference across the membrane, and $h$ is the membrane thickness. The overall water permeability is determined by the intrinsic permeability of the water-swollen sulfonated styrene blocks, and a geometric, tortuosity factor, $\tau$, that relates the overall membrane permeability to the intrinsic permeability of the water-conducting micro-domain.

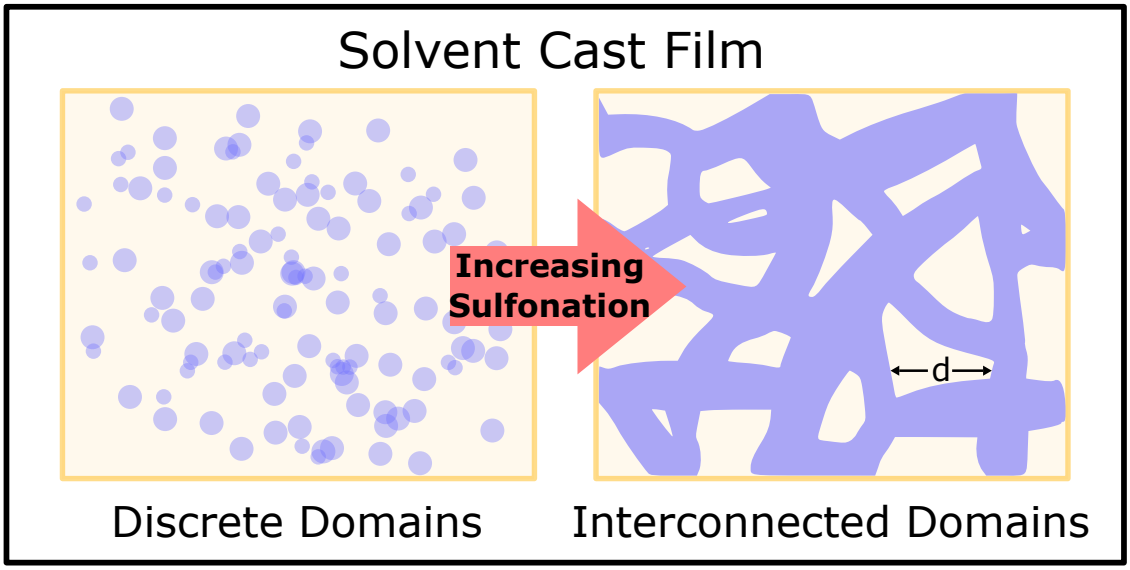


Figure 3.2: Schematic of the inner ionic domain of the pentablock. As the sulfonation level increases, the ionic domains evolve from discrete pockets into interconnected channels.

We can employ an analogy here to fluid flow in materials where a high-permeability gel with a hydraulic permeability of $k_{gel}$ is confined within an impermeable matrix, with an overall gel volume fraction of $\phi_{gel}$. In this case we can use the following expression to relate $k_m$ to $k_{gel}$[81]:

$$k_m = \frac{k_{gel}\phi_{gel}}{\tau} \tag{3.2}$$

The tortuosity is equal to 1 for ideal, cylindrical channels that penetrate directly through the membrane, and is expected to be close to 2 for the more random pore structures that are expected in our case[42,82,83]. We expect the swollen gel to have a permeability similar to other polymer solutions of similar concentrations, for which the permeability can be written in the following form[84,85]:

$$k_{gel} = a_0^2 \phi_p^{-1.5} \tag{3.3}$$

Here $a_0$ is a prefactor with a magnitude in the angstrom range and $\phi_p$ is the volume fraction of polymer in the gel. Combination of Equations 3.2 and 3.3 gives the following overall expression for $k_m$:

$$k_m = \frac{a_0^2 \phi_p^{-1.5} \phi_{gel}}{\tau} \tag{3.4}$$

While there is some system-wide variation in $a_0$ and $\tau$, these parameters are generally known with a reasonable degree of precision, providing a clear design strategy for producing membranes with a maximal permeability.

In a practical application, the mechanical properties of the membranes are also important, and these are much more difficult to predict quantitatively. For example, increasing $\phi_{gel}$ will

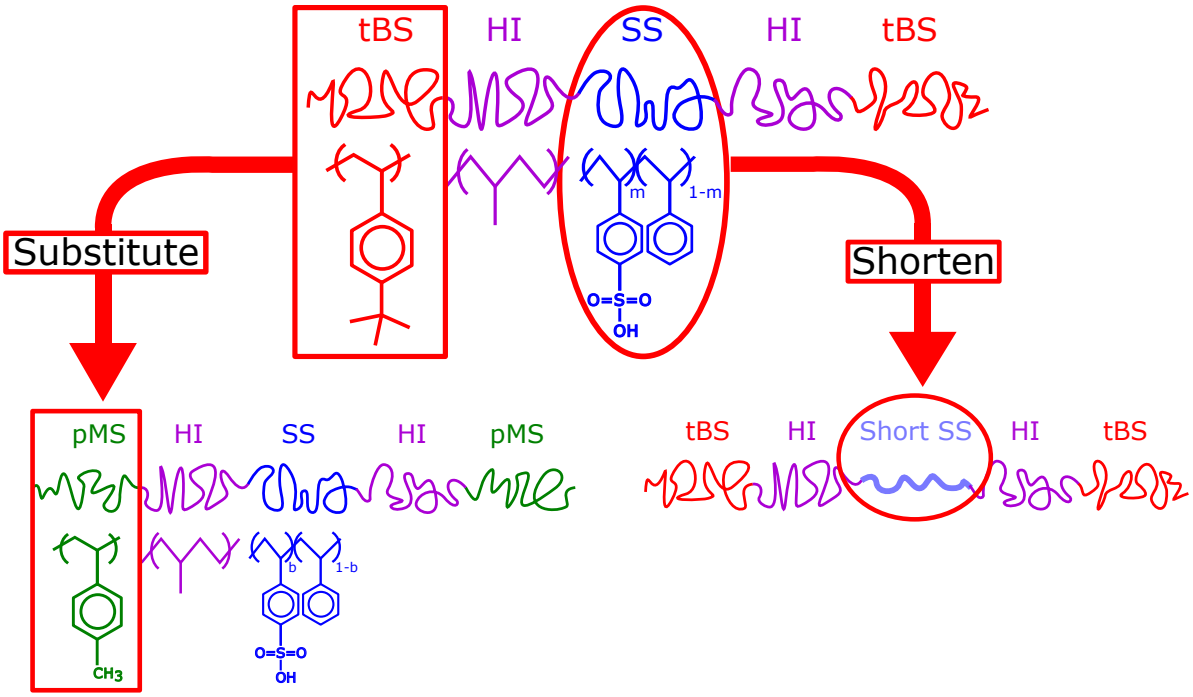


Figure 3.3: Modifications to the sulfonated pentablock copolymer, involving either the substitution of the poly(t-butyl styrene) end-block poly(p-methyl styrene) or the reduction in the length of the sulfonated polystyrene mid-block.

increase the membrane permeability, but at the expense of a decreased toughness and elastic stiffness of the membrane.

The purpose of the work described here is to pursue two different material design strategies in order to optimize the balance of permeability and elastic stiffness of the membranes. These two strategies correspond to modifications made to the original sulfonated styrenic pentablock system are shown in Figure 3.3. In the first of these the poly(t-butyl styrene) end-blocks are substituted with a poly(para-methyl styrene) end-block of similar molecular weight. In the second strategy the molecular weight of the gel-forming sulfonated polystyrene mid-block is reduced from 28kDa to 6kDa.

## 3.2 Experimental Details

### 3.2.1 Materials

The compositions of the three copolymers are summarized in Table 3.1, which lists the ion-exchange capacity (IEC), the sulfonation level of the mid-block, and the volume fraction of each polymer species in the pentablock construction in the dry state. Here, the reference Nexar pentablock copolymer is named "P-ref", the end-block substituted copolymer "P-sub", and the copolymer with reduced mid-block molecular weight "P-short". The molecular weight of the reference pentablock copolymer prior to sulfonation is approximately 15-10-28-10-15 kg/mol[86]. The equivalent molecular weight for P-sub is 15-17-38-19-15 kg/mol, and 16-10-6-9-13 kg/mol for P-short. The densities of the components used to calculate the volume fraction are as follows: *t*-butylstyrene (BS), 0.94g/cm$^3$[87]; p-methylstyrene (MS), 1.004g/cm$^3$[88]; hydrogenated isoprene (HI), 0.812g/cm$^3$ ? ; styrene (S), 1.048g/cm$^3$[88], and sulfonated styrene (SS), 1.43g/cm$^3$[89].

| Sample | End-block | IEC [mequiv/g] | Sulf. Level [mol %] | $\phi_{\text{end}}$ | $\phi_{\text{HI}}$ | $\phi_{\text{SS}}$ |
|---|---|---|---|---|---|---|
| P-ref | tBS | 2.0 | 58.0 | 0.39 | 0.46 | 0.15 |
| P-sub | MS | 2.0 | 57.0 | 0.22 | 0.66 | 0.12 |
| P-short | tBS | 0.67 | 62.8 | 0.46 | 0.53 | 0.01 |

Table 3.1: Summary of the sample compositions in the dry state. The dry state volume fractions for the end-block, hydrogenated isoprene block and sulfonated styrene block are $\phi_{end}$, $\phi_{HI}$ and $\phi_{SS}$, respectively.

### 3.2.2 Membrane Preparation

The polymers were originally received as 10-12 wt% polymer solutions in a cyclohexane/heptane mixed solvent. Bare silicon wafers were cleaned in a UV/O-zone scrubber prior to use. A sacrificial layer of 1 wt% poly(acrylic acid) (PAA) in (50/50 v/v) MeOH/$H_2O$ solution was

first spin-coated onto the substrate in order to release the membrane from the substrate. Samples used for water uptake and water permeability measurements were hand-cast using a wire-wound drawdown bar (size 50, Paul N. Gardner Company, Inc., Pompano Beach, FL) onto a 2-inch by 2-inch glass slide coated with a PAA sacrificial layer. Thickness measurements were confirmed using a high-resolution contact profilometer (Dektak 150, Veeco Instruments Inc.). Dry thicknesses of the films used for the permeability measurements were approximately 10 $\mu$m and weigh approximately 0.4 g.

Toluene (Sigma-Aldrich) dried with molecular sieves (Sigma-Aldrich) was used to dilute the as-received polymer solutions to 4-6 wt% polymer in order to spin-coat uniform thin films. Membranes used in membrane inflation were cast via spin-coating of the polymer solutions to produce membranes that were 0.5 $\mu$m thick. These membranes were floated onto a water bath and subsequently transferred onto the end of an aluminum tube. (Figure 3.5A). This membrane was capped in place, and submerged into water for 20 minutes to ensure that the membrane was fully hydrated prior to testing.

Previous work[42] has shown that processing technique of these materials could lead to different membrane morphologies. Additionally, Griffin et. al.[48] reported that a blend of polar and non-polar solvents can be used to tune the solution morphologies, and higher-order structures can be achieved. The solvents used in this work are non-polar and have high vapor pressures, which enables rapid removal of solvents to achieve consistent casting of uniform films. AFM micrographs reveal that both casting methods result in membranes having a disordered micellar structure with domain spacings on the order of $\sim 31\,nm$. Future work is needed in order to elucidate the potential effect that different membrane morphology may have on the mechanical properties and transport performance of these materials.

### 3.2.3 Membrane Swelling

The samples were cast from solution, dried in air for 24 hours at room temperature and subsequently dried in a vacuum oven at 110 °C to remove any water molecules adsorbed, and weighed to give the dry mass, $m_{dry}$. Subsequently, the membranes were immersed in deionized water for 48 hours at room temperature. The wet mass ($m_{wet}$) of the membrane is measured after the surfaces of the membrane is softly wiped dry.

### 3.2.4 Water Permeability Measurement

Water permeability was measured at room temperature using a stainless-steel dead-end stirred cell (XFUF04701 Solvent-resistant Stirred Cell, EMD Millipore, Billerica, MA). The sample is supported in the cell using a hydrophilic disc filter (Millipore) to prevent breakage. The cell is filled with 150 mL of de-ionized water and pressured with nitrogen to 50 psi. The chamber was pressurized to shorten the duration of the experiment, and does not affect the measured permeability[90]. The membrane thickness was measured after the experiment using an optical profilometer (Bruker ContourGT Optical Profiler, Bruker Daltonics Inc., Billerica, MA).

### 3.2.5 Biaxial Membrane Inflation

Figure 3.4 shows the biaxial membrane inflation apparatus used in this study. The stage is comprised of an experimental chamber housing an aluminum inflation tube with an inner diameter of 12 mm. The inflation tube is connected to a pressure transducer (PX653, Omega Inc., Stamford, CT) and a syringe pump (NE-1000, New Era Pump Systems Inc., Wantagh, NY) to measure and modulate the pressure inside the membrane.

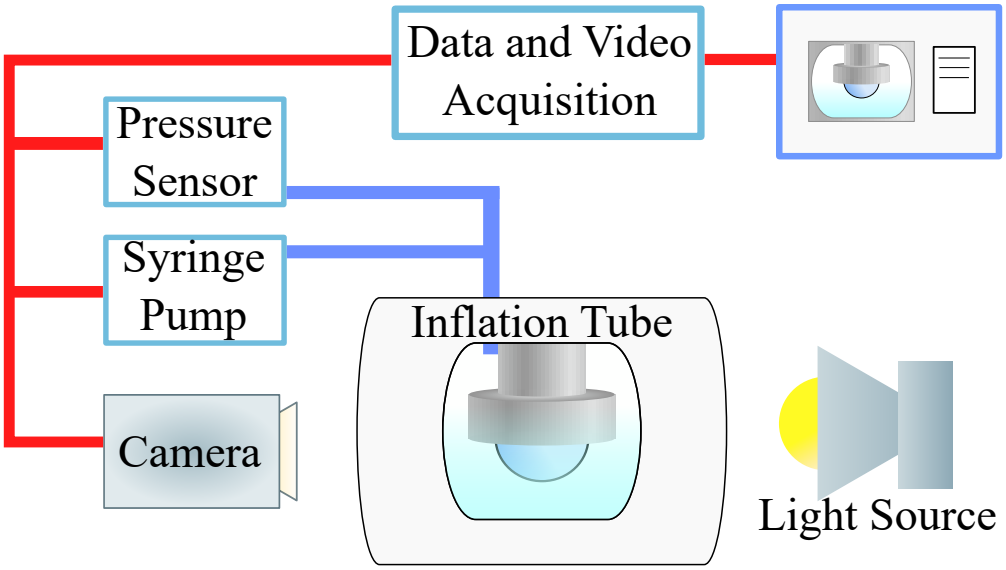


Figure 3.4: Schematic of the biaxial inflation apparatus.

A CCD camera (Adimec 1000m, Adimec Inc., Stoneham, MA) positioned on the side of the test chamber tracks the water level and the membrane profile. The pressure and video data were recorded simultaneously through a data acquisition system (National Instruments Inc., Austin, TX) that is interfaced with a MATLAB (Mathworks) program.

The membrane is transferred to the stage using a water bath, shown in Figure 3.5. Once the undeformed membrane is transferred onto the inflation tube, it is submerged in deionized water.

For a stress-controlled experiment, the membrane is pressurized with air at a rate of 0.1 mL/min until the target stress threshold is reached. The system then regulates the pressure within the membrane to maintain the apex stress at the target value. During a cyclic loading experiment (Figure 3.6b), the membrane is injected with air at a rate of 0.05 mL/min until the upper target of pressure (Pa) or displacement (mm) is reached, at which point the pump reverses direction. The protocol is looped without delay when loading the membrane for multiple cycles.

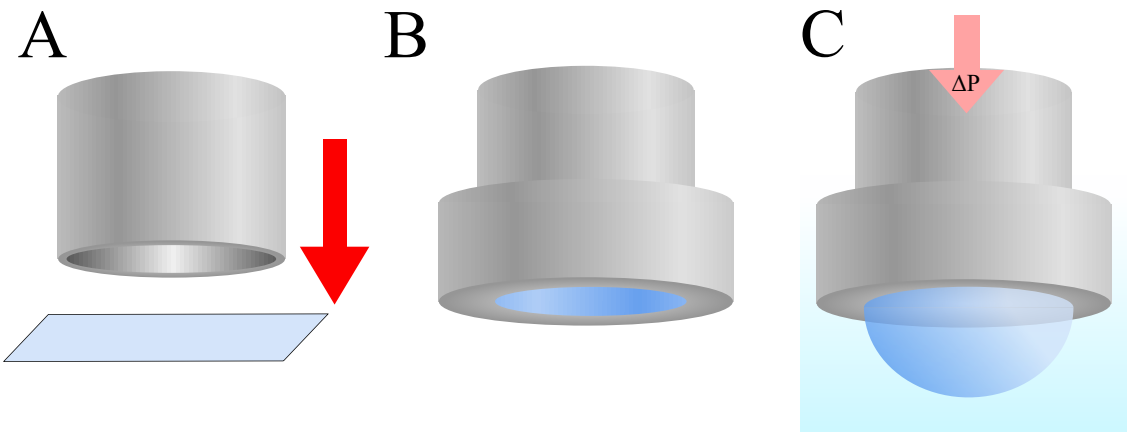


Figure 3.5: Schematic of membrane inflation procedure. (A) The aluminum tube is moved into contact with the free-floating film and (B) capped with an aluminum cap. (C) The membrane in submerged in water and pressurized with air.

### 3.2.6 Steady-State Creep

To capture the steady-state creep behavior of the membranes a constant stress is applied by monitoring $R_{apex}$, the radius of curvature at the membrane apex with a CCD camera and appropriately modulating the applied pressure. The tension, $T_{apex}$, at the membrane apex is then given by the Laplace pressure relationship:

$$T = \frac{P_{apex} R_{apex}}{2} \tag{3.5}$$

where $P_{apex}$ is the pressure difference across the membrane. Since the membrane is inflated with air in water, the hydrostatic pressure exerted by the column of water outside the membrane needs to be accounted for when determining $P_{apex}$ from the measured pressure difference, $P_{measured}$:

$$P_{apex} = P_{measured} - \Delta\rho g z \tag{3.6}$$

where $\Delta\rho$ is the density difference of the media on either side of the membrane, $g$ is the gravitational acceleration, and $z$ is the depth of water measured from the apex.

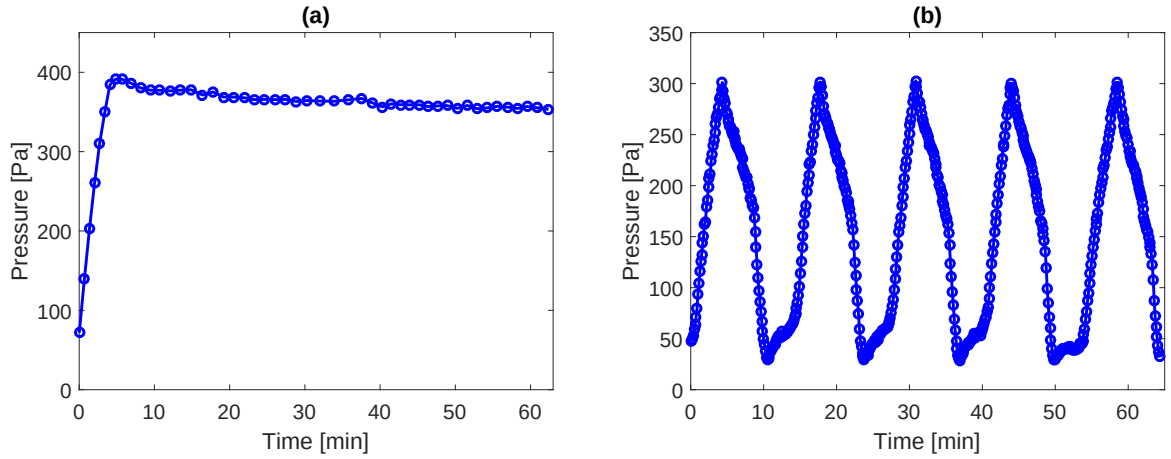


Figure 3.6: (a) Pressure versus time of a typical stress-controlled routine. The pressure decreases with time to maintain constant stress at the apex of the membrane. (b) Pressure versus time of a typical cyclic loading experiment. Each loop cycles between an upper and a lower threshold.

The stress at the membrane apex is obtained by dividing the membrane tension by the membrane thickness, $h_{apex}$:

$$\sigma_{apex} = \frac{T_{apex}}{h_{apex}} \tag{3.7}$$

Here $h_{apex}$ is obtained from the estimated from the initial thickness, $h_0$, and the apex area strain, $\epsilon_{apex}$;

$$h_{apex} = \frac{h_0}{\epsilon_{apex}} \tag{3.8}$$

The directly measured strain is the area strain, $\epsilon_{A,\,avg}$, given by:

$$\epsilon_{A,\,avg} = \frac{A_o}{\pi R_m^2} - 1 \tag{3.9}$$

where $A_o$ is the surface area of the deformed membrane and $R_m$ is the radius of the undeformed membrane. This average strain is assumed to be linearly related to $\epsilon_{apex}$:

$$\epsilon_{apex} = q\epsilon_{A,avg} \tag{3.10}$$

where $q$ is a fitting parameter obtained from additional calibration experiments. Previous work has determined $q$ experimentally by tracking the membrane thickness using magnetic probes[72] or by tracking the membrane deformation using fluorescent QD grids[47]. This previous work has shown that the apex strain can be approximated by assuming $q = 1.2$, and this is the value used on our work. Finally, the creep compliance, $D(t)$ is calculated by dividing the average area strain by the applied apex stress[2]:

$$D(t) = \frac{\epsilon_{apex}(t)}{\sigma_{apex}} \tag{3.11}$$

### 3.2.7 Extracting the Stress/Strain Behavior

Figure 3.7a shows the pressure vs. displacement curve for a P-ref membrane loaded under a displacement-controlled protocol, with upper and lower displacement targets of 3 mm and 1 mm, respectively. For each cyclic loading test, the membrane is inflated at a rate of 0.05 mL/min until a maximum apex displacement of 3 mm is reached. After the target is reached, air is withdrawn at the same rate until the initial displacement value is reached. Each cyclic test is cycled for 5 successive cycles.

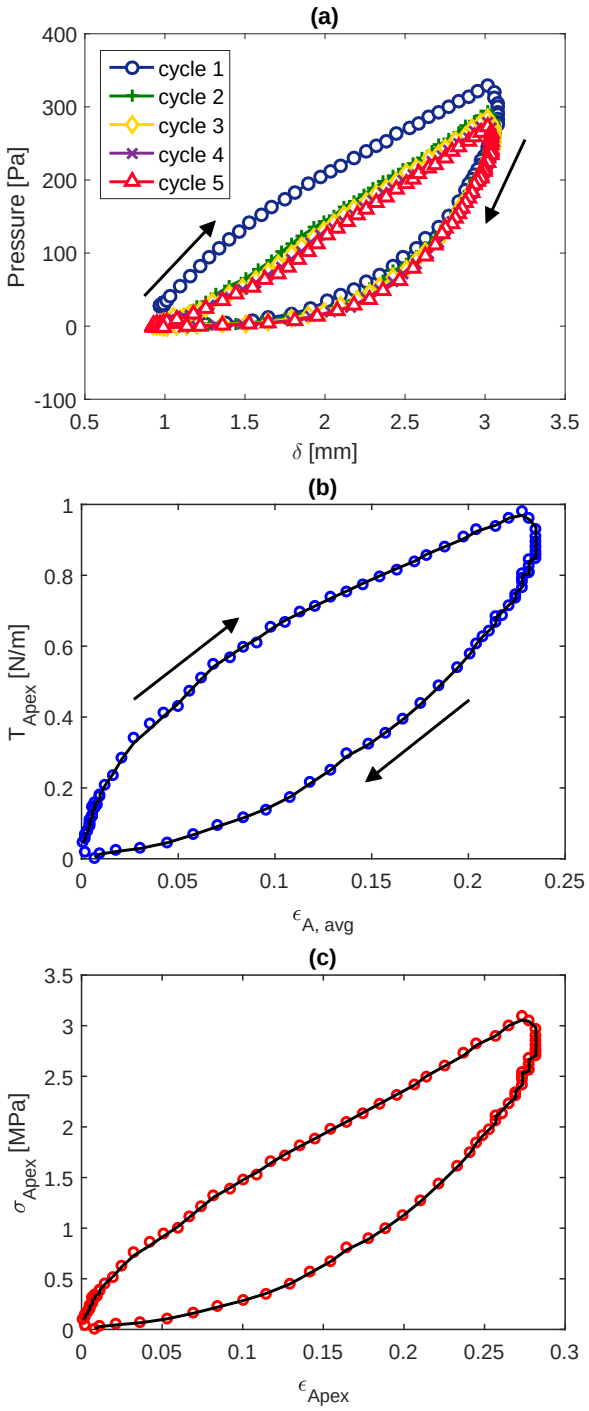


Figure 3.7: (a) Pressure versus displacement of a P-ref membrane loaded for 5 consecutive cycles. (b) Apex tension and versus average area strain (c) apex stress versus apex strain of the second cycle.

The results indicate that the deformation behaviors are reproducible after each cycle of inflation, and permanent deformation following the initial cycle results in non-recoverable strains in the membrane. Figures 3.7b and 3.7c show the tension and stress vs. strain of a hydrated P-ref membrane. The biaxial modulus, which is twice the Young's modulus for incompressible materials, can be calculated by taking the slope at low strain in the linear, elastic region. For this material we are effectively running a low-frequency dynamical mechanical experiment in the nonlinear regime. This is illustrated for the P-ref membrane in Figure 3.8, in which the time dependence of $\sigma_{\text{Apex}}$ and $\epsilon_{\text{Apex}}$ over one cycle is plotted. The stress and strain are not purely sinusoidal in this experiment, but an effective phase angle, $\Delta_{\text{eff}}$, can be obtained from the following expression[32]:

$$\sin \Delta_{eff} = \frac{\int \sigma_{Apex} d\epsilon_{Apex}}{4\pi \left(\sigma_{Apex}^{max} - \sigma_{Apex}^{min}\right)\left(\epsilon_{Apex}^{max} - \epsilon_{Apex}^{min}\right)} \tag{3.12}$$

Here $\sigma_{Apex}^{max}$ and $\sigma_{Apex}^{min}$ are the respective maximum and minimum values of $\sigma_{\text{Apex}}$ applied over one cycle, and $\epsilon_{\text{Apex}}^{\text{max}}$ and $\epsilon_{\text{Apex}}^{\text{min}}$ are the corresponding maximum and minimum values for $\epsilon_{\text{Apex}}$. For the P-ref membrane, a $\Delta_{\text{eff}}$ value of 5.4° is obtained. Figure 3.8 demonstrates the phase shift between the stress-strain response during a typical cyclic experiment. Mechanical properties obtained from these measurements are reproducible to within 10%.

## 3.3 Results and Discussion

### 3.3.1 Water Uptake and Water Permeability Measurement

We are able to extract values for both $\phi_{gel}$ and $\phi_p$ from the swelling data by assuming that the majority of the water adsorbed by a pentablock copolymer film is incorporated into the sulfonated polystyrene domain[31], and none into the glassy outer blocks. These values are listed in Table 3.2, along with measured values of the membrane permeability, $k_m$. Each of

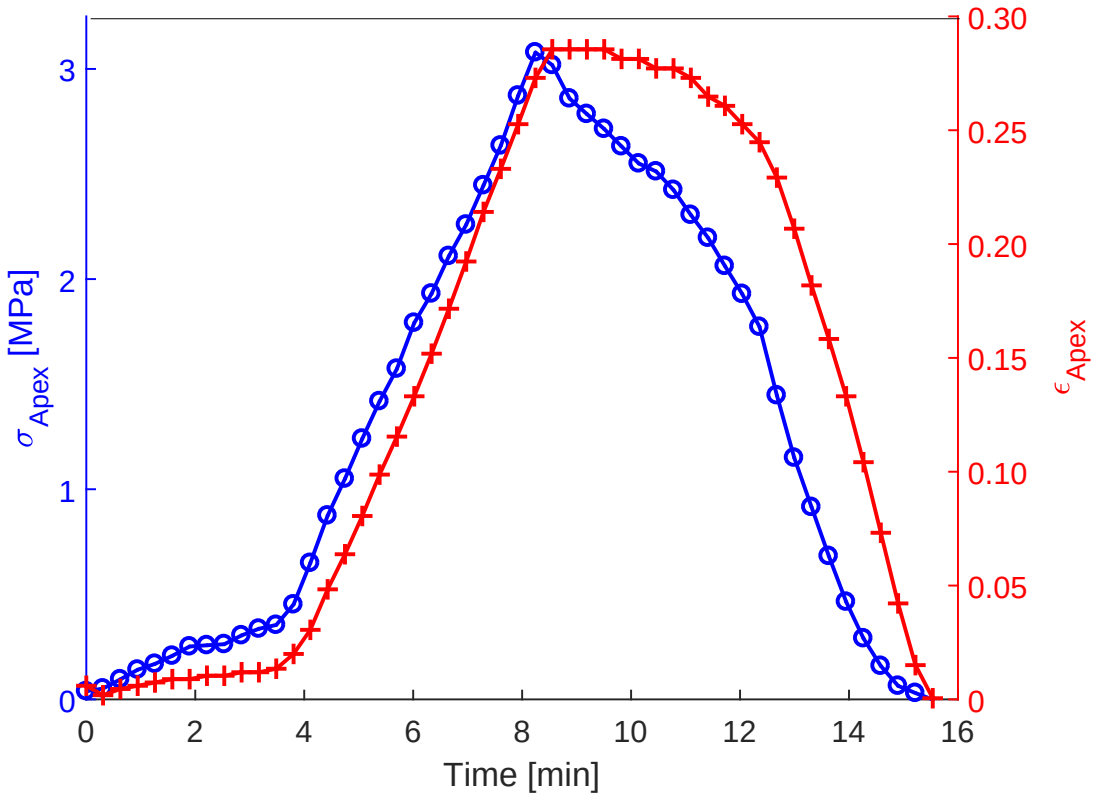


Figure 3.8: Time dependence of $\sigma_{\text{Apex}}$ and $\epsilon_{\text{Apex}}$ for the P-ref membrane over one cycle.

the pentablock copolymers presented in this study exhibit relatively high specific water permeability compared to other classes of high performance water treatment membranes[4,33,91,92], but measurable differences are obtained between the three different structures that we have investigated.

Equation 3.4 can be used to obtain a value of $a_0^2/\tau$ from these quantities, and these values are also included in Table 3.2. These can be compared to expected values of $a_0$ and $\tau$ to discern the degree to which the transport properties are optimized. The smallest possible value of $\tau$ is one, corresponding to either a homogeneous material with $\phi_{gel} = 1$, or a material with cylindrical pores aligned across the membrane. A value close to 2 for $\tau$ is generally expected for a randomly oriented and highly percolated structure[81,82]. The value of 3.6x10$^{-21}$ m$^2$ obtained for $a_0^2/\tau$ is consistent with expected values.

For example, Tokita and Tanaka obtain $a_0^2 \sim 10^{-21}$ m$^2$ for polyacrylamide gels[84]. While some variation in $a_0$ will be obtained for different types of polymer solutions, we do not expect substantial variations in this quantity[30]. Since $\tau$ must be greater than or equal to 1, we expect that the value of $10^{-21}$ m$^2$ is close to the upper limit for $a_0^2/\tau$. The fact that larger values of $a_0^2/\tau$ are extracted from the permeability data for the P-ref and P-sub samples may originate from our assumption that the polymer volume fraction within the pores is constant. In fact, we expect a lower polymer volume fraction in the centers of the pores, with enhanced water permeability in these regions. Our main point here is that Equation 3.4 provides a useful framework for understanding the overall factors controlling the water permeability in these systems.

| Polymer | Swelling [wt %] | $\phi_{gel}$ | $\phi_p$ | $k_m$ (m$^2$) | $a_0^2/\tau$ (m$^2$) |
|---|---|---|---|---|---|
| P-ref | 117 ± 7 | 0.61 | 0.11 | 6.1x10$^{-20}$ | 3.6x10$^{-21}$ |
| P-sub | 94 ± 4 | 0.54 | 0.11 | 2.9x10$^{-20}$ | 2.0x10$^{-21}$ |
| P-short | 45 ± 3 | 0.30 | 0.03 | 2.0x10$^{-20}$ | 3.4x10$^{-22}$ |

Table 3.2: Wet-state properties of the membranes based on tests of 9 samples of each type, including the membrane permeability, $k_m$. The reported $\phi_{gel}$ and $\phi_p$ values have standard deviations of less than 0.01.

This framework is particularly helpful for understanding the changes in the membrane permeability obtained when the degree of polymerization of the gel-forming sulfonated polystyrene mid-block is reduced from ≈270 in the P-ref sample to ≈60 in the P-short sample. This substantial reduction in the content of the water-swellable portion of the block copolymer leads to a surprisingly small decrease in the overall membrane permeability, with $k_m$ decreasing by a factor of 3. The decrease in $k_m$ is driven by the decrease in $\phi_{gel}$, and an associated increase in $\tau$[82]. This decrease is partially compensated by decrease in $\phi_p$, the polymer volume fraction within the swollen polyelectrolyte domains. The P-short polymer therefore consists of highly-swollen domains with a high intrinsic permeability and high tor-

tuosity in comparison to the P-ref or P-sub samples, resulting in the observed net decrease in $k_m$.

### 3.3.2 Creep Behavior of Hydrated Membranes

A series of stress-controlled creep tests was carried out to investigate the effect of the mid-block and end-block on membrane mechanical properties. During the initial inflation stage, which typically lasts several minutes, the membrane was pressurized with air until a target stress of $\sigma_{\text{apex}} \approx 2\,\text{MPa}$ is reached. The stress was then held constant at this target value for 60 minutes (Figure 3.9a). Figure 3.9b,c shows the apex area strain, $\epsilon_{\text{Apex}}$, and tensile creep compliance, D(t), for a P-ref membrane under this 2 MPa stress.

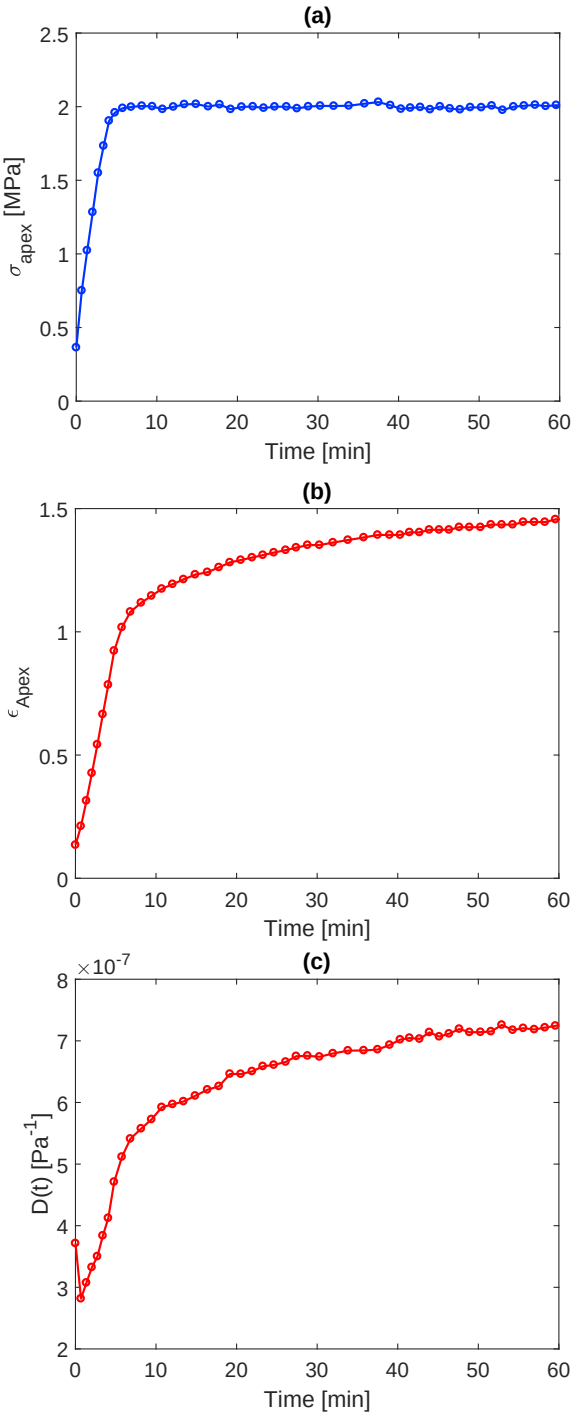


Figure 3.9: Creep behavior of a hydrated P-ref membrane for an applied biaxial stress of 2 MPa. (a) Stress; (b) strain; (c) creep compliance.

A characteristic creep rate is obtained by fitting the time-dependence of the strain in the later stages of the experiment to a straight line (Figure 3.10a). Similarly, a characteristic creep compliance of the membrane was obtained as the value of this quantity at a creep time of 60 minutes. Figure 3.10b shows a comparison of the strains for the three pentablock copolymers used in this study, with the characteristic creep rates and creep compliance values listed in Table 3.3.

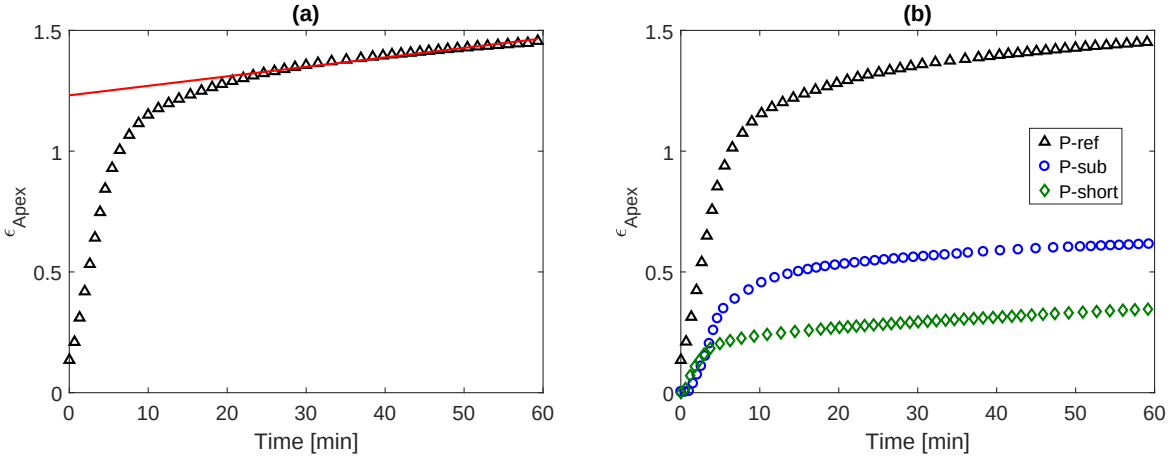


Figure 3.10: (a) Time dependent apex strain from Figure 3.9a, showing the linear fit to the long-time data from which we extract a characteristic creep rate. (b) Strain curves for P-ref, P-sub, and P-short membranes at an applied membrane stress of 2 MPa.

Both modifications to the original P-ref sample resulted in stiffer, less-compliant membranes. The reduction in the measured creep strain and characteristic creep strain rate for the P-sub pentablock system reveals that the chemical substituent on the alkyl-styrene end-block can have substantial effects on the mechanical response of the membrane. By switching from t-butylstyrene to p-methylstyrene end-blocks, the membranes become 60% less compliant (Figure 3.10b).

| Polymer | $\dot{\epsilon}_{Apex}$ $[s^{-1}]$ | $D_{60}$ [$Pa^{-1}$] | $1/D_{60}$ (MPa) |
|---|---|---|---|
| P-ref | 3.1x$10^{-3}$ | 7.3x$10^{-7}$ | 1.4 |
| P-sub | 2.0x$10^{-3}$ | 3.1x$10^{-7}$ | 3.2 |
| P-short | 1.7x$10^{-3}$ | 1.7x$10^{-7}$ | 5.9 |

Table 3.3: Characteristic creep rate and creep compliance obtained from the data in Figure 3.10. Results are within 10% error.

This result is consistent with creep experiments performed on bulk poly(t-butylstyrene) and poly(p-methylstyrene)[93], and can be explained by the increase in density of backbone bonds in the system when the bulky t-butyl group is replaced by a much smaller methyl group. An additional factor of two in the membrane stiffness was obtained by the substantial reduction in the molecular weight of the sulfonated polystyrene block represented by the P-short sample.

### 3.3.3 Cyclic Loading of Hydrated Membranes

Cyclic loading experiments were carried out to investigate the relative strain recovery of the different materials. Figure 3.11 shows the stress-strain curves of the pentablock copolymer membranes loaded under the cyclic loading protocol. The plastic strain after each cycle is plotted in Figure 3.12a. It is found that P-ref membranes have the highest relative recovery and are able to recover most of the deformation following each cycle, although these membranes are also the most compliant.

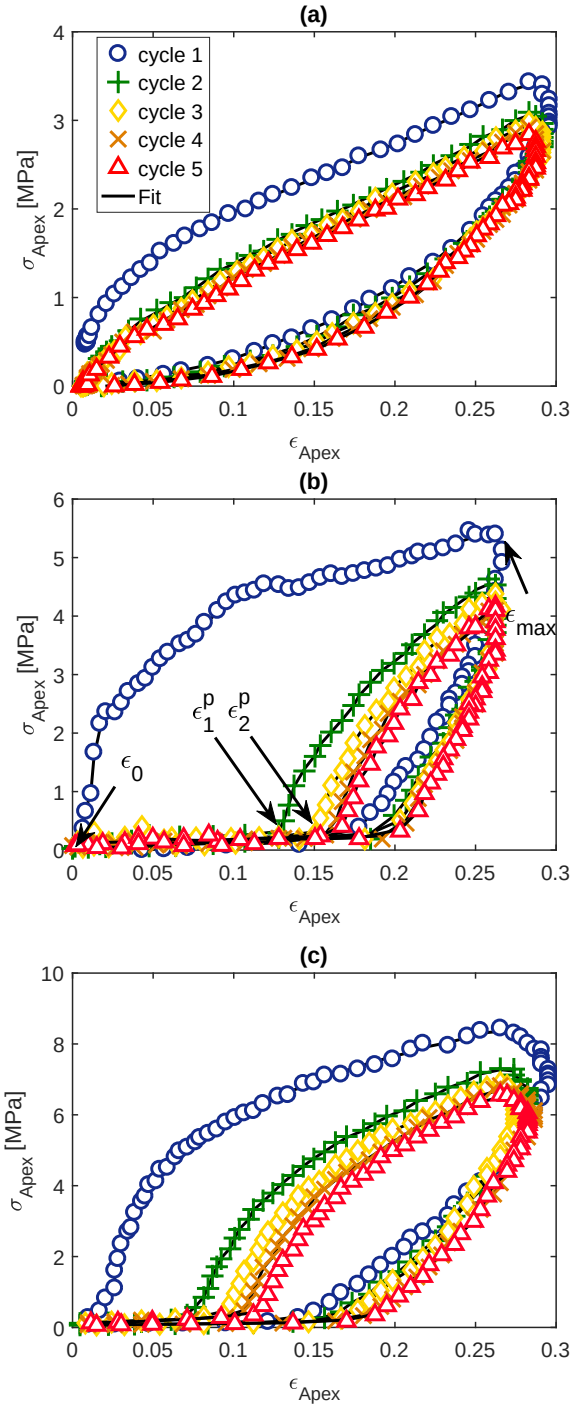


Figure 3.11: Stress/strain curves for (a) P-ref, (b) P-sub, and (c) P-short membranes tested for 5 cycles.

Conversely, while P-sub and P-short membranes are more resistant to deformation and creep, they undergo plastic deformation at much lower strains. The relative recovery of the strains experienced by the membrane is calculated as the amount of strain recovered per cycle after plastic deformation:

$$\text{Relative Recovery, RR}\,(\%) = \frac{\epsilon_{\max} - \epsilon_{\mathrm{N}}^{\mathrm{p}}}{\epsilon_{\max}} \tag{3.13}$$

The P-sub copolymer with the poly(p-methylsyrene) end-blocks has a much higher plastic strain after the first cycle than reference polymer with the poly(t-butylstyrene) end-blocks, corresponding to a lower relative recovery (Figure 3.12a,b). The P-short polymer has behavior intermediate between that of the two other polymers. In each case the additional plastic strain induced after subsequent cycles is relatively small, with relatively small effective phase angles representative of a material with an elastic character (Figure 3.12c).

The trade-offs between stiffness and permeability are illustrated in Figure 3.13, a cross-plot of the Young's modulus and water permeability for several different classes of materials used for water treatment. The values obtained in our experiments (Table 3.4) are comparable to reported values for similar sulfonated block polymer systems in the hydrated state (∼10-70 MPa wet,∼340-480 MPa dry)[11,94].

| Polymer | $\epsilon_{apex}^{plastic,\,f}$ $[s^{-1}]$ | $E\ [MPa]$ |
|---|---|---|
| P-ref | $<$0.01 | 25±2 |
| P-sub | 0.16 | 78±5 |
| P-short | 0.07 | 93±4 |

Table 3.4: Elastic modulus and total plastic strain obtained from the cyclic data from Figure 3.11.

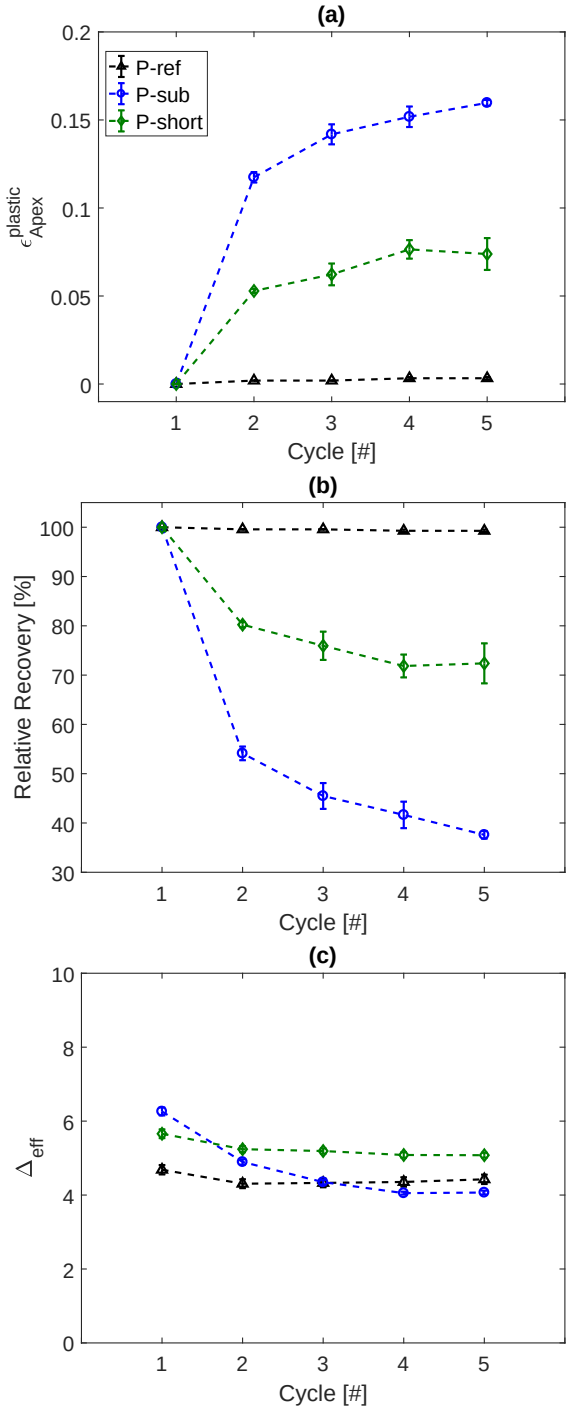


Figure 3.12: Membrane properties obtained from the cyclic stress/strain data from Figure 3.11: (a) total plastic strain; (b) relative recovery; (c) effective viscoelastic phase angle.

Despite having a significantly reduced MW of the sulfonated block, P-short membranes maintain comparable water transport properties while exhibiting the highest membrane stiffness and creep resistance compared to the other two pentablock systems. The modifications described in this paper represent a scheme for tuning the property balance in the property space occupied by these materials, which have water permeability values at the upper end of the full spectrum of available membrane materials.

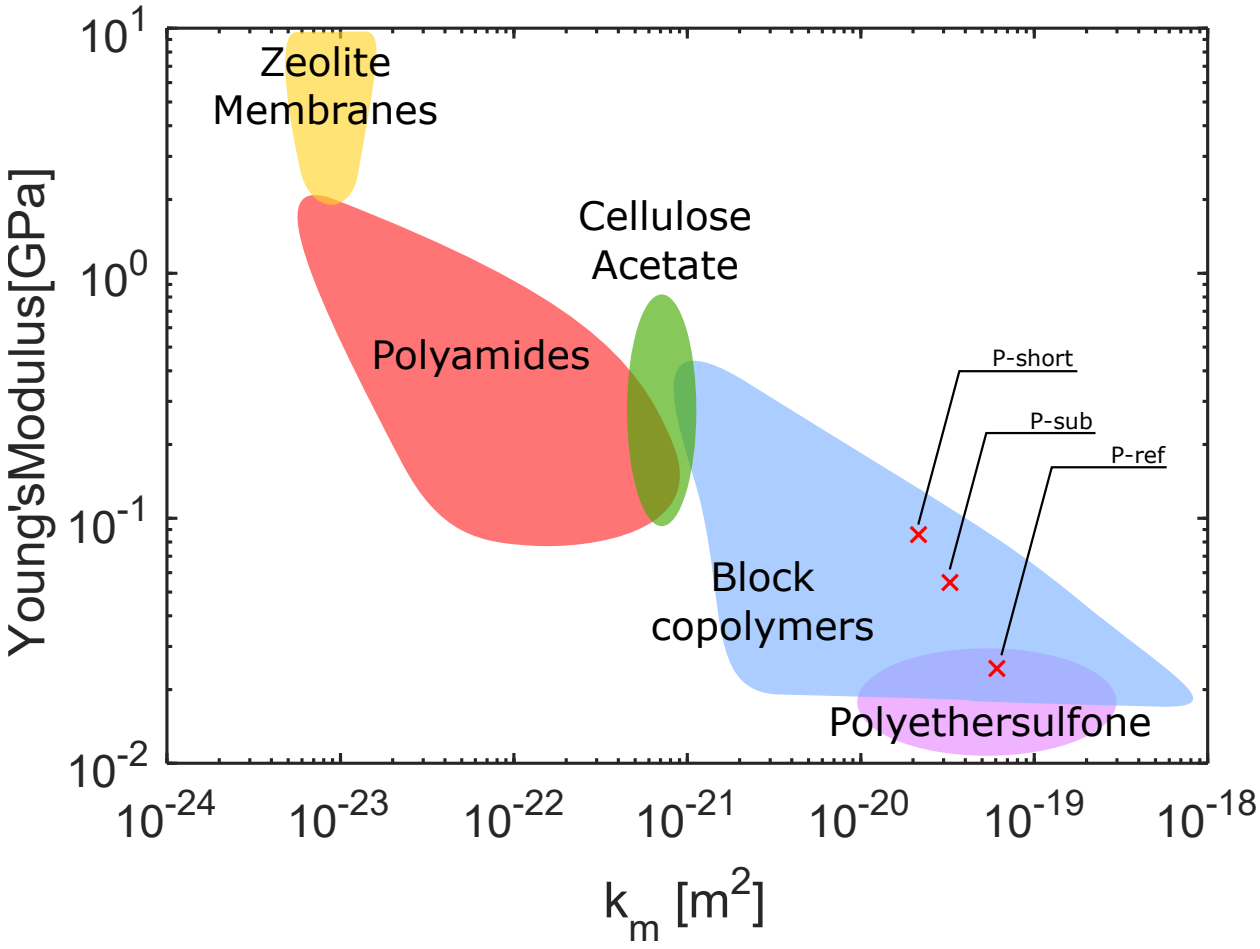


Figure 3.13: Cross-plot of the elastic stiffness and water permeability for common classes of nanofiltration and reverse osmosis membranes based on a review of current literature[4,33,91,92,95–103].

## 3.4 Conclusion

In this chapter, a cation exchange membrane fabricated from a commercial pentablock copolymer platform was explored using a non-traditional membrane inflation technique that specializes in investigating the mechanical behavior of the polymer membranes in hydrated conditions. The steady-state creep behavior of spin-coated membranes reveals a dependence of the membrane stiffness on the polymer's end-block chemistry and polymer molecular weights. In general, increasing sulfonation level leads to membrane softening. However, this effect can be mitigated by reducing the molecular weight of the sulfonated styrene mid-block. Additionally, modification of the end-block chemistry from t-butylstyrene to p-methylstyrene significantly reduces the membrane compliance. In both cases, the membranes maintained comparable water transport properties to the unmodified base pentablock copolymer.

# Chapter 4

# Structural Characterization of Sulfonated Pentablock Copolymers Using X-Ray Scattering Techniques

In addition to factors such as sulfonation level, molecular architecture, and block molecular weight, the structure of block-copolymers can be tuned by controlling the quality of the solvent species used to process the polymer.

In this chapter, the effect of the relative selectivity of the solvent on the polymer morphology of the pentablock sulfonated copolymer described in Section 3.2.1 is investigated. Previous work have discussed relationship between processing, structure, and membrane performance, and I hope to investigate the correlation further[11,22,31,46]. A combination of X-ray scattering techniques is used to provide insight into the evolution of structure from the solution to thin film. A binary solvent blend of contrasting solubility of the pentablock copolymer is employed to precisely tune the solvent selectivity. This tunability is especially evident when considering amphiphilic block copolymers in miscible polar/nonpolar solvent blends[104–107]. While the kinetics of this growth process are certainly important, determining the transition from the steady state characteristic micelle solution morphology as a result of the polymer/solvent interactions to solid thin films is another key part in fully understanding the process of block copolymer assembly.

## 4.1 Introduction

Ion exchange membranes (IEMs) have garnered increasing attention in the recent decade from simple materials in the laboratory to successful industrial products such as Nafion used in fuel cells[1,6–8]. Further, IEMs are often used in the desalinization of sea water, gas separation,

and chemical recovery in industrial effluents[9–12]. In most cases, IEMs transport ions across a conductive polymeric membrane while blocking the passage of water or other solvents. Although the ionic and water transport properties of IEMs are of the utmost importance to increase yield and reduce cost, the mechanical properties of these membranes which are often overlooked play a significant role in membrane performance and longevity[3,16]. Not only do IEMs need to maintain high ionic conductance or water transport rates, but they also need to have high mechanical strength to support large pressure differentials separating clean and feed water or reactive chemical intermediates[22].

Specifically, commercially available Nexar polymer with various sulfonation levels and end-block functional groups will be dissolved in a series of nonpolar, polar, and mixed solvents to selectively solvate the mid-block, the end-block, or both, respectively. The hydrophilic and hydrophobic domains will phase separate to form a variety of different ordered structures, depending on the polymer composition and solvent conditions. Previous studies explored the micellar structures for a range of sulfonation level using atomic force microscopy (AFM) and electron microscopy techniques. Choi and coworkers[42] explored the transport properties of the pentablock copolymer as a function of sulfonation level, but did not explore further the effects of solvent quality, polymer functionalization, and block size. They found that at lower levels of sulfonation, the sulfonated pentablock copolymer formed micelles on the order of ∼30nm with a sulfonated core. At increasing sulfonation levels, the micelles merge to form interconnect channels, leading to an improvement in transport properties. Griffin and coworkers[48] subsequently investigated the solution morphology of these sulfonated pentablock copolymers in binary mixtures of good and bad solvents. They found that higher order structures can be accessed when using polar solvents that can solvate the charged mid-blocks, but they did not explore further the effect of the morphological changes during solvent evaporation into solid films.

In the present work, X-ray scattering techniques are employed to develop a more accurate understanding of the dependence of sulfonation level, degrees of polymerization, block chemistry, post-processing methods, and polarity of casting solvents on the dynamics, structural evolution, and formation of a sulfonated pentablock copolymer. Earlier studies focused primarily on systems with a di-block design[41,63,80], in which a sulfonated block responsible for water and ion transport is attached to a second block that provides mechanical strength. In such cases, the degree of sulfonation is limited by the strength of the second block species. A higher degree of sulfonation leads increase water solubility of the polymer, which can be an undesirable effect as it leads to a loss of structural integrity[47].

The use of multi-block copolymers can lead to materials with relatively high degrees of sulfonation without sacrificing mechanical strength, since swelling issues of the ion-conducting segments can be mitigated by the additional segments which act to pin the ion channels. The structural tunability of the block copolymers also gives insight into the molecular underpinnings of order-disorder transitions approximated by Flory-Huggins Theory and self-consistent field theory[48,80]. With the establishment of powerful x-ray scattering techniques and non-traditional mechanical tests, the structure and the mechanical properties of ion-exchange membranes can be fully characterized[50–53].

Here, grazing-incidence X-ray scattering techniques are employed to investigate the domain size and morphology evolution of sulfonated block copolymers during solvent evaporation. Using grazing-incidence X-ray scattering (GIXS) at the Advanced Photon Source at Argonne National Lab (APS-ANL), the morphological evolution during solvent evaporation is monitor in real-time. Exploiting the incident beam angle in the grazing-incidence geometry, additional structural information can be obtained from both the surface and the bulk. A binary mixture of a polar and a non-polar solvent will be used to elucidate the dependence of the membrane micro-structure and morphology on solvent species and concentration. In polar solvents, the morphology of the micelles are expected to be inverted. Additionally, *in*

*situ* swelling experiments can capture the morphological changes between the dried and wet membranes.

Currently there is a limited understanding of how the continued swelling of the sulfonated styrene mid-block under high humidity environments contribute to membrane creep and mechanical strength degradation. It is believed that water channels will continue to swell during operation, leading to irreversible softening and membrane failure. The results will help to understand the mechanism of water and ion transport, and also guide the design of new membrane materials that can be more resistant to membrane creep and degradation during operation.

## 4.2 Experimental

### 4.2.1 Materials and Sample Preparation

Sulfonated pentablock copolymers used in this chapter have been discussed previously in 3.2.1, but with a few notable difference as highlighted in Table 4.1. The as-received polymer solutions provided by Kraton Polymers were dried in a vacuum chamber for 48 hours. The dried polymers were then redissolved in a series of binary/solvent mixtures composed of toluene (tol) and dimethylacetamide (DMAc) to make 3 to 3 wt% polymer solutions. Dimethylacetamide was selected as the polar solvent as it is a common processing solvent for making fibers or films in the adhesive industry. All samples were stirred on a magnetic stir plate at 60°C for 24 hr to ensure complete dissolution, and subsequently removed from the heat. The solutions are stirred until use.

| Sample | End-block | IEC [mequiv/g] | Sulf. Level [mol %] | Equivalent MW [kg/mol] |
|---|---|---|---|---|
| P-2.0 (P-ref) | tBS | 2.0 | 58.0 | 15-10-28-10-15 |
| P-1.0 | tBS | 1.0 | 29.0 | 15-10-28-10-15 |
| P-short | tBS | 0.67 | 62.8 | 16-10-6-9-13 |

Table 4.1: Summary of the sample compositions in the dry state, including sulfonation level and the equivalent MW of the polymer.

### 4.2.2 Atomic Force Microscopy

The prepared polymer solutions were spin-coated onto UV-O cleaned silicon wafer. Atomic force microscopy (AFM) (Bruker Dimension FastScan AFM, Bruker, Billerica, MA) was conducted in air using soft tapping mode. Standard silicon probes with pyramid tips were used for imaging.

### 4.2.3 Small-Angle X-Ray Scattering

Small angle X-ray scattering (SAXS) measurements were performed at Sector 5-ID-D of the Advanced Photon Source at Argonne National Laboratory. Previously prepared polymer solutions were sealed in 1.5mm diameter quartz capillaries and measured at room temperature. An X-ray energy of 10 keV was used, with a sample-to-detector distance of 8.5 m. Scattering patterns were captured using a two-dimensional CCD detector. Due to the high brilliance of the APS source, short exposure times of 0.5 - 1 s were used, depending on the scattering intensity, to capture scattering patterns and to minimize beam damage. The scattering from the capillary and the solvents are subtracted, and the resulting scattering intensity was corrected for the primary beam intensity. 2D scattering patterns were converted to 1D profiles using azimuthal angle integration and subsequently fitted with the Percus-Yevick hard sphere model[108], which uses a spherical form factor to describe the shape of the scattering

features. The analysis were made using the Irena computational package developed in Igor Pro for SAXS and SANS analysis[109].

### 4.2.4 Grazing-Incidence Small-Angle X-ray Scattering

Grazing-incidence small-angle x-ray scattering (GISAXS) enables *in-situ* observations of the size and organization of weakly-scattering polymeric thin films to give structural information of interfacial features[15,110]. The advantages to using the grazing-incidence x-ray scattering are manifold. First, the technique uses x-ray reflection geometry instead of transmission geometry. GISAXS is lauded as a highly surface sensitive technique that can probe a broad range of length scales by properly controlling the incident-angle and the distance between the sample and the detector[52]. Since x-ray scattering is a statistical measurement, it can provide more reliable and meaningful statistical information about the size distributions and length scales present in a larger area compared to direct imaging techniques such as atomic force microscopy (AFM). For polymeric thin films that have small scattering volumes, the reflection geometry allows for higher sensitivity to weakly scattering materials. Not only does GISAXS probe features on the surface, it can also provide structural information buried in the bulk and between interfaces.

Additionally, GISAXS enables time-resolved tracking of morphological developments of drying films cast from solution as the samples can be laid flat[52,110]. In order to resolve and capture the spatial and temporal dynamics that occur at small time-scales with good fidelity and high sensitivity, a synchrotron source with a highly collimated x-ray beam is needed. In the present work, GISAXS experiments were performed at Sector 8-ID-D of the Advanced Photon Source at Argonne National Laboratory. Samples were prepared by spin-coating the prepared polymer solutions onto Si substrates. The fabricated films are about 100 nm, measured using a high-resolution contact profilometer (Dektak 150, Veeco Instruments Inc.).

Sample alignments were performed using an avalanche photodiode (APD). X-ray scattering of the spin-coated films were collected using a 2-D detector (PILATUS 1M pixel array detector) with an X-ray energy of 7.35 keV ($\lambda = 1.69$ nm), and a sample-to-detector distance of 2.17 m. A silver behenate standard is used as reference. Typical incident angles for polymer thin films on silicon substrates are between the critical angles for total reflection of the film and the substrate. At a photon energy of 8 keV, the critical angles of the film and the substrate are$\sim 0.15°$ and $\sim 0.22°$, respectively. Under these conditions, the beam will penetrate the sample but reflect off the substrate, fully illuminating the sample volume along the footprint of the beam.

A typical GISAXS experiment measures the scattered electric field intensity from a sample in both the lateral (y) and the vertical (z) directions. In this geometry, $q_y$ is the scattering vector component parallel to the sample surface and perpendicular to the scattering plane, and $q_z$ is the component perpendicular to the sample surface.The difference between the incident and scattered wave vectors, $k_i$ and $k_f$, or the scattering vector, $\mathbf{q}$, can now be defined 3-dimensionally as:

$$\boldsymbol{q} = \begin{pmatrix} q_x \\ q_y \\ q_z \end{pmatrix} = \frac{2\pi}{\lambda} \begin{pmatrix} cos(\alpha_f)cos(\theta_f) - cos(\alpha_i) \\ cos(\alpha_f)sin(\theta_f) \\ sin(\alpha_i) + sin(\alpha_f) \end{pmatrix} \tag{4.1}$$

where $\alpha_i$ and $\alpha_f$ are the out-of-plane angles, and $\theta_i$ and $\theta_f$ are the in-plane angles ($\theta_i$ can be assumed to be 0). $2\pi/\lambda$ is the magnitude of the wave vectors $k_i$ and $k_f$. By setting $\theta_f = 0$ and $\alpha_i = \alpha_f$, the specular reflection condition ($q_x = q_y = 0$, $q_z = 4\pi\sin(\alpha_i)/\lambda$) can be achieved.

The scattered intensity, $I$, as a function of the scattering vector, q, can best be described using the distorted-wave Born approximation (DWBA) theory.

$$\mathrm{I} \propto \left|\mathcal{F}(\mathrm{q_y},\, \mathrm{k_z^i},\, \mathrm{k_z^f})\right|^2 \mathcal{S}(\mathrm{q_y},\, \mathrm{k_z^i},\, \mathrm{k_z^f}) \tag{4.2}$$

The DWBA theory provides a rigorous treatment of scattering in the GISAXS geometry, breaking it down into the structure factor $S$ and the form factor $F$, which describe the spatial correlation and the size of the lateral features, respectively (Equation 4.2). For example, nanoparticle additives used to enhance anti-fouling properties in IEMs[40] may be modeled using the Percus-Yevick approximation for 3-D hard spheres[111], or a model for 2-D structure on a surface[51]:

$$\mathcal{S}(\mathrm{q_y}) = \frac{1 - \exp(-2\mathrm{q_y^2}\sigma_\mathrm{d}^2)}{1 - 2\cos(\mathrm{q_y d})\exp(-\mathrm{q_y^2}\sigma_\mathrm{d}^2) + \exp(-2\mathrm{q_y^2}\sigma_\mathrm{d}^2)} \tag{4.3}$$

where d is the average separation distance between particles with a dispersion width of $\sigma_\mathrm{d}$. The form factor $F$ for spherical particles in a structure can be expressed by:

$$\mathcal{F}(\mathrm{q}) = \frac{4}{3}\pi \mathrm{R}^3 \left[\frac{\sin(\mathrm{qR}) - \mathrm{qR}\cos(\mathrm{qR})}{(\mathrm{qR})^3}\right] \mathrm{e}^{-\mathrm{iq_z R}} \tag{4.4}$$

where R is the mean radius of the particles. By considering one-dimensional cross-sectional slices of the experimental GISAXS patterns either in the $\mathrm{q_y}$ or $\mathrm{q_z}$ direction, the structure factor $S$ and form factor $F$ can be fitted to reveal information about the system. The form factor for SAXS and GISAXS may be different due to the scattering geometry. Scattering patterns collected in these experiments were processed with a beamline MATLAB program, which accounts for both the sample-to-detector distance and detector resolution, and produces intensity maps in the inline image plane ($\mathrm{q_y} - \mathrm{q_z}$). here, we consider line scans in the $\mathrm{q_z}$ direction. An average of pixels across $\mathrm{q_y}$ provides a higher signal-to-noise ratio and

provide a 1-D profile of the scattering intensity. The reciprocal-space momentum transfer, q, corresponds to a real-space distance, d, by:

$$q = 2\pi/d \tag{4.5}$$

### 4.2.5 Morphological Evolution during Solvent Evaporation

A blade-casting technique shown in Figure 4.1 is employed to capture the time-resolved structural evolution during solvent evaporation.

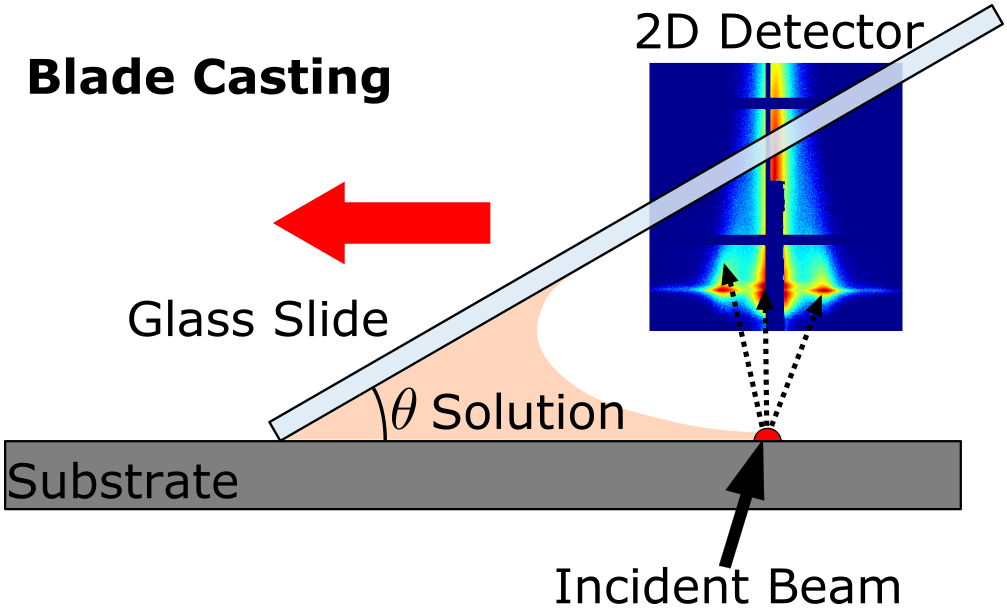


Figure 4.1: Schematic of the blade casting technique used for GISAXS experiments to investigate the microstructural evolution during solvent evaporation. Adapted from Laprade et al.[47].

A syringe pump (NE- 1000 syringe pump, New Era Pump Systems Inc, Wantagh, NY) is modified into a simple translation stage with a glass slide attached at a fixed angle, $\theta$ ($\sim 30°$). The glass slide is pushed across a Si substrate centered on the path of the incident x-ray beam on a static stage at a fixed rate (180 mm/min). Polymer solution is injected onto the backside of the glass slide via Teflon tubing from a second syringe pump (NE- 1000

syringe pump, New Era Pump Systems Inc, Wantagh, NY), creating a meniscus between the slide and substrate. A thin film of solution is deposited as the slide is translated across the substrate. The deposited film is approximately $80 - 100\,\text{nm}$ thick, depending on the polymer concentration and solvent composition. GISAXS scattering pattern is recorded approximately every 0.5 second, with an exposure time of 0.5 s. Images were processed with a beamline MATLAB program.

## 4.3 Results and Discussions

### 4.3.1 Solution Morphology

The solution morphology of sulfonated pentablock copolymers in tol:DMAc binary-solvent mixtures is investigated using small angle X-ray scattering (SAXS). Figure 4.2a presents the 1-D scattering patterns for 3 wt % polymer solutions in pure toluene for all three samples. The scattering patterns exhibit a broad first order primary peak, q*, centered near 0.1 $nm^{-1}$, followed by a weak shoulder. The location of the primary peak in each SAXS profile relates to the characteristic spacing (Equation 4.5) of the morphology. The absence of sharp peaks indicate minimal long-range ordering of the features.

The features of the scattering profiles were characteristic of spherical aggregates with a less dense coronal region of the non-ionic blocks. A liquid-like distribution of hard spheres is used to describe the spatial distribution of these aggregates. If we assume the contribution from the structure factor S(q) is negligible at higher q values beyond the primary peak, the scattering profile can be modeled with the appropriate hard-sphere form factor, P(q):

$$\mathrm{P(q)} = \left[3\left(\frac{\sin(\mathrm{qR})}{\mathrm{qR}} - \mathrm{qR}\cos(\mathrm{qR})\right)\right]^2 + B \tag{4.6}$$

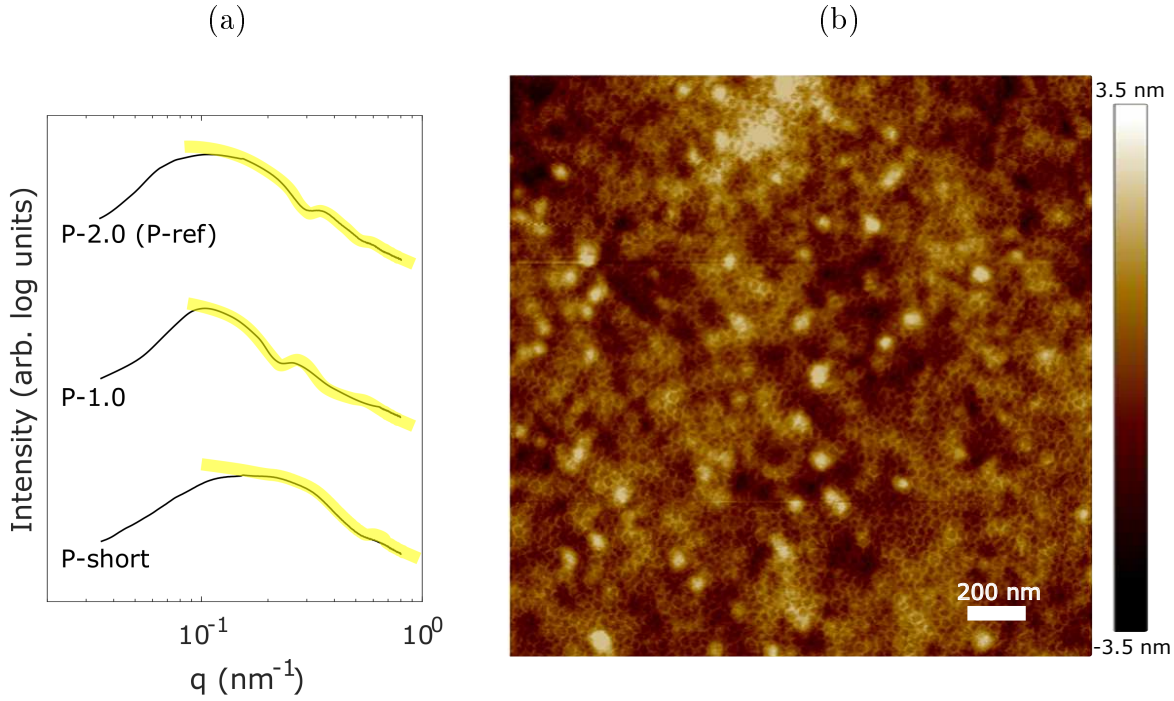


Figure 4.2: (a) SAXS profiles of all three samples dissolved in 100% toluene. The thick yellow lines represent model fits of P(q) from Equation 4.6. (b) An AFM micrograph of P-ref film spin-coated from toluene. Spherical features with diameters of $31.3 \pm 2.1$ nm are observed. Scale bar is 200 nm.

where B is the background. The model yields core radii of 10.3, 13.7, and 8.5 nm for P-1.0, P-2.0, and P-short, respectively. The resulting domain spacing constitutes the center-to-center distance between adjacent micellar cores is calculated from the primary peaks, and measures 30.8, 31.2, and 27.3 nm for P-1.0, P-2.0, and P-short, respectively. The values for P-1.0 and P-2.0 compare favorably with those previously reported[42,47] for similar pentablock copolymers cast from the as-received cyclohexane/heptanes (CH) mixture. Surprisingly, despite having a significantly smaller sulfonated styrene mid-block, the domain spacing for P-short remains comparable to the reference polymer, suggesting the packing of the micelles are driven by the non-ionic tBS-HI blocks. The AFM micrograph for P-ref cast from pure toluene in Figure 4.2b reveals features made up of irregularly dispersed micelles with a SS

core and a tBS-HI corona. This disordered micellar structure present in the film is consistent in all the samples cast from toluene.

Binary solvent mixtures were prepared by adding increasing amounts of dimethylacetamide (DMAc), a polar solvent commonly used in industrial processing. The solution morphology of P-ref in these binary solvent mixtures exhibit three distinct types of scattering patterns that change depending on the concentration of DMAc in the solvent blend, as shown in Figure 4.3a.

(a) (b)

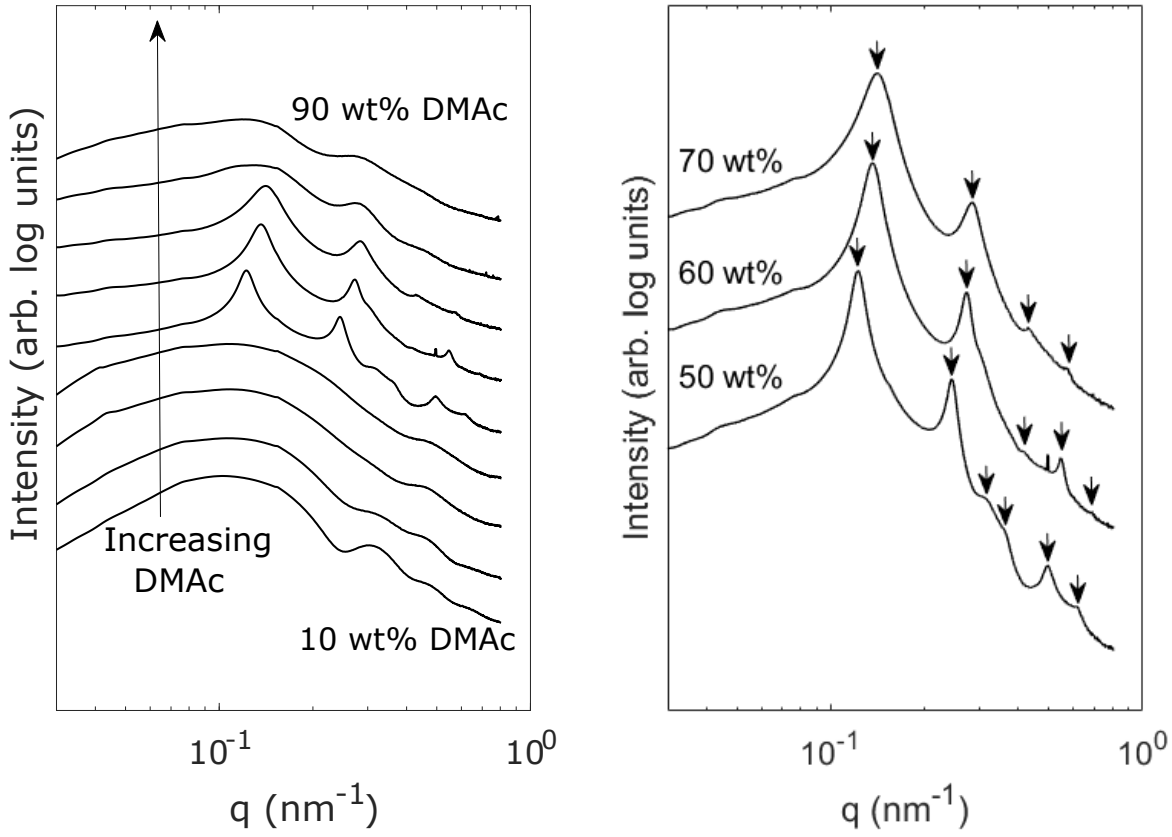


Figure 4.3: (a) SAXS Measurements of 3 wt% P-ref in binary solvents. (b) SAXS profiles of P-ref in 50 to 70wt% DMAc highlighting the higher order peaks discussed in text.

At low DMAc concentrations (0 to 40 wt%), the scattering profiles changes minimally from pure toluene, which were characteristic of spherical aggregates. At 50 to 70 wt% DMAc, higher order peaks can be observed, as shown in Figure 4.3b. The arrows mark the distinct higher ordered peaks in the scattering pattern at $2q^*$, $3q^*$, $4q^*$, and $5q^*$, which is indicative of an alternating lamellae morphology with a domain spacing of 51.5 nm at 50wt% DMAc. Weak shoulders are observed at $\sqrt{7}q^*$ and $\sqrt{12}q^*$ for 50 wt% and 60 wt% DMAc solutions, respectively, suggesting coexistence of hexagonally packed cylinders with the ordered alternating lamellae. This increase in the domain spacing is caused by swelling of the sulfonated block by the polar solvent. However, the domain spacing decreases (from d = 56.5 nm to 44.7 nm) with increasing solvent polarity as a result of DMAc being not a great solvent for the non-ionic tBS-HI end-blocks. The domain spacing of 44.7 nm at 70 wt% DMAc compares favorably to literature values for sulfonated pentablock samples exhibiting alternating lamellae structure[112]. For solvent compositions of predominantly polar DMAc (>80 wt%), the morphological ordering of the solutions decrease substantially, and characteristics of inverted spherical micelles ($d = 33.6 \pm 1.5$ nm) is observed.

At high concentrations of the polar solvent DMAc, an inverted micelle structure with a non-ionic core is expected. In this scenario, since the sulfonated mid-block can form loops that terminate at the core of the micelle, or they can form bridges that cross between two micelles due to constrained by the uncharged end-blocks. These solutions are found to be optically opaque and settled over time, which suggests precipitation and macroscopic aggregation in solution. For P-1.0, no higher order peaks were observed at the solvent compositions tested. Since the mid-block was less sulfonated than P-ref, the effects of DMAc is less pronounced. Nevertheless, a final morphology of inverted micelles ($d = 32.2 \pm 2.1$ nm) is observed. For P-short membranes, higher order peaks were observed for 80 to 100wt% DMAc (from d = 38.7 to 32.4 nm) and no additional peaks for DMAc <70 wt%. The lower

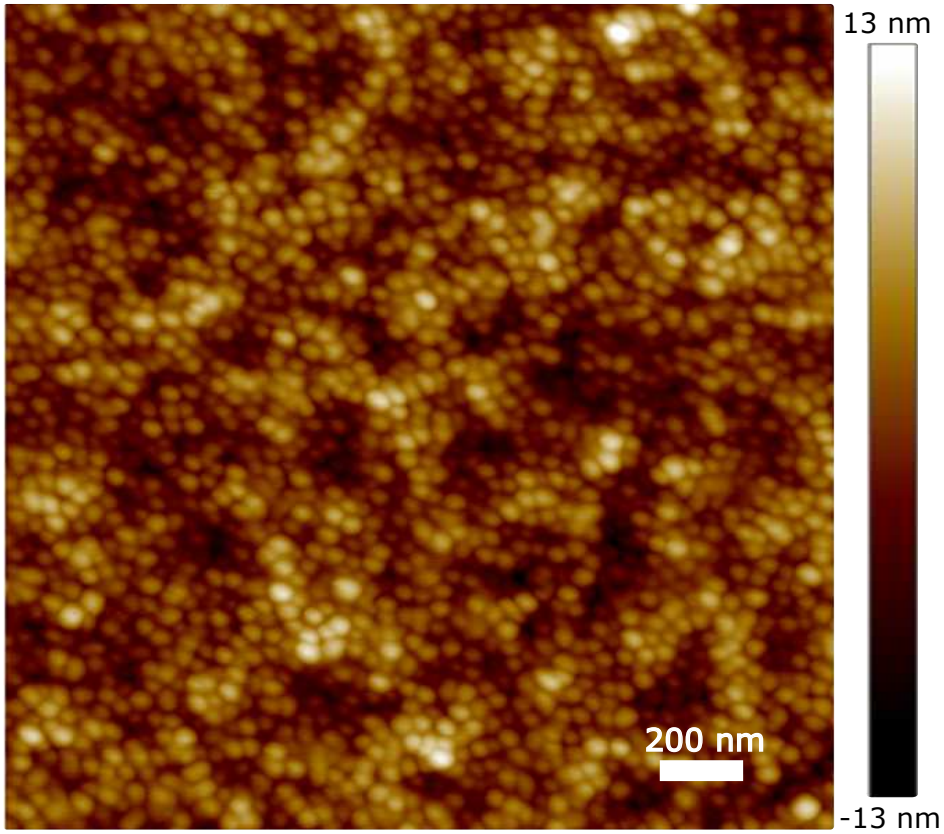


Figure 4.4: AFM micrograph of P-ref film spin-coated from DMAc. Spherical features with d = 32 nm are observed. Scale bar is 200 nm.

maximum domain spacing is reflective of the shortened mid-block (from 28k to 6k), but it nevertheless highlights the role solvent quality can have on solution morphology.

### 4.3.2 Morphological Evolution During Solvent Evaporation

A multitude of studies have investigated the solution morphology of the sulfonated pentablock copolymers as a function of polymer concentration, sulfonation level, and solvent quality. However, the morphology of the resultant polymer structure once the solutions are cast is still unclear. As solvent evaporates, the resulting membrane morphology should be equivalent to the existing solution morphology (Figure 4.5). We've employed an in-situ blade

casting technique to capture the evolution of morphology of pentablock copolymers during solvent evaporation using GISAXS technique.

Figure 4.6 shows the scattering pattern during solvent evaporation of a P-ref film cast from toluene. At time $t = 0$ s, the glass slide has just passed the path of the beam, and $t = -1$ s is used to demarcate all times prior to film deposition. Due to the high vapor pressure of toluene, the film dries quickly and the development of the scattering peaks occurs seconds after the wet film is deposited. When a film cast from DMAc, the evolution of the peaks is significantly slower due to the low vapor pressure of DMAc.

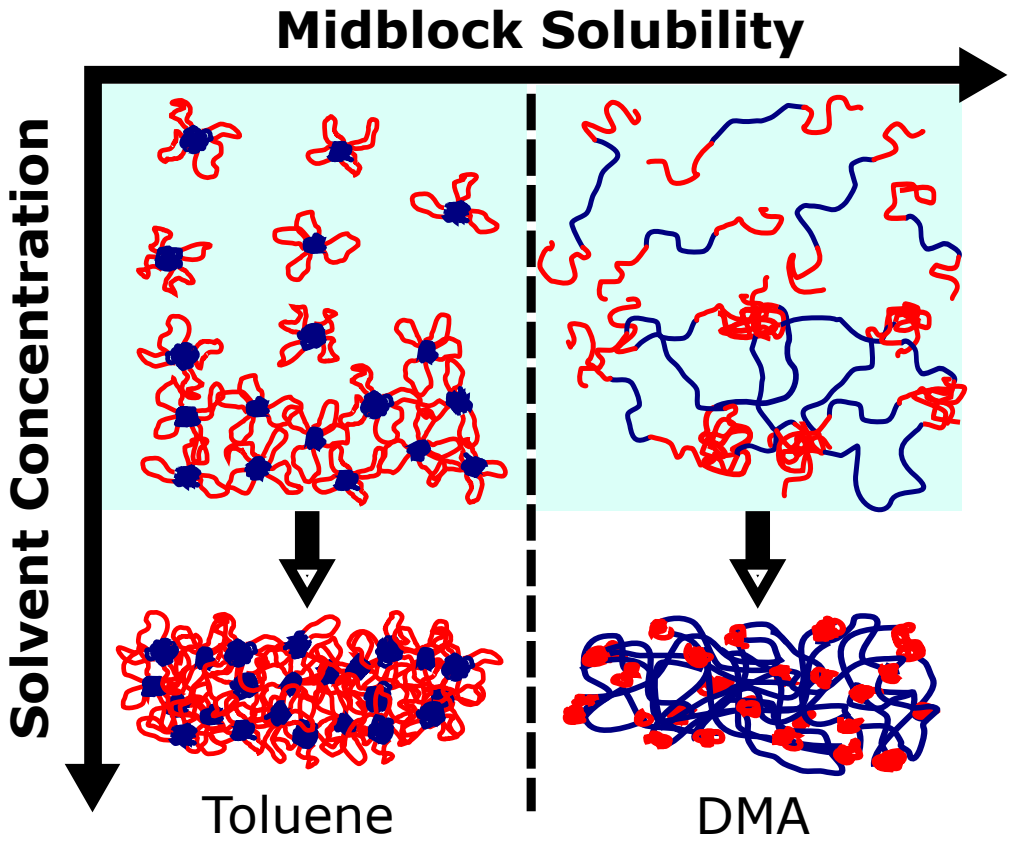


Figure 4.5: Schematic showing the packing of existing structures in solution as solvent evaporates as a function of the solvent quality for the sulfonated mid-block.

It should be noted that when cast from toluene, the micellar structure observed in the previous SAXS results is present in the wet film of P-2.0 at short times. As the film dries, the

initially weak first order peak broadens and shifts to higher q as a weaker second order peak forms, both of which are indicative of increase packing density of disordered spherical micelles forming the polymer film. The disordered packing of the micellar features are consistent with those seen in the AFM micrograph.

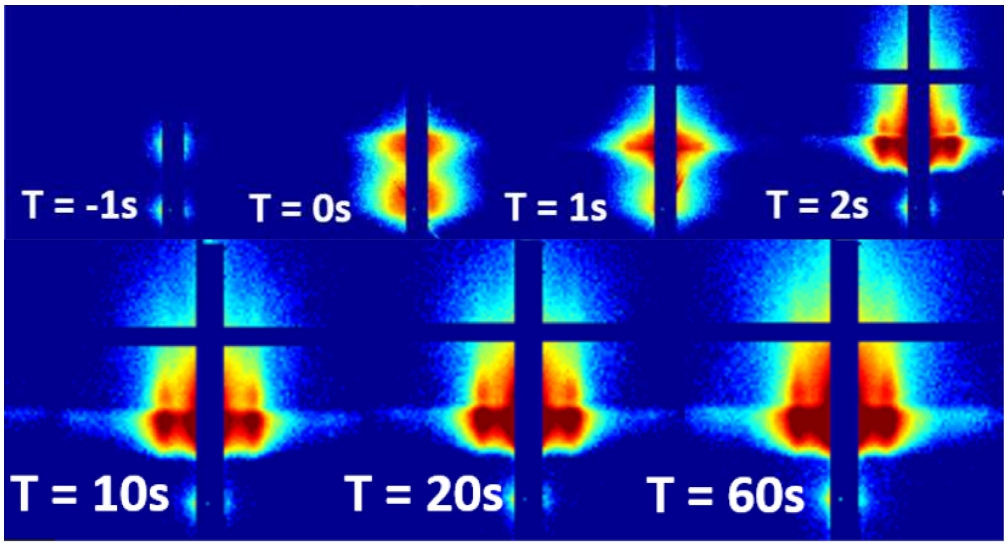


Figure 4.6: GISAXS scattering patterns during solvent evaporation for 1 wt% P-ref cast from pure toluene. Time, t = 0s, corresponds to right after the glass slide has past the path of the beam.

Scattering patterns for P-1.0 cast from solutions containing low concentrations of DMAc reveal no initial structure, which is indicative of a polymer in a good solvent. As polymer concentration increases due to solvent evaporation, the ionic mid-blocks agglomerate to form micellar structures that pack down as the film dries. The domain spacing measured from GISAXS scattering spectra range between 45 to 52 nm for films cast from solvents containing DMAc concentration below 50 wt%.

At higher DMAc concentrations, minimal solution scattering is observed for the wet film cast from DMAc, suggesting a time dependent agglomeration of the polymer solution. It is possible that during the blade casting process the solution morphology could have been disturbed, but additional studies are required to draw any definitive conclusions. Higher

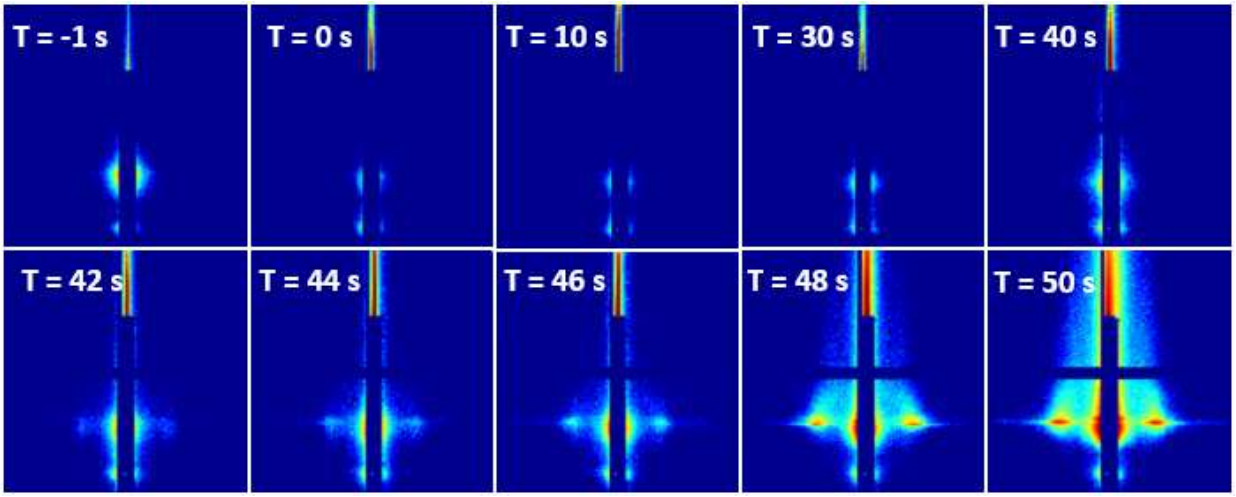


Figure 4.7: GISAXS scattering patterns during solvent evaporation for 1 wt% P-ref cast from pure DMAc.

order hexagonally packed cylinders and lamellae structure were not observed during solvent evaporation from solutions containing high concentrations of DMAc. Due to the discrepancies between the vapor pressure of toluene and DMAc, it is likely that in the binary solvent mixtures containing predominantly DMAc, most of the toluene will evaporate first before DMAc. The resulting films cast using this method have morphology and domain spacing consistent with those spin-coated from pure DMAc, and shows a inverted micelle structure with $d = 29.1 \pm 1.3$ nm. Our findings are in good agreement with those reported by Griffin *et al.*[48] detailing the micelle size and volume fraction of these sulfonated block copolymers in an increasing polar environment. They reported a micelle size of 26 nm at a solvent composition of 90 wt% n-propanol in toluene, and no values were reported for 100 wt% n-propanol.

The discrepancies in the domain spacing between SAXS and blade-coated membranes at low DMAc concentrations can be attributed to membrane processing. In order to prepare the casting solutions for blade-casting, polymer solutions used in SAXS experiments were diluted down to 1 wt% polymer solutions. Figure 4.8 shows the domain spacing calculated from GISAXS spectra collected from blade-coated samples cast from the binary solvents

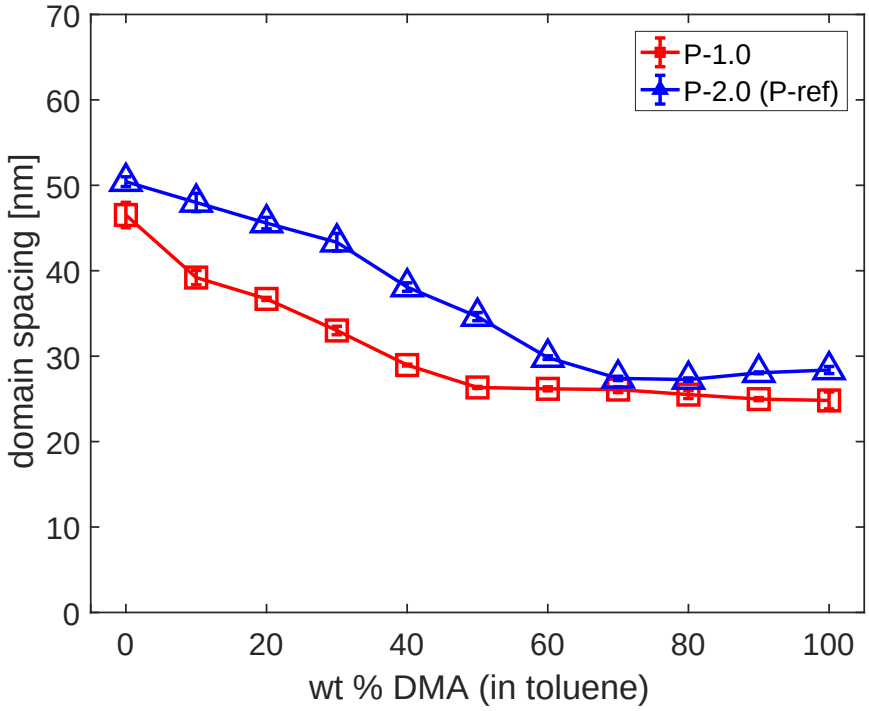


Figure 4.8: The domain spacing of blade-coated films of P-1.0 and P-2.0 (P-ref). The domain spacing decreases with increasing polarity of the casting solvent.

used in the SAXS experiments. In toluene, the sulfonated mid-block is not well solvated and will phase-separate to make up the micellar core. These ionic cores will agglomerate to minimize the high surface energy during film drying. However, as the film dries rapidly during spin-coating, the solution morphology is disrupted, and the resulting film is trapped in a non-equilibrium structure. DMAc has a low vapor pressure, making it a difficult solvent to spin-coat uniform films, the slow rate of film drying allows the formation of structures that are more energetically favorable. Consequently, as the polarity of the solvent blend increases, the domain spacing approaches a minimum size of 29 nm and 27 nm, for P-1.0 and P-2.0(P-ref), respectively, which is in good agreement with the SAXS data. P-1.0 has a weaker dependence on solvent polarity than P-2.0 as it contains a lower sulfonation level and therefore less charged functional groups. It is worth noting that is it difficult to fabricate uniformly smooth

films using the prepared P-short solutions due to polymer precipitating out before the wet film dries completely at high concentrations of DMAc (>60 wt%). Nevertheless, GISAXS spectra of P-short cast from 60 wt% DMAc yields an average domain spacing of d = 33.5 nm that is reminiscent of the domain spacing for spherical micelles.

### 4.3.3 Solvent Vapor Annealing and Membrane Swelling

#### Solvent Vapor Annealing

We've shown that the selection of suitable solvents is crucial in obtaining desirable membrane morphology. However, the positive effects on solution morphology in a good solvent system can be obviated during processing. As demonstrated in the previous section, the most appropriate solvent candidates for the sulfonated pentablock are those that have high solubility for all interacting species. Unfortunately, Due to the complex amphiphilic nature of the pentablock copolymers, it is difficult to predict a single solvent species appropriate for dissolving the material while being indiscriminate of the block chemistry. Neither the non-polar toluene nor the highly polar DMAc are capable of accessing solution morphologies containing high degrees of ordering, and only a combination of both polar and non-polar characteristics was effective. Therefore, it is likely that a potential solvent candidate would be moderately polar to be able to indiscriminately dissolve the participating blocks in this multi-block design. After a sampling of common laboratory solvents with moderate polarity, we found that both tetrahydrofuran (THF) and methylene chloride dissolve the ionic and non-ionic domains of the sulfonated pentablock. In this work, THF was selected as the annealing solvent.

A schematic of the atmosphere chamber used for our in-situ solvent annealing experiments is shown in Figure 4.9. Multiple reservoir pockets enable high surface areas for evaporation.

The heating element maintains the testing temperature to drive or prevent condensation during swelling experiments.

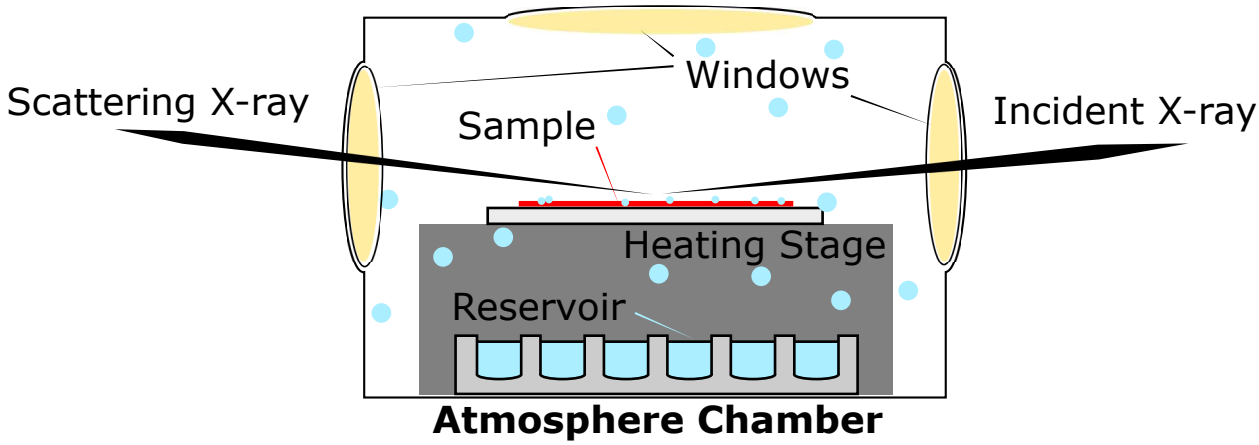


Figure 4.9: Schematic of an atmosphere chamber designed for in-situ annealing and swelling measurements.

Figure 4.10a shows the time-dependent evolution of the membrane morphology during an hour long in-situ solvent annealing experiment for a P-ref membrane cast from DMAc. The initial structure of the film consists of inverted micelles with domain spacing of 28.7 nm. As annealing increases with time, the primary peak shifts to lower q, indicating an increase to the domains spacing and swelling of the ionic domain. Higher order peaks at $2q^*$, $3q^*$, and $4q^*$ begin to appear and increase in intensity with increasing annealing time. In contrast, annealing of a P-ref membrane cast from toluene (Figure 4.10b) exhibit less long range ordering. Bulk of the peak development occurs within the first 10 min of annealing. In both cases, the primary peak position, $q^*$, decreases with increasing annealing time, signifying swelling of the micelles until a final domain spacing of around 44 nm consistent with those of alternating lamellae is achieved. Perhaps more useful in improving our fundamental understanding of the transformation process of the membrane morphology is the increasing peak intensity of the higher order peaks that is indicative of increasing long-range periodicity.

(a) (b)

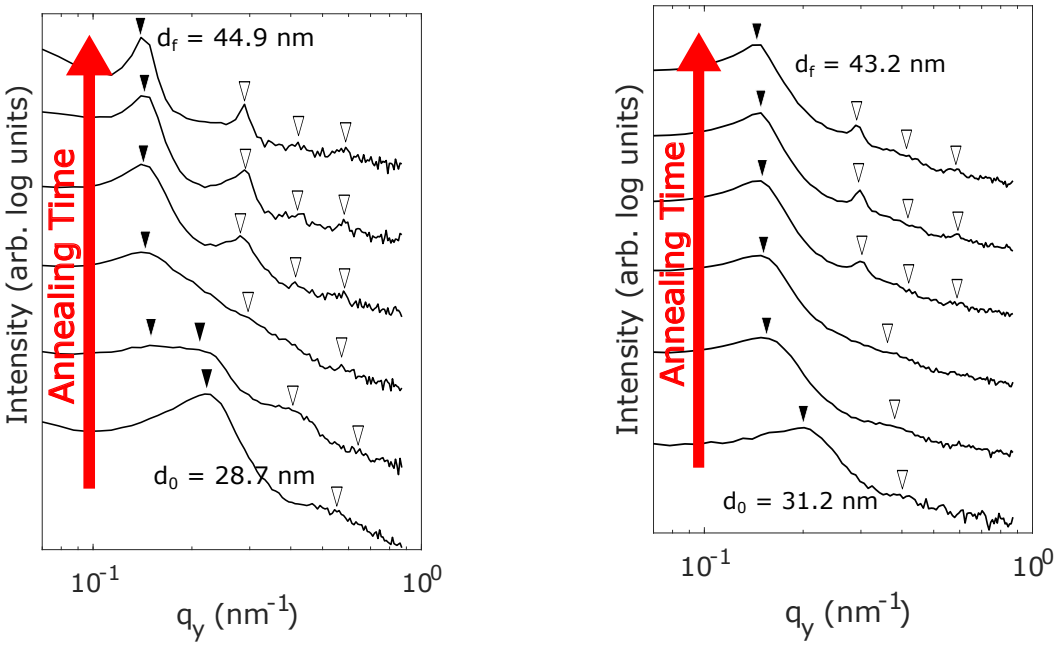


Figure 4.10: Time-dependent GISAXS profiles for in situ solvent annealing of a P-ref film cast from (a) pure DMAc and (b) pure toluene.

Compared to a P-ref sample annealed for 24 hours (Figure 4.11a), our hour-long in-situ annealing experiments are insufficient for the complete conversion of disordered micelles into a mixed morphology of ordered lamellae (with peaks at $2q^*$, $3q^*$, and $4q^*$) and hexagonally packed cylinders (with additional peaks at $\sqrt{3}q^*$, $\sqrt{7}q^*$ and $\sqrt{12}q^*$). It is evident that for P-ref, exposure to an annealing solvent such as THF enables the morphological transformation from disordered micelles to ordered lamellae and cylindrical structures, independent of the casting solvent used.

The same solvent annealing process can be applied to P-short membranes to obtain interconnected channels as shown in the AFM micrograph (Figure 4.11b) with domain spacing of $d = 47.6 \pm 4.7$ nm. The observed morphology was not present in SAXS spectra, and highlights the important role of solvent quality and selectivity in obtaining unique morphologies.

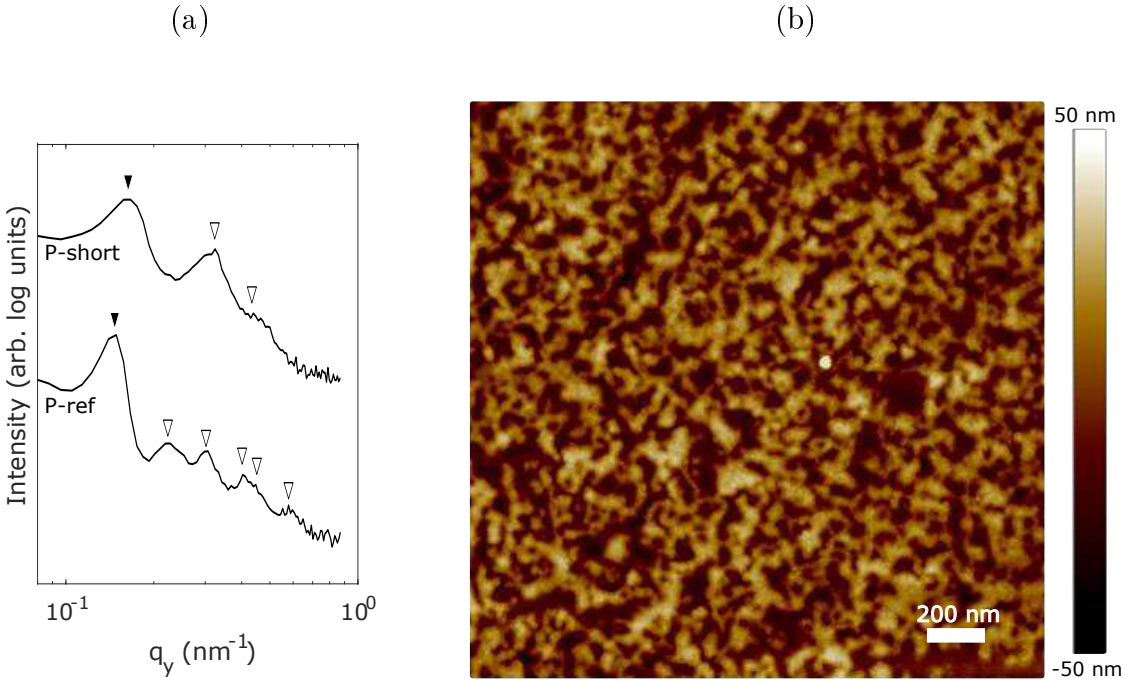


Figure 4.11: (a) GISAXS profiles for P-ref and P-short membranes annealed for 24 hours. (b) AFM micrograph of a P-short membrane annealed in THF.

While these images provides an estimation of domain spacing, it is not immediately obvious what block segments correspond to the high intensity and low intensity regions. We must therefore be cautions to not over-interpret the AFM images, and rely on other more suitable imaging techniques such as tunneling electron microscopy (TEM) with selectively stained domains to determine the long range morphology as demonstrated by Mineart and coworkers[112].

### Morphology-Dependent Membrane Swelling

Thus far, this study has focused largely on the morphological evolution of S-PBC membranes as a function of solution processing and solvent quality. Although it is useful to control the morphology of our thin films through solvent annealing processes, is it perhaps of more practical interest to understand how membrane morphology affect transport properties. Using the environmental chamber shown previously (Figure 4.9), in-situ water swelling experiments

were carried out for P-ref membranes before and after solvent vapor annealing. A Filmetrics reflectometer (Filmetrics Inc., San Diego, CA) was positioned above the top chamber window to capture the changes in membrane thickness during membrane swelling.

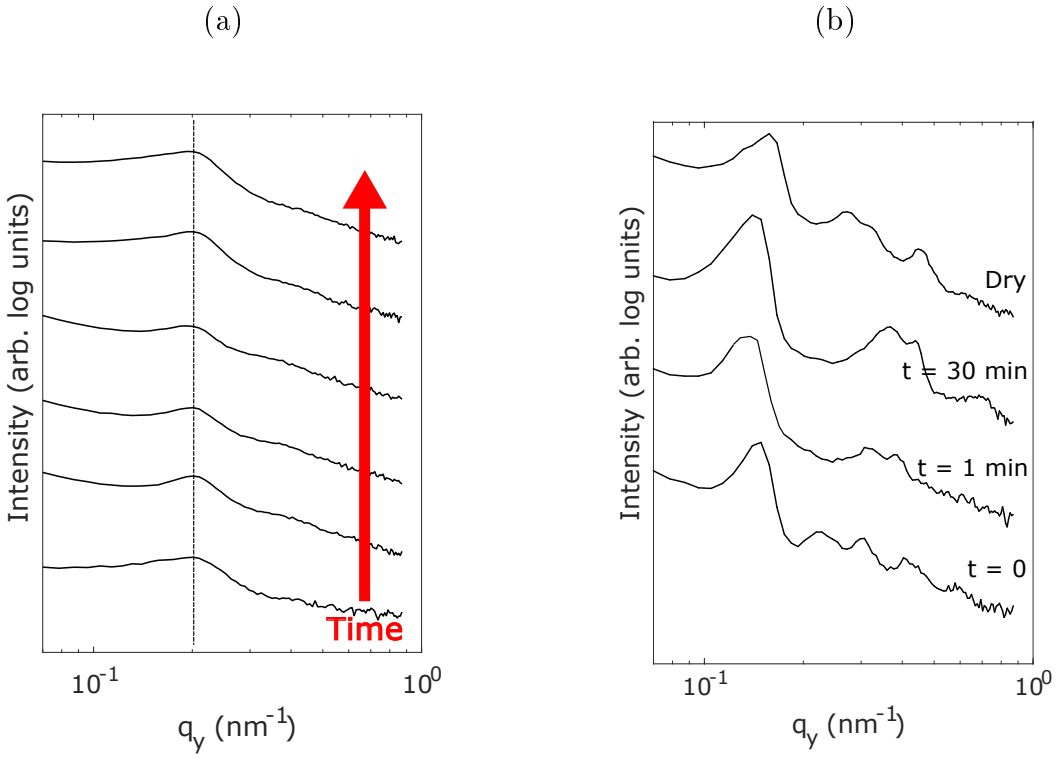


Figure 4.12: Time-dependent GISAXS profiles for (a) unannealed and (b) annealed P-ref membranes at 100% humidity.

Figures 4.12a and 4.12b show the time-dependent swelling of P-ref membranes cast from pure DMAc before and after solvent vapor annealing in THF for 24 hr. When exposed to a 100% humidity air, membrane thickness increases around 120% for an unannealed membrane, which is consistent with water uptake measurements shown in Chapter 3. Surprisingly, GISAXS profiles reveal only minimal changes to the primary peak position during swelling, implying that the overall center-to-center distance does not change as the ionic domains swell with water. On the other hand, an annealed membrane reveal significant morphological changes when exposed to 100% humidity air. As swelling increases, the domain spacing also

increases, from $d$ = 39 nm (at t = 0) to $d$ = 48 nm (at t = 30 min). The membrane morphology is also altered during swelling from lamellae to cylinders as indicated by the the significant changes to the higher order peak positions. Additionally, membrane thicknesses increased by close to 200% in the annealed membrane. The original membrane morphology is partially recovered as the membrane is heated up to drive off the absorbed water. As shown in the GISAXS profiles, when water is present in the P-ref membranes, a membrane morphology of mixed cylinders and lamellae is observed.

Water transport measurements of solvent annealed P-ref membranes were made at room temperature using a stainless-steel dead-end stirred cell (XFUF04701 Solvent-resistant Stirred Cell, EMD Millipore, Billerica, MA). Preliminary permeability measurements of annealed P-ref membranes reveal no improvement to the overall water permeability ($k_m = 5.8 \times 10^{-20} \pm 0.6 \times 10^{-20}$ m$^2$ ) when compared to our previously reported permeability values for unannealed P-ref membranes (($k_m = 6.1 \times 10^{-20}$ m$^2$ ). Our findings suggest that although membrane morphology can affect water uptake, and likely the mechanical strength, of the sulfonated pentablock copolymers, it may play a less significant role on the water permeability than expected. It may be useful to compare the mechanical strength and deformation behavior of annealed and unannealed membranes in future studies.

## 4.4 Conclusion

In this chapter X-ray scattering techniques were employed to characterize the solution morphology and morphological evolution of mid-block sulfonated block ionomers as a function of solvent quality and selectively. It was revealed that block ionomers can become trapped in non-equilibrium morphologies due to incompatible solvents or membrane processing techniques. A solvent vapor annealing process was introduced to provide an alternative method to unlocking equilibrium morphologies even with undesirable casting solvents or methods.

Specifically, we demonstrated that disordered micelle and inverted micelle structures can be converted into a mixed lamellar and cylinder morphology using THF vapors. In addition, in-situ measurements of membrane annealing and water swelling were conducted along with preliminary water permeability tests to further elucidate the structure-properties relationship. Solvent annealed membranes exhibited an enhancement to water uptake. Surprisingly, preliminary water permeability measurements reveal minimal effect on water transport, suggesting that the water transport mechanism is independent of membrane morphology.

In combination with the findings from Chapter 3, we have described a comprehensive approach to characterizing the the processing-structure-properties relationship of a unique ionomeric block copolymer. that can be applied to more efficiently design and optimize novel ionomers for water treatment applications.

## 4.5 Acknowledgments

Technical support for performing the X-ray scattering experiments were provided by the wonderful staff scientists at the Advanced Photon Source at Argonne National Lab. Special thanks Josh Yeh, Yaoyao Chen, David Delgado, and Kazi Sadman, who have provided much of both scientific and emotional support in conducting x-ray scattering experiments.

# Chapter 5

# Measurement and Modeling of Creep in Low-Salt Polyelectrolyte Complex Membranes

Mechanical properties are among the most important physical properties of free standing films as they define the deformation and fracture behavior of the material that are relevant for ensuring protection of the coated materials. The process of tuning the mechanical strength of complex coacervates have been characterized extensively using traditional mechanical tests and rheological techniques[113–116], but these traditional methods prove to be insufficient in the characterization of thin membranes as they often require large sample volume, or have restrictive geometric limits.

In this Chapter, free-standing polyelectrolyte complex membranes (PECMs) of the strong polyelectrolyte poly(styrene sulfonate) and poly(diallyl dimethyl ammonium) were fabricated for mechanical characterization. Stoichiometric PSS:PDADMA thin films were inflated with air into in aqueous media containing 0.0 to 0.3M NaCl using the biaxial membrane inflation apparatus discussed in Chapter 3 to measure the elastic modulus and creep compliance of the polyelectrolyte complex membranes. In addition, we apply a modified Fractional Maxwell Model (FMM) to describe the power-law relaxation and creep behavior observed in this low salt regime.

Special thanks to Kazi Sadman for helping with the preparation of the complex coacervate solutions and Dr. Bavand Keshavarz for helpful discussions on the fractional models. This work was performed under the following financial assistance award 70NANB14H012 from U.S. Department of Commerce, National Institute of Standards and Technology as part of the Center for Hierarchical Materials Design (CHiMaD).

## 5.1 Introduction

Polyelectrolytes are polymers that contain electrolyte groups within its repeating units. Notably, the charged groups in polyelectrolytes dissociate in aqueous solutions, giving rise to unique viscoelastic properties even at low polymer concentrations. The pervasiveness of polyelectrolytes extends to both nature and industry, and they can be commonly found as adhesives, thickeners, coatings, and flocculation agents due to their unique solution properties and biocompatibility[117–120]. While most industrially prevalent polymers are extensively used in non-aqueous media where electrostatic forces are not effective, these forces are fundamentally significant in nature and other biological applications. Therefore, understanding the behavior of charged polymers in these confined environments is crucial to engineering new materials that can operate in complex environments where multiple interactive species are present.

In this work, the mechanical properties of the strong polyelectrolytes poly(styrene sulfonate) (PSS) and poly(diallyl dimethyl ammonium) (PDADMA) were investigated. When oppositely charged polyelectrolytes are mixed together in the presence of salt, a phase separation phenomenon occurs. Ranging from liquid solutions to solid precipitates, the resulting products can have very diverse structures and properties depending on the conditions and methods of preparation[121–124].

Known as complex coacervation, this interaction forms polyelectrolyte complexes (PECs) that have numerous application impacts across fields such as food processing, cosmetics, and drug delivery, and may also help further our understanding of biological systems observed in marine organisms and extend it to human biology[120,125? –129]. The coacervation process can be controlled not only by the interaction species and preparation process, but also through external environmental parameters. From gels to particles, PECs with different morphologies and phase behaviors can be formed[120,121,130]. Most simplistically, oppositely charged

polyelectrolyte solutions can be mixed together to form coacervate-precipitates and phase-separated gels[116,121,131]. More complex behaviors can be achieved with the introduction of salts as counter ions. The broad range of transition regime between the liquid-like coacervate and solid-like precipitates have resulted in multitude of studies investigating the interaction mechanisms between key components that make up the complex coacervate: polyelectrolytes, water, and salts[118,123,124,128,132].

Some recent works have imparted significant progress in understanding the phase behavior and relaxation dynamics of polyelectrolyte coacervates, using time-temperature and time-salt superpositions to access a wider range of the frequency space otherwise untenable with linear viscoelastic measurements[123,124,132–134]. However, direct measurements of solid polyelectrolyte complex membranes in the low to no-salt regime ($<$0.5 M to 0.0 M) remain a challenge[121–124,135,136]. In the recent work by Ali and Prabhu[132], deviations from the scaling behavior in the low frequency regime for systems with decreasing salt concentrations highlight the current limitations of time-salt and time-temperature superposition in capturing the evolution of the complex relaxation dynamics in the precipitate-coacervate continuum of PECs.

In a different vein, fabrication of solid PEC films requires additional considerations when characterizing these polyelectrolytes. Methods such as spin-coating[137] and layer-by-layer assembly[138]? have been shown to produce PEC membranes (PECMs) with good film quality and thickness control, but they can be difficult to scale-up for industrial production. Electro-deposition[115] is a promising technique to expand the viability for scaling-up, but the substrates that can be used are limited to those that are conductive. In addition, typical film release methods that use a sacrificial layer not non-viable, since typical materials used such as poly(acrylic acid) or poly(styrene sulfonate) can contaminate the membrane. Here, a method to fashion free-standing PSS:PDADMA polyelectrolyte complex membranes (PECMs) without the use of sacrificial release layers is explored. Moreover, the biaxial mem-

brane inflation technique introduced in Chapter 3 is employed for the direct characterization of the mechanical properties of polyelectrolyte complexes at limiting salt concentrations (<0.5M NaCl).

## 5.2 Experimental Details

### 5.2.1 Materials

Poly(4-styrenesulfonic acid, sodium salt) (PSS, MM ca. 200k $g \cdot mol^{-1}$) and poly(diallyl dimethyl ammonium chloride) (pDADMAC, MM ca. 200k - 350k $g \cdot mol^{-1}$) were purchased from Sigma-Aldrich and used as received. Sodium chloride, potassium chloride, and potassium bromide were also purchased from Sigma-Aldrich. Sodium hydroxide used to make the film-release solution is from Fisher Scientific. All salt solutions were prepared using in-house deionized water. MilliQ water (18.2 MΩ) is used when forming coacervates.

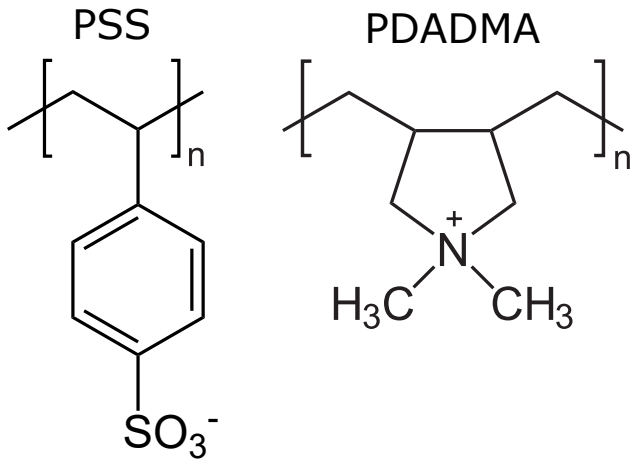


Figure 5.1: Chemical structure of poly(styrene sulfonate) (PSS) and poly(diallyldimethylammonium) (PDADMA).

### 5.2.2 Preparation of Polyelectrolyte Coacervate Complexes

Stoichiometric polyelectrolyte complexes were prepared following the methods detailed previously by Wang and Schlenoff[116]. Separate solutions of PSS (0.25 M) and PDADMA (0.25 M) were prepared and mixed together in a well-stirred beaker filled with deionized water at room temperature. The anionic and cationic polymers will complex in a 1:1 molar ratio and precipitate out as white solid. The precipitated PEC were then isolated using vacuum filtration and rinsed thoroughly with DI water until the conductivity of the supernatant fell below $50\mu S/cm$, at which point the PEC were collected and dried at 120°C for 12 hours.

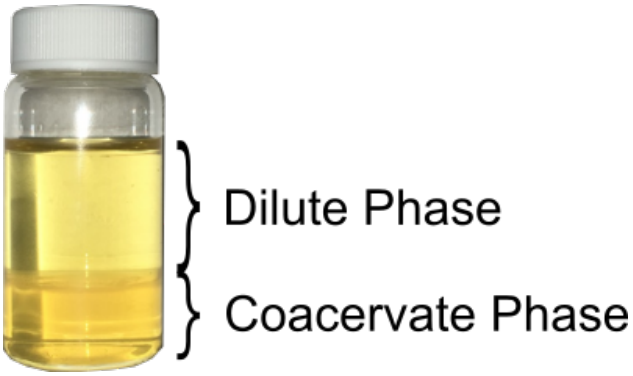


Figure 5.2: Phase separated solution of a PSS:PDADMA containing 3.03g of KBr.

Complex coacervates were then prepared by redissolving 1.50g of previously dehydrated PEC in 10 mL of 1.58 M KBr solution. Once the solid dissolves, an additional 5mL of water is added to reach a total of 15mL solution. The solution is then annealed at 60°C for 30 minutes on a stir plate. The polymer solution will phase separate into (a) a polymer-rich coacervate phase and (b) a polymer-poor dilute phase (Figure 5.2). This kinetically driven phase-separation process can achieve equilibrium after 7 to 10 days.

### 5.2.3 Fabricating Free-Standing PEC Membranes

Complex coacervate membranes were prepared by spin-coating the polymer-rich coacervate phase extracted from the solution. The substrate used here are aluminum plates cut from sheet stock and polished on a polishing wheel at increasing finer grits. A smooth, mirror-like finish is achieved by polishing using a 1$\mu$m polycrystalline diamond polishing solution. A smooth surface is needed to make pristine membranes. The extracted coacervate solution is spin-coated at 3000 rpm for 10 seconds and immediately transferred into a 0.5M KBr bath solution and annealed for 30 minutes. This process draws out the residual salt in the membrane, locking in the coacervate network structure in the form of a white, smooth membrane.

Next, to release the PEC membrane from the substrate, a highly basic (pH 13) NaOH solution is used. The basic solution dissolves away the polished aluminum substrate, forming aluminates and hydrogen gas. The released film is then rinsed repeatedly with DI water and transferred to a water bath until use. To verify the complexation polyelectrolyte coacervate membranes, and to ensure minimal contamination from the aluminates during release, the Fourier-transformed infrared (FTIR) spectra of the as-cast membrane and the post-anneal, post-release membrane are registered.

#### Fourier Transformed Infrared Spectroscopy (FT-IR)

FT-IR was performed with a Nexus 870 spectrometer (Thermo Nicolet) with a attenuated total reflection (ATR) module. Figure 5.3 shows the FTIR spectra of 1:1 (mole ratio) solution-precipitated complex membranes of PSS-PDADMA dried in air with and without annealing in a 0.5M KBr solution. The measured spectra is in good agreement with those reported in literature[139]? .

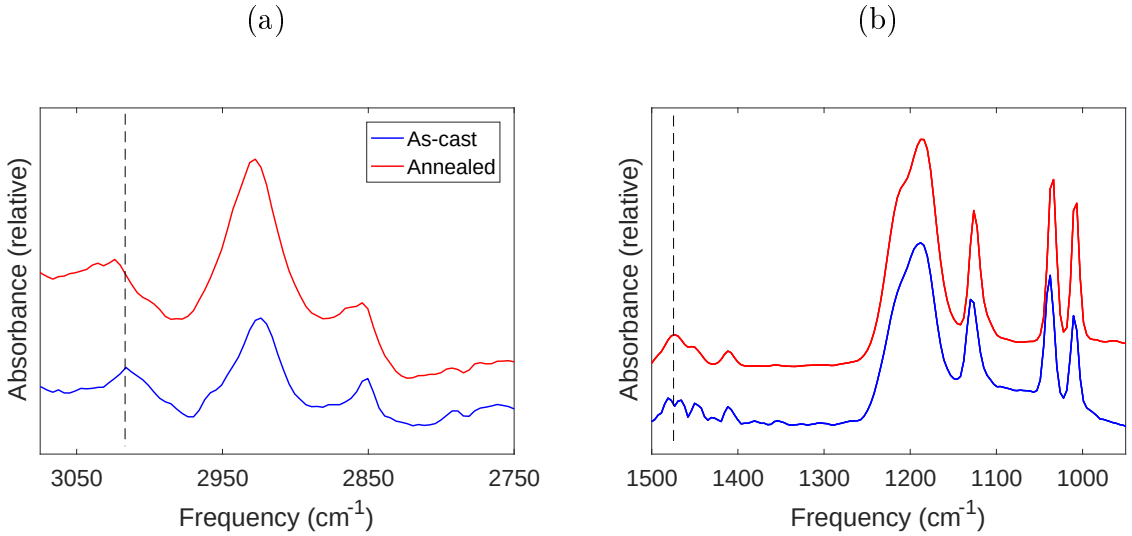


Figure 5.3: Attenuated total-reflection Fourier transform infrared (ATR-FTIR) spectra of PSS-PDADMA membranes as-cast (blue) and after annealing and release (red). (a) The C-H stretch region and (b) sulfonate region are shown.

The high frequency IR absorption region of the C–H stretch shows slight changes to the $-CH_3$ band (3016 $cm^{-1}$ to 3024 $cm^{-1}$). Since the membranes are to be used in hydrated conditions, and excessive drying results in very brittle films, those used for the ATR-FTIR experiments were only air dried. As a result, an appreciable quantity of adsorbed water remain within the membrane, and manifests in a broad absorption peak centered around 3500 $cm^{-1}$. The low frequency region (Figure 5.3b) highlights the absorption band produced by the sulfonates ($-SO_3^-$). Notably, the peak at 1473 $cm^{-1}$ (dash line), which is characteristic of the $-CH_3$ bending vibrations of PDADMAC, becomes more evident after annealing. The absence of additional peaks reveal that the PECMs are chemically identical before and after annealing, and rules out covalent interactions between the two materials as well as possible contamination from the film release step.

#### Membrane Thickness and Water Uptake

Thickness measurements are made using a high-resolution contact profilometer (Dektak 150, Veeco Instruments Inc.). A portion of the film is removed with a razor blade and transferred to a flat surface. Typical dry film thickness ranges between 5 to 8 $\mu m$ depending on spin conditions. In aqueous environments, PEC can be expected to swell considerably. After annealing, however, the structure of the network reduces the amount of water uptake. Film swelling measurements were made using a quartz-crystal microbalance (QCM) to determine the total mass uptake of the PEC films in solutions of varying salt concentrations. A 33% water uptake is observed in pure water, up to roughly 40 percent by weight for PSS-PDADMA membranes in low ionic strength (0.0M to 0.4M) NaCl solutions.

### 5.2.4 Biaxial Membrane Inflation

Details on the biaxial membrane inflation technique employed here can be found in Chapter 3. This testing configuration is advantageous for testing these polyelectrolyte complex films in aqueous environments. In particular, the hydration level can be maintained throughout the duration of the experiment, and unnecessary handling and excessive drying of the coacervate films can be avoided.

Briefly, a free floating PEC membrane is transferred onto an aluminum inflation tube ($d = 12\,mm$) and clamped in place with an aluminum cap (Figure 5.4). The capped membrane was submerged in aqueous solutions with 0 to 0.3M NaCl at room temperature and conditioned for at least 10 minutes prior to each measurement. No evidence of flow is observed in our experiments prior to loading.

The membrane is infused with air (RH 100%) into the aqueous bath at a constant rate of 0.1 mL/min to achieve a target stress of 0.2 MPa. Stress increases linearly during initial loading, and it takes about 5 minutes during each experiment to reach the target threshold.

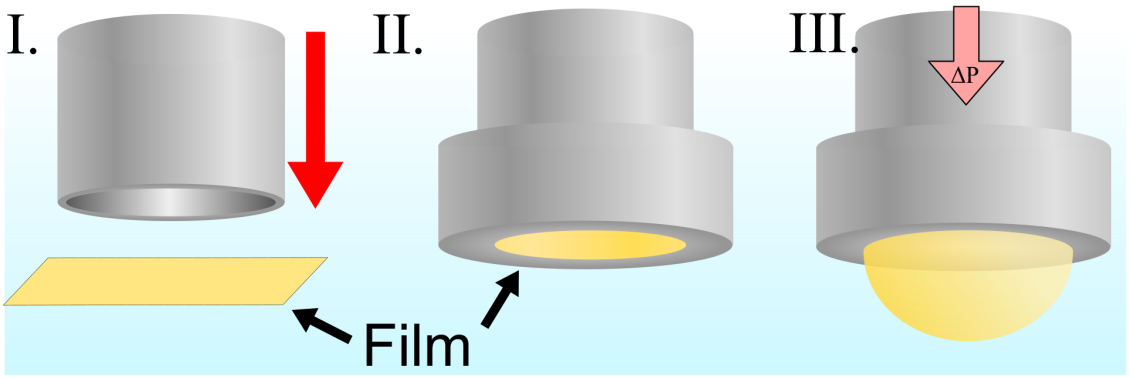


Figure 5.4: Schematic of the biaxial inflation tube showing the (i) transfer, (ii) clamping, and (iii) inflation of a thin film.

### 5.2.5 Fractional Maxwell Model

The Fractional Maxwell Model has been previously reported[124,140,141] to accurately describe the relaxation behavior of a wide range of complex rheological fluids such as the system presented here. In this work, we attempt to describe the biaxial deformation behavior of the solid PEC complex membranes more succinctly than traditional models using the framework set by this constitutive theory. Indeed, linear viscoelastic Maxwell model can describe the relaxation characteristics of these complex power-law materials by introducing additional springs or dash-pot elements. However, this approach is impractical from a modeling perspective, as a very large number of elements may be necessary to recapture the observed relaxation behaviors. An advantage of the FMM is the ability to describe the complex power-law behavior succinctly without the need to employ a large quantity of elements.

As an extension of the traditional linear viscoelastic Maxwell model in which an arrangement of elastic Hookean springs and viscous Newtonian dash-pots are used, the fractional Maxwell model utilizes a conceptual "spring-pot" element, denoted with subscript "sp", to describe material responses intermediate between those of the classical elements. The spring-pot is a numerical representation of the observed power-law behavior and lacks a precise physical representation like the spring or dash-pot. The constitutive equation for the spring-

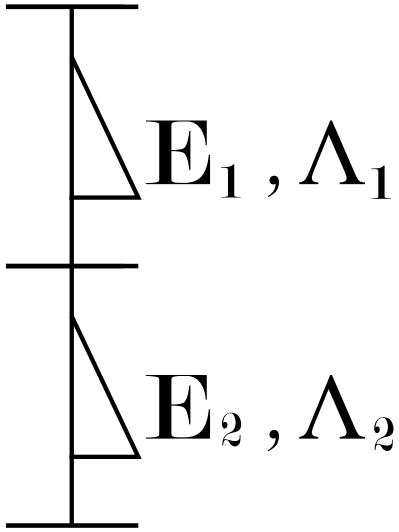


Figure 5.5: A schematic of the Fractional Maxwell model consisting of two spring-pots in series as described by Jaishankar and McKinley[140].

pot is represented as:

$$\sigma(t) = E_{sp}\frac{d^{\Lambda}\varepsilon}{dt^{\Lambda}} \tag{5.1}$$

The properties of the spring-pot element are quantified by two independent parameters, $\Lambda$ and $E_{sp}$, where $\Lambda$ is the fractional power law exponent, and $E_{sp}$ is the magnitude of the modulus with units of $Pa\,s^{\Lambda}$. The units of Pa with a fractional power of time may be rather non-intuitive, but by setting a reference time, $t_{ref}$, corresponding values of the magnitude of the modulus with units of $Pa$ can be recovered. The complete Fractional Maxwell Model is presented in Jaishankar and McKinley[140] as two spring-pot elements in series. The FMM can recover the traditional Maxwell model in the limiting cases of $\Lambda_1 = 0$ and $\Lambda_2 = 1$, with which the spring-pot elements reduces to a Hookean spring and a Newtonian dash-pot, respectively.

## 5.3 Results and Discussion

### 5.3.1 Biaxial Deformation

Figure 5.6 shows the stress and strain vs. time curves of a film tested under a cyclic protocol.

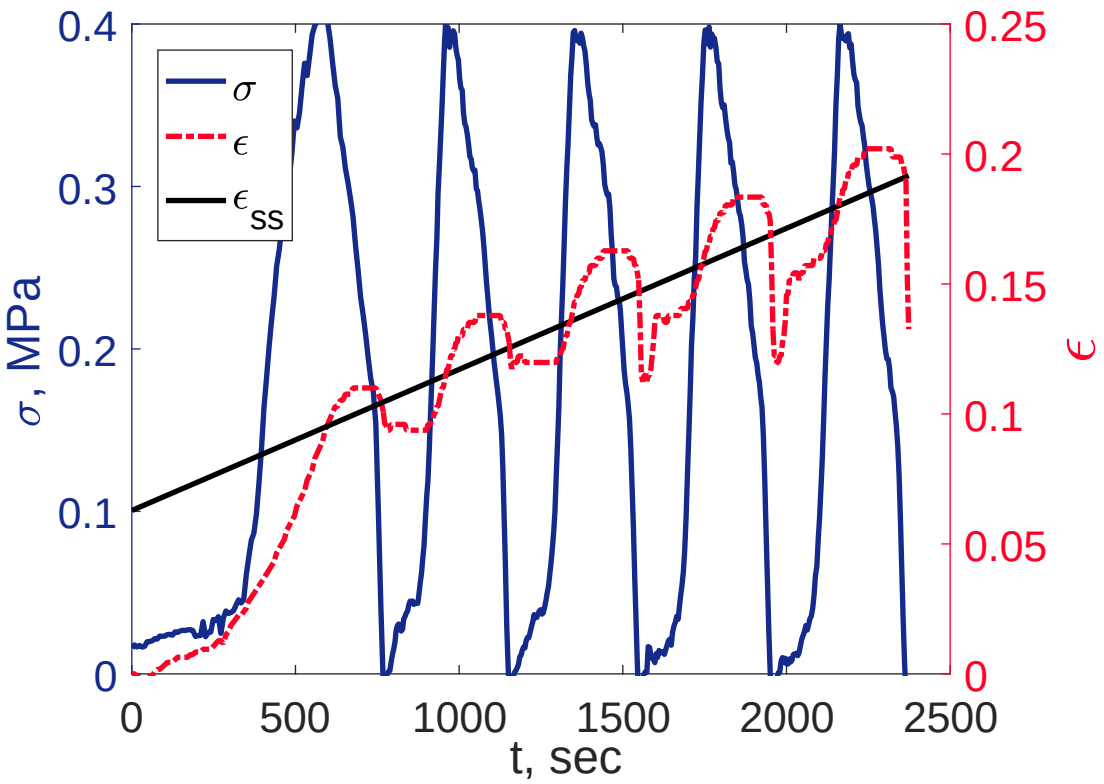


Figure 5.6: (a) Stress and strain vs. time for a PECM tested for 5 consecutive cycles. The black line indicates the fit for a steady-state creep that results from a positive stress applied during the experiment.

The membrane is injected with air at a constant rate of 0.05 mL/min until a target stress of 0.4 MPa at the apex is achieved. Strain at the apex is corrected to the initial membrane position recorded just before the start of the experiment. Due to the osmotic pressure across the interface of the membrane, small stresses are measured at the apex at the start of the test. After the target is reached, air is withdrawn at the same rate until a lower threshold of

0.01 MPa. Significant deformation is observed upon loading the first cycle with over 10% of the applied strain being permanent. During unloading, 2 to 3% elastic recovery is observed.

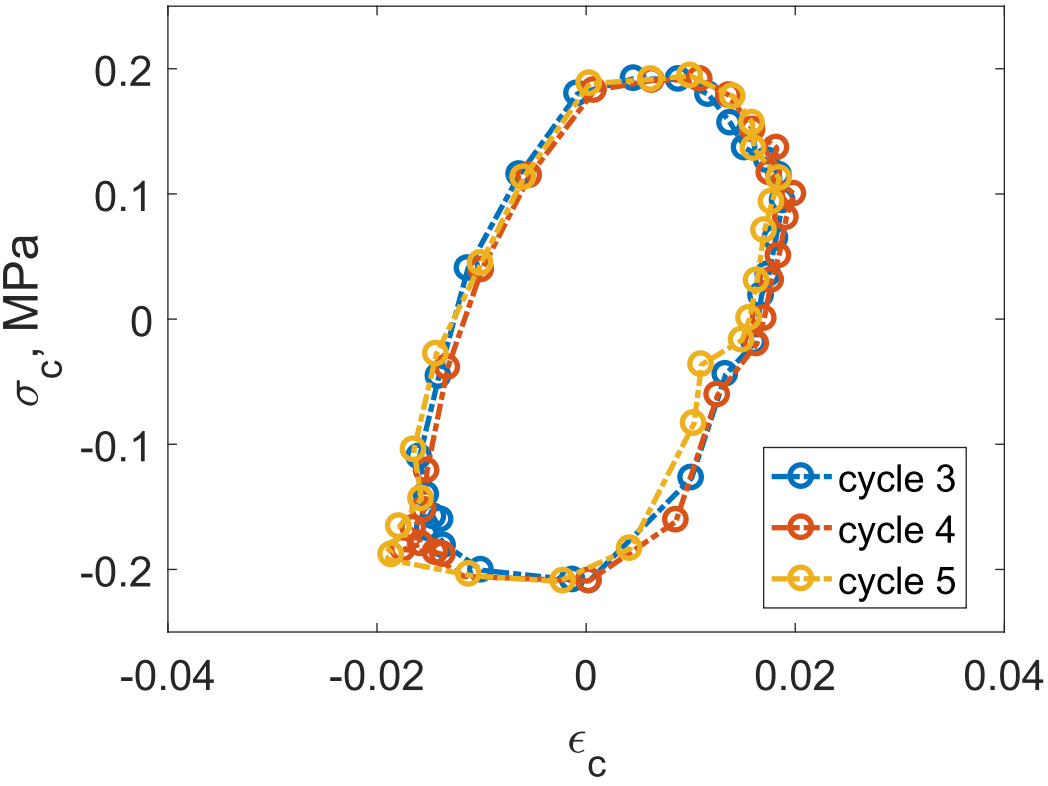


Figure 5.7: Cyclic stress-strain response of the membrane without the linear creep contribution.

The biaxial modulus, which is twice the Elastic modulus for incompressible materials, is calculated to be around 7.7 MPa by taking the slope at low strain in the linear, elastic region of the first cycle. In subsequent cycles, the positive stress in the inflation experiment results in steady-state creep, $\epsilon_{ss}$, and contributes to the unrecoverable deformation incurred. By subtracting an average stress from the total stress of the experiment, ($\sigma_c = \sigma - \sigma_{avg}$), a cyclic stress can be calculated. Similarly, the steady-state creep contribution can be subtracted from the total strain ($\epsilon_c = \epsilon - \epsilon_{ss}$) to isolate the response to the cyclic loading. Figure 5.7 shows this corrected cyclic stress-strain behavior. Although the stresses and strains are not

purely sinusoidal in this experiment, an effective phase angle, $\phi_{\text{eff}}$, can be obtained from the following expressions[32]:

$$\epsilon_c = \epsilon_0 cos(\omega t) \tag{5.2}$$

$$\sigma_c = \sigma_0 cos(\omega t + \phi) \tag{5.3}$$

$$\sin \phi_{eff} = \frac{\oint \sigma d\epsilon}{\pi \sigma_0 \epsilon_0} \tag{5.4}$$

Here $\sigma_0$ and $\epsilon_0$ are the relative magnitudes of stress and strain in a cyclic experiment. The phase shift between the stress-strain response for a PSS:PDADMA membrane in pure water is found to be $\phi_{\text{eff}} = 7.7° \pm 3.2°$. The result reveals that the material behaves mostly elastically, despite a significant water swelling.

### 5.3.2 Modulus and Creep Compliance

As film dehydration drives the formation of ion pairs, it is expected that the association of PSS-/PDADMA+ would be stronger in environments with lower salt concentrations and weaker in those with higher salt concentrations. Therefore, a higher maximum strain can be expected for a PEC membrane in an aqueous salt solution at any given stress. Knowing this, a constant stress experiment is designed to observe the creep behavior of the material in the presence of salt. The geometric constraint of the test requires additional ramping time to achieve the specified target stress, since we cannot apply an instantaneous load. To avoid high ramping time at the beginning of the test, a target stress of 0.2 MPa is set.

Figure 5.8 shows the behavior for PECM membranes under a constant stress protocol. The corresponding strain ($\epsilon^*$) and time ($t^*$) at which the target stress is reached are marked

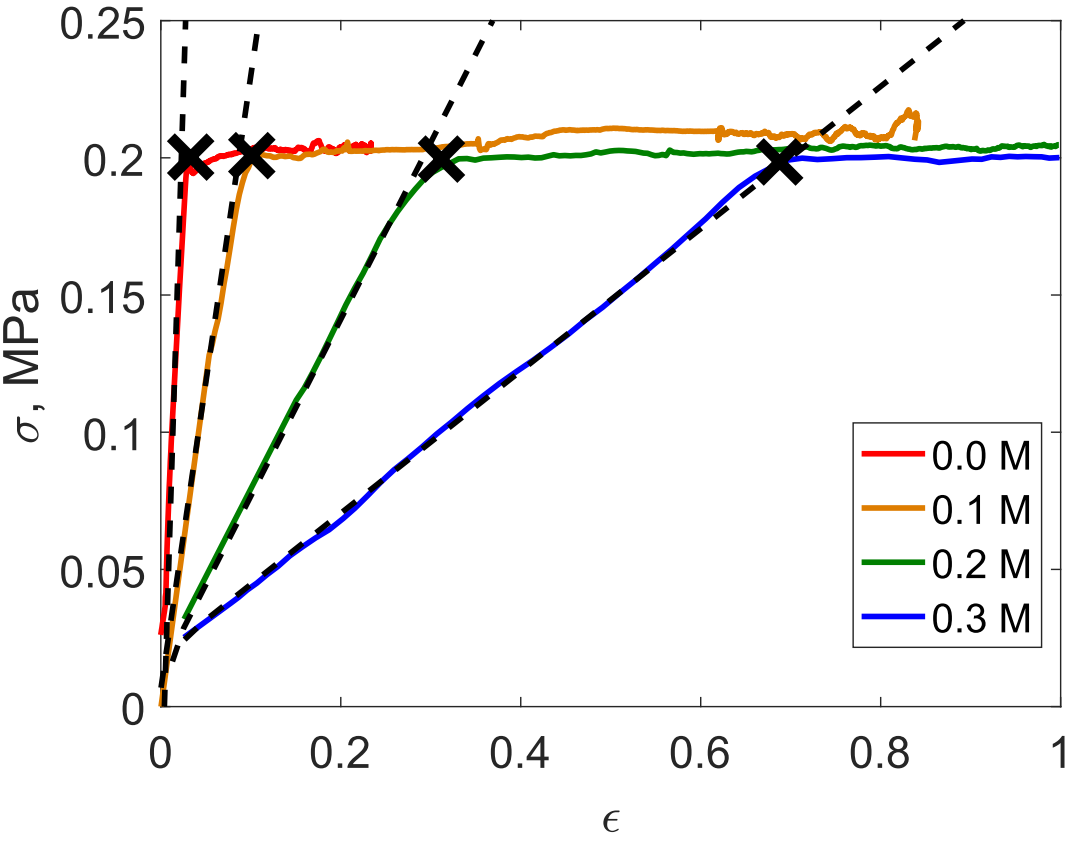


Figure 5.8: Stress-strain behavior of PECMs inflated with air under a constant stress protocol. Black X's denote the point at which a target stress of 2 MPa is achieved.

with black X's in Figures 5.8 and 5.9. As expected, the addition of salt plasticizes the PEC membranes, resulting in greater deformation at the given stress. Although the chain mobility within the network is severely limited due to the annealing process required to fabricate free-standing films, the presence of salts can promote swelling within the network and softens the material. Salts can also promote the re-association of broken charge pairs within the network, which allows for greater deformation without membrane fracture or failure. On the other hand, further increasing the salt concentration detrimentally weakens the charge association, which leads to the transformation of the precipitates into a gel or solution. Due

to the linearity of the strain response, an effective modulus, $E^*$, can be evaluated. Values of $\epsilon^*$, $t^*$, and $E^*$ are summarized in Table 5.1 below.

| Salt conc. (M) | $\epsilon^*$ | $t^*$ (sec) | $E^*$ (MPa) |
|---|---|---|---|
| 0.0 (cyclic) | – | – | 7.7 ± 0.5 |
| 0.0 | 0.04 | 94 | 7.2 ± 0.7 |
| 0.1 | 0.10 | 198 | 2.3 ± 0.4 |
| 0.2 | 0.38 | 246 | 0.6 ± <0.1 |
| 0.3 | 0.69 | 260 | 0.3 ± <0.1 |

Table 5.1: $E^*$, $\epsilon^*$, and $t^*$ as a function of NaCl concentration.

Membrane compliance was found to increase with increasing concentration of sodium chloride. At concentrations above 0.3 M, membrane leakage and failure are observed prior to loading. The average area strain as a functional of time is captured for constant stress creep experiments (Figure 5.9). The initial loading region is represented in gray, with black markers showing when the target stresses are achieved. Stills from the captured video are shown to highlight the profile of the inflated membrane at various strains for the 0.3M NaCl case.

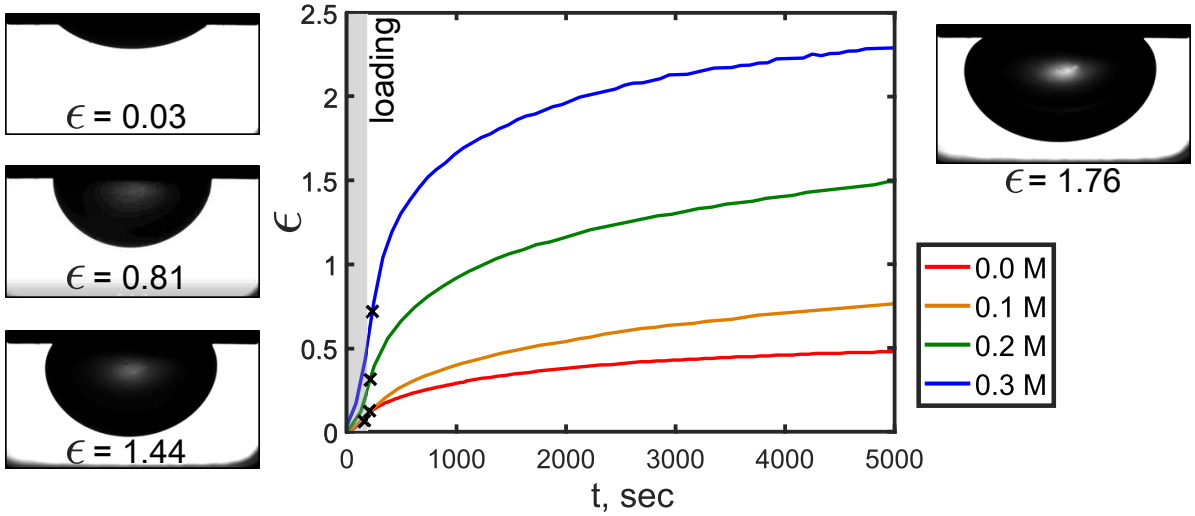


Figure 5.9: Apex strain of PSS-PDADMA membranes inflated in 0 to 0.3M NaCl solutions for 80 minutes. Gray region highlights initial loading of the membranes.

Significant membrane deformation is observed even after the target stress is reached. Steady state creep is achieved when the strain rate stabilizes and yields a constant value. During this time, the charge associations within the PEC network are breaking and reforming to maintain the overall integrity of the film. The results here exhibits a power-law behavior similar to those observed in polyelectrolyte complex fluids and gels[114,123,124,141].

### 5.3.3 Modified Fractional Solid Model

The fractional Maxwell model (FMM) was previously introduced to describe the power-law behavior observed in these rheologically complex materials. In this work, we set $\Lambda_1 = 0$ to recover the Hookean spring, and to reflect the solid nature of the PEC membranes at the low salt regime. This modified fractional Maxwell model with a spring and a spring-pot in series is defined as the modified fractional solid model (Figure 5.10).

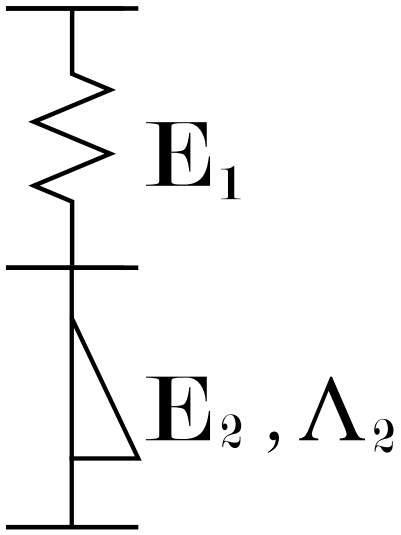


Figure 5.10: Fractional solid model consisting of a Hookean spring and a spring-pot in series. In the limiting case of $\Lambda_1 = 0$, the first spring-pot element reduces to a Hookean spring.

By taking the LaPlace transform of the constitutive differential equation, the creep compliance, or the measured strain divided by the applied stress, can be described with the following expression:

$$D(t) = \epsilon(t)/\sigma_{ss} = \frac{1}{E_1} + \frac{1}{E_2}\frac{\left(\frac{t}{t_{ref}}\right)^{\Lambda_2}}{\Gamma(1+\Lambda_2)} \tag{5.5}$$

where $\Gamma$ is the gamma function, and $\Lambda_i$ is the fractional exponent of power-law, $E_1$ is the modulus of the spring element calculated previously, and $E_2$ the modulus of the spring-pot element. Figure 5.11 shows the creep compliance of PSS:PDADMA membranes at each salt concentration with fits from the fractional solid model. A reference time of 3,000 sec is defined to fit the steady-state compliance of the material. The model fits the long term creep of the membranes well, although the short term behavior during initial loading was not captured.

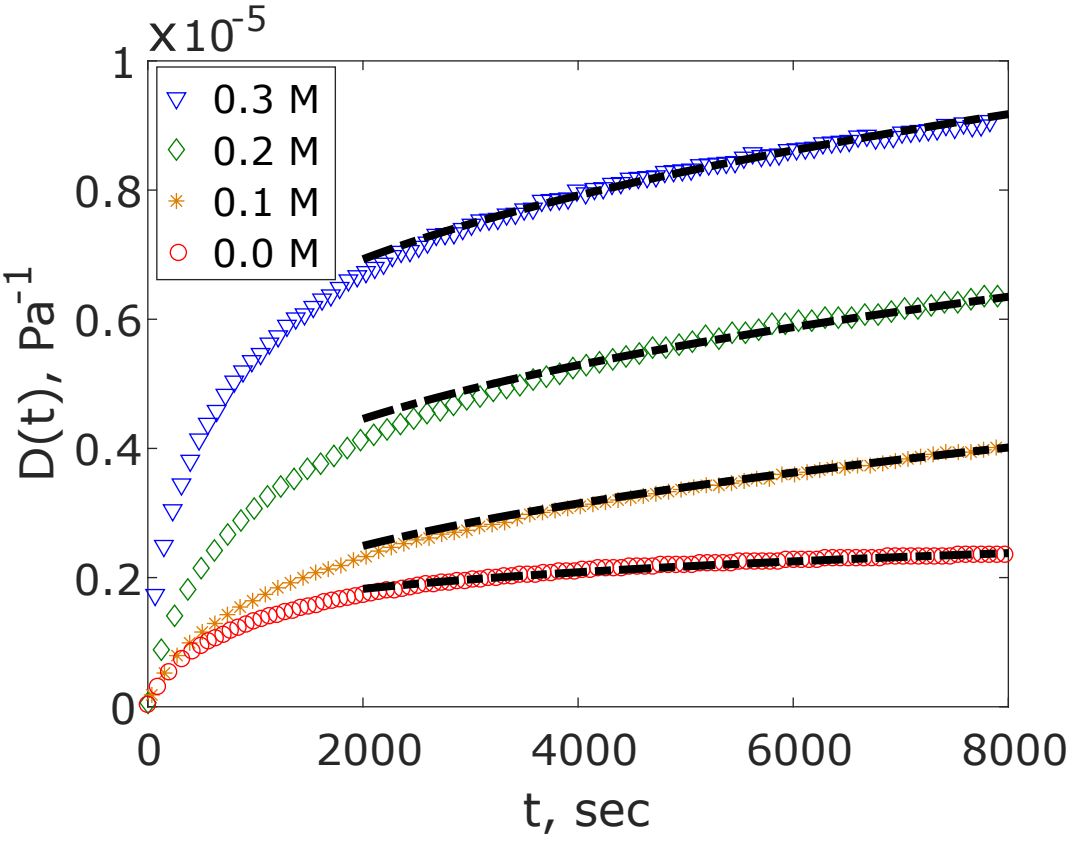


Figure 5.11: Creep compliance of PSS-PDADMA membranes fitted using the fractional solid model in black dash lines. the FSM fits the long-term creep of the material well, although the short-time behavior during membrane loading is not capture.

Since the membrane loading was non-instantaneous, the model, which assumes a step-strain, cannot properly capture our observed behavior. Despite the simplicity of our model, the creep behavior of the PEC network is nevertheless recaptured at long times. Results of the fractional solid model fit are summarized in Table 5.2.

| Salt conc. (M) | $\Lambda_1$ | $E_1$(MPa) | $\Lambda_2$ | $E_2$ (MPa) |
|---|---|---|---|---|
| 0.0 | 0.0 | 7.2 | 0.20 | 0.47 |
| 0.1 | 0.0 | 2.3 | 0.35 | 0.29 |
| 0.2 | 0.0 | 0.6 | 0.35 | 0.22 |
| 0.3 | 0.0 | 0.3 | 0.35 | 0.17 |

Table 5.2: Values of the fractional solid model fitting parameters $E_1$ and $E_2$ with a reference time of 3,000s.

The elastic modulus of the PECMs decreases with increasing charge concentration in the testing media. Salt ions screens the charge-pair interaction within the PEC network and effectively removes the total number of charge association sites contributing to the overall membrane integrity. The membrane swells further as each ion carries multiple water molecules within its hydration shell. Values of $E_1$ reveal that this pseudo-modulus related to the viscoelastic response of the polyelectrolyte network to an applied load decreases with modulus.

Interestingly, the fractional power $\Lambda_2$ reveal that a secondary relaxation with a more liquid-like response can be associated with the presence of salt, suggesting that at longer times the deformation is dominated by complex relaxation described by the spring-pot element with properties defined by $E_2$ and $\Lambda_2$. These finding suggest that the spring-pot element, with a mathematical treatment based in fractional calculus, can be a useful tool for modeling complex rheological behavior in materials with power-law relaxation, as well as systems associated with network viscoelasticity at the low-salt regime.

## 5.4 Conclusion

This chapter demonstrated that a biaxial inflation technique can be a useful tool in studying the deformation and creep behaviors of PECMs in an hydrated environment in order to fully appreciate the complex effects of the interconnected components within this interpenetrating polymer network swollen with water and filled with charge.

The reported modulus and compliance of PECMs at the low-salt regime is highly relevant to the fields of filtration, bio-coatings, and drug delivery in which the immediate response and long-term stability of the system to external stimuli such as hydration level, charge density, and applied stress, which can all have significant impact on material performance. The creep compliance is found to have a linear dependence on salt concentration, which can be attributed to an increase in the bound water brought into the film by the salt ions. The fractional solid model provides a simple method to describe the power-law creep behavior of polyelectrolyte complex membranes at these low-salt conditions.

# Chapter 6

# Quantifying the Mechanical Properties of Polycarbonate Thin Films Using Wrinkles and Cracks

In this chapter, the mechanical properties and fracture behavior of polycarbonate thin films as tough coatings on a supported geometry are investigated. A combined wrinkling–cracking (WC) methodology is employed to characterize the elastic and fracture properties of a stiff film deposited onto a polydimethyl siloxane (PDMS) substrate. This work aims to better understand key mechanical properties such as stiffness, strength, and ductility to provide design guidelines for mechanically strong and fracture-resistant engineering materials. Taking advantage of the elastic mismatch between a rigid coating and a soft substrate, this technique captures the mechanical properties of ultra-thin ($< 200$ nm) films that are difficult to measure accurately using traditional tensile tests. Here, the mechanical properties of polycarbonate (PC) thin films are characterized as a function of film thickness.

Special thanks to Dr. Edwin Chan and Dr. Christopher Stafford from the Material Measurement Laboratory at the National Institute of Standards and Technology (NIST) for their expertise on the wrinkling and cracking setup.

## 6.1 Introduction

Supported structures in the form of a hard coating layer on a compliant substrate is becoming more prevalent in the field of flexible electronics[?] , wearable devices[142], and protective coatings[143]. For these applications, film or substrate deformation in and out of the plane are expected, and interlayer delamination and environmentally assisted crack formation can be detrimental for device operation. With the miniaturization of technology, accurate and reli-

able mechanical testing of materials at the nanoscale becomes a primary challenge. Additionally, the mechanical behavior of nanoscale materials has been shown to differ from those in the bulk[144]. To further engineer materials that are mechanically strong and fracture-resistant at these ever-shrinking dimensions, direct knowledge of the key mechanical properties such as stiffness, strength, and ductility is a necessity.

Volynskii et al.[145,146] devised a combined wrinkling–cracking (WC) technique to characterize the fracture behavior and mechanical properties of Pt thin films deposited on a rubber substrate. When subjected to uniaxial tension, the layered structures will form parallel channel crack in the direction of the applied strain. Independent of these crack formation events, periodic surface instabilities in the form of wrinkles will appear in the direction perpendicular to the direction of the applied strain.

Stafford and coworkers[97] applied the technique to characterize polymeric thin films. They show the critical strain for crack initiation can be predicted by extrapolation of the crack density at varying strains. Interestingly, through the surface wrinkling wavelength they found the stiffness of the polymer decreases substantially below a critical film thickness of 40 nm, which further highlights our limited understanding of how material properties are affected by the transition from the bulk to nanoscale. The WC technique not only enables accurate measurement of the mechanical properties, but also reasonable prediction of the brittle fracture behavior of polymeric thin films.

## 6.2 Background

### 6.2.1 Brittle Fracture

Previous work employing this technique have primarily focused on understanding brittle fracture in materials such as metal thin films and glassy polymers that undergo brittle fracture with negligible plastic yielding. Taking advantage of the elastic mismatch between

a rigid coating and a soft substrate, this technique can capture the mechanical properties of ultra-thin films that are difficult to measure accurately using traditional methods. From these brittle materials, it follows that the average fragment width is inversely proportional to the applied strain, and maximum tensile stress occurs at the center between adjacent cracks. For a given film with a thickness $h_f$, the average crack spacing, $\langle d \rangle$, as a function of applied strain after the onset of cracking, $\overline{\varepsilon}$ $(= \varepsilon - \varepsilon^*)$, is given by:

$$\langle d \rangle = \frac{2h_f \sigma^*}{E_s \overline{\varepsilon}} \tag{6.1}$$

Where $\sigma^*$ is the fracture strength of the film, and $E_s$ is the elastic modulus of the substrate. By rearranging the equation to the form $\sigma^* \propto \langle d \rangle \, \overline{\varepsilon}$, a direct estimate of the fracture strength can be made:

$$\sigma^* = \frac{E_s \overline{\varepsilon}}{2h_f \rho_c} \tag{6.2}$$

Where $\rho_c (= \frac{1}{\langle d \rangle})$ is the crack density of the film.

### 6.2.2 Buckling Instabilities

Due to the Poisson effect, when a material is stretched uniaxially, the material also experiences a compressive strain in the transverse direction. The elastic mismatch between the film and the substrate drives the system to minimize the strain energy through buckling instabilities. The buckling instabilities grow parallel to the direction of applied strain, and can occur in the form of surface wrinkles or film delamination. The exact mode of energy dissipation is dependent on the ratio of the elastic moduli of the film and substrate, and is used to determine the critical strain to the onset of surface wrinkling:

$$\varepsilon_w^* = \frac{1}{4}\left(\frac{3\overline{E_s}}{\overline{E_f}}\right)^{2/3} \tag{6.3}$$

Wrinkling is the preferred instability mode when the film can be easily bent and is well-adhered to a soft substrate. Alternatively, delamination will occur when the work required to bend the film becomes greater than the energy released during delamination. This happens when the substrate modulus is closer to the film modulus, or the film is too thick to bend. The critical value of the strain for delamination can be calculated using the following relationship:

$$\varepsilon_d^* = \frac{\pi^2}{12}\left(\frac{2h_f}{L}\right)^2 \tag{6.4}$$

Where L is a delamination width along which the film is not adhered to the substrate. Mei el al.[147] presented a bucking mode selection map by plotting these two expressions of critical strain to the onset of surface wrinkling and delamination, and this map predicts whether the preferred buckling mode for a given film is surface wrinkling or film delamination.

This is caused by the Poisson's effect and the elastic mismatch between the film and substrate. The wavelength of these wrinkles, $\lambda$, could effectively estimate the elastic modulus of the film material, given by:

$$\lambda = 2\pi h_f \left(\frac{\overline{E_f}}{3\overline{E_s}}\right)^{1/3} \tag{6.5}$$

where $h_f$ is the film thickness, and $\overline{E_f}$ and $\overline{E_s}$ are the plane-strain modulus of the film and substrate, respectively.

### 6.2.3 Ductile Fracture

Although brittle fracture has been studied extensively, the investigation of the mechanisms behind ductile fracture of polymers is still in its infancy. Ductility is observed in materials

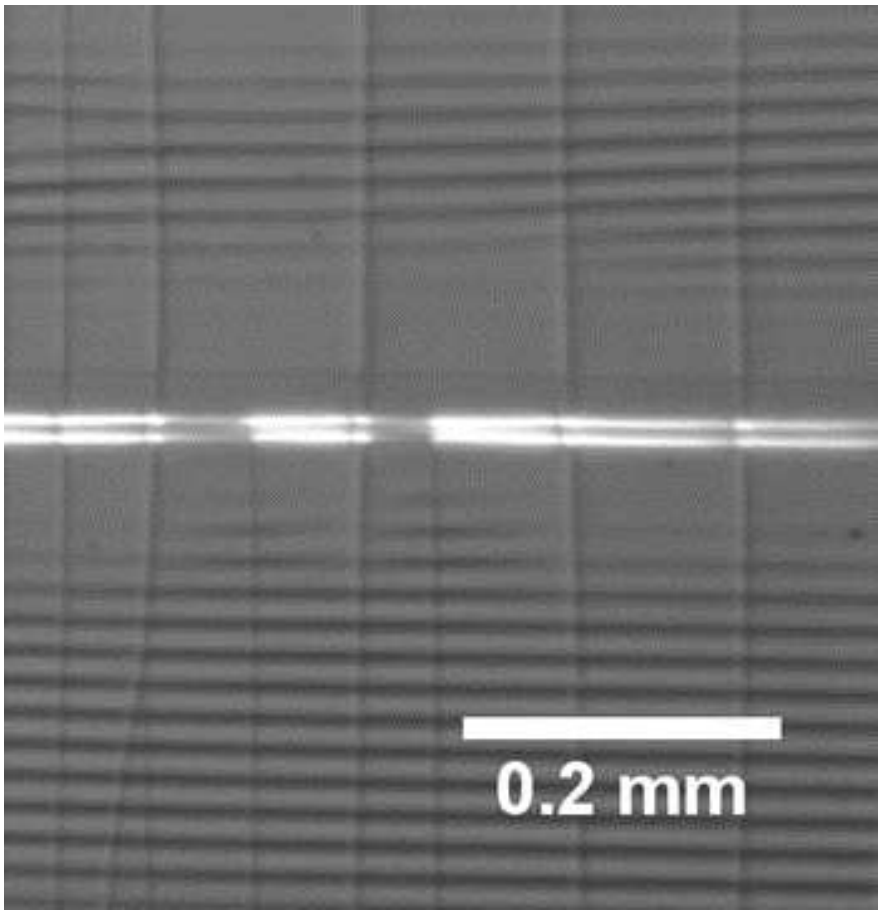


Figure 6.1: An optical micrograph of a 250 nm polystyrene film deposited on a compliance substrate. Vertical channel cracks accompanied by horizontal wrinkles in the film. Film delamination can be seen running across horizontally in the center of the image.

that undergo large, permanent deformation under an applied tensile load, and typically uniaxial tensile test and indentation tests are used. However, these traditional mechanical tests often require large samples or specific geometries, and may not be suitable for studying thin films or supported structures. In addition, current methodology in characterizing the mechanical properties of polymers attempts to capture the materials properties in terms of a "toughness" measurement, yet differentiating a stiff material from a stretchy material with similar toughness values remains a challenge.

Ductile fracture can be differentiated into two pathways: (a) Plastic deformation, or yielding, of the polymer chains, which could lead to strain hardening or strain softening, and (b) through the formation of fracture surfaces. Typical ductile material undergo crack blunting events, in which the crack tip with the highest stresses will extend out beyond the crack tip, yielding in the process and reducing the overall stress field. These fracture events do not always end in catastrophic failure like brittle fracture, as the extended stress field dissipates the strain energy in a larger region to prevent critical stress buildup at the crack tip. These properties make ductile polymers extremely desirable for applications in coatings and impact mitigation.

In this study, the mechanical properties and fracture behavior of polycarbonate, a highly durable commercially prevalent engineering polymer, are characterized as a function of film thickness. Figure 6.2[148] shows that upon loading, polycarbonate samples will reach a critical stress value, at which the material will begin necking. The neck will grow and extend across the entire sample, at which point the material will fail by fracture. The focus is to develop the WC methodology as a technique to directly characterize the mechanical properties of ductile polymers.

The wrinkling phenomenon can be exploited to characterize the modulus of a material that has undergone a yielding event. Due the yielding of the material, surface wrinkling and fracture become dependent variables. As a result, the analysis of the wrinkling wavelength enables the characterization of a deformed material. The mechanical properties of rigid films on compliant substrates are of practical interest for applications such as stretchable electronic and organic photovoltaics. In these applications, device failure is often caused by interlayer delamination or stable crack formation that lead to circuit shorting instead of mechanical failure of the system. The prescribed testing geometry allows for the characterization of desirable mechanical properties that are pertinent in these applications, and provides a testing environment that is appropriate for the targeted use for these devices.

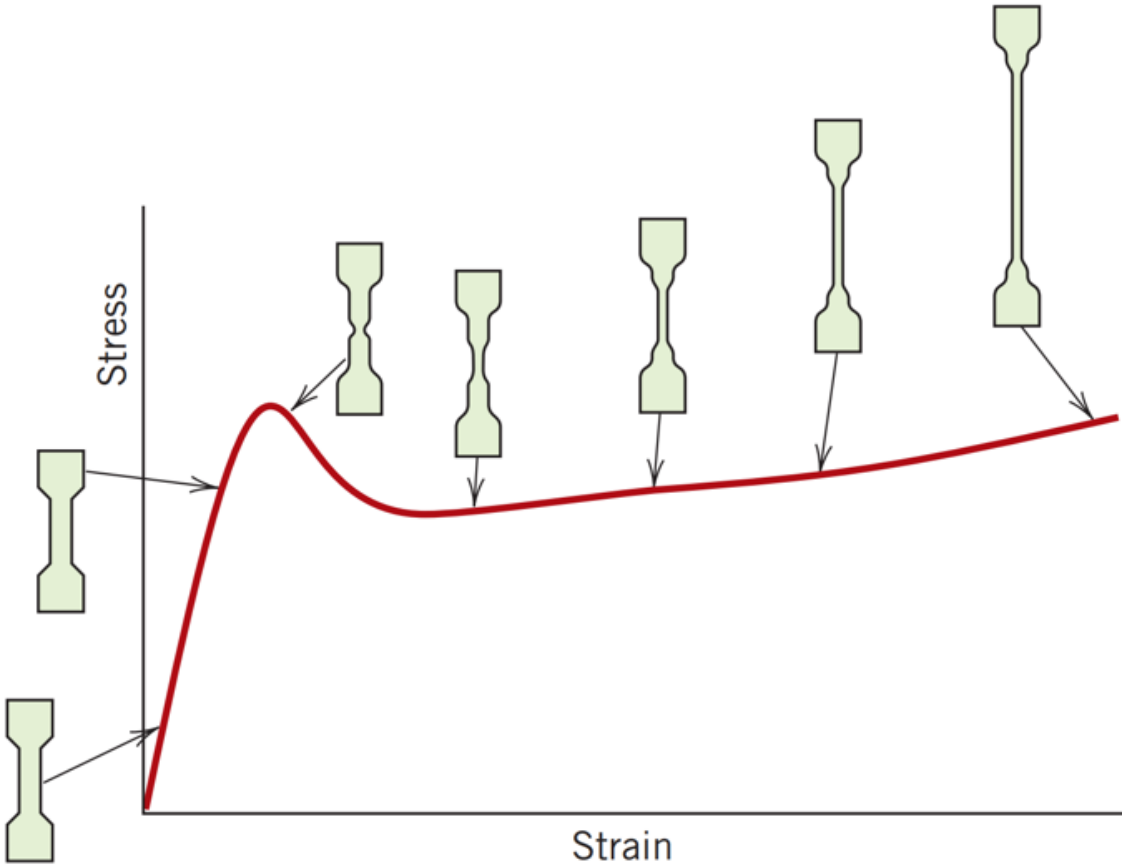


Figure 6.2: Typical stress-strain behavior for a polycarbonate tensile sample.[148]

## 6.3 Experimental Details

### 6.3.1 Materials

Polycarbonate (Lexan 130-111, $M_w$ = 36,500 g/mol) was obtained from GE and used as received. Sylgard 184 silicone elastomer kit is purchased from Dow-corning. Cyclohenanone is purchased from Sigma-Aldrich and used as received.

### 6.3.2 Substrate Preparation

Poly(dimethylsiloxane) (PDMS) substrates were prepared by mixing the elastomer base to crosslinker in a 15:1 mixing ratio. Once mixed, the mixture was degassed in a desiccator

under vacuum for 20 min and subsequently poured into a Petridish mold to cure in air for at least 48 h. Substrate thicknesses were measured using a Mitutoyo digital height gauge. Typical thickness range from 1 mm to 2 mm. The cured PDMS is subsequently cut into 6 cm by 1.5 cm slabs. A custom tensile stage is used to determine the elastic modulus for each batch of PDMS and confirmed with a JKR indentation test.

### 6.3.3 Film and Sample Preparation

Solutions of polycarbonate were prepared by dissolving 1 to 3 wt% of polymer in cyclohexanone and allowed to stir over heat (T = 70°C) for 4 days. All solutions were filtered with 0.45 $\mu$m syringe filters prior to spin coating. UV-O cleaned Si wafers were flooded with polymer solution and spin coated at various speeds for 30 s with a 1 s ramp time. Films thicknesses were measured using a Filmetrics reflectometer, and averaged over six arbitrary positions on each sample. Triplicates were made to determine the spin-coating conditions necessary to produce uniform, smooth films of the desired thickness. Average film thicknesses at the various spin speeds are summarized below (Figure 6.3). In this work, film thicknesses below 200nm were chosen to limit possible film delamination during testing. Spin-coated films are kept in a vacuum chamber prior to use.

During sample preparation, a slab of PDMS is first clamped onto a custom tensile stage to avoid pre-straining the PC sample through excessive handling. A small initial strain is applied to the slab of PDMS to ensure there is no slack on the substrate. This gauge value is set as the initial, non-deformed value.

For film transfer, a spin-coated PC film is brought into intimate contact with the clamped PDMS. Once the film and the substrate are in intimate contact, the clamping stage is submerged into a DI water bath to release the adhered film from the Si substrate. Excess water is removed with compressed air.

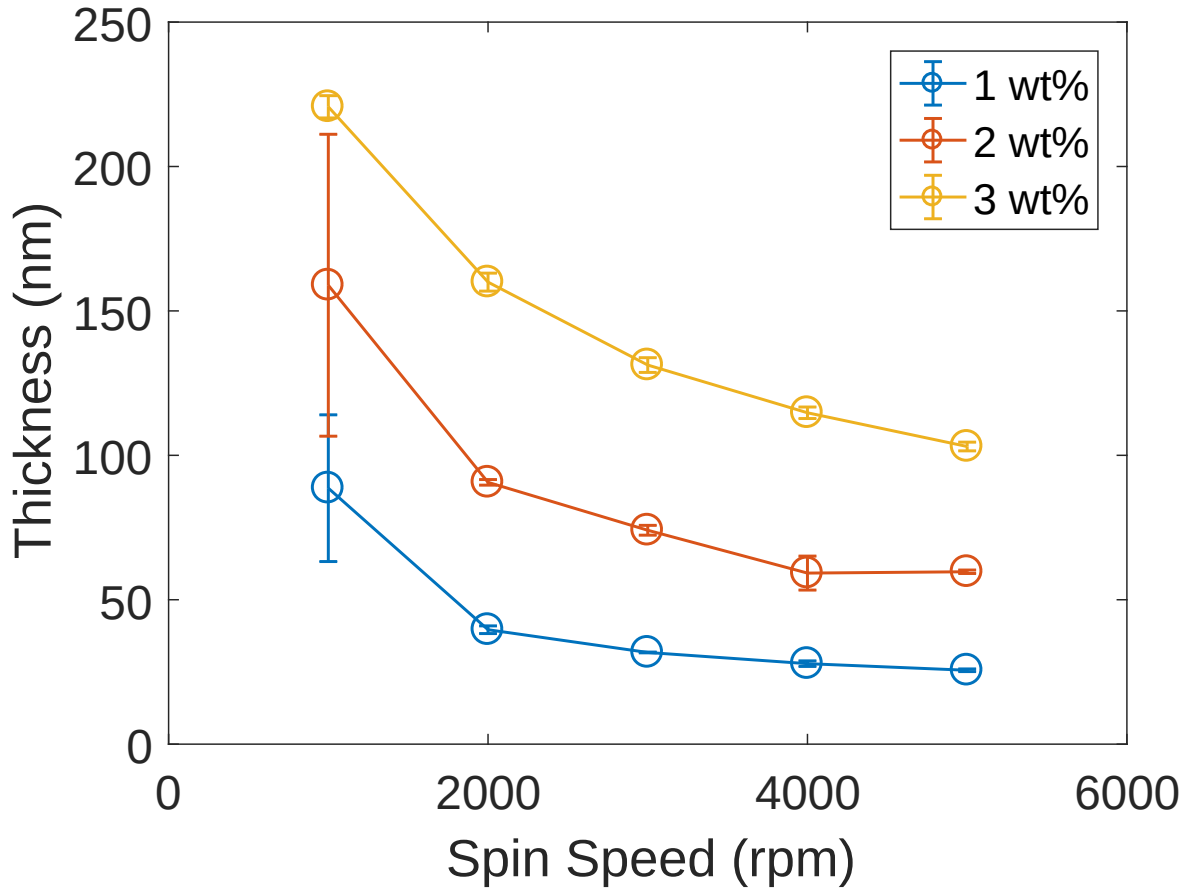


Figure 6.3: PC film thicknesses as a function of solution concentration and spin speeds. PC films are cast from 1 to 3 wt% polymer solutions in cyclohexanone. At low speeds (<1000rpm), film thicknesses vary greatly due to uneven drying.

### 6.3.4 Image Analysis

The affixed specimen is deformed at a rate of 0.5 % strain per second. Continuous load-displacement measurements were recorded until a predetermined displacement was achieved. Film deformation and fracture were captured using a Nikon Z730 optical microscope outfitted with a CCD camera. The collected images are analyzed using ImageJ tools.

(a) (b)

Figure 6.4: Polycarbonate thin film transferred to a clamped slab of PDMS (a) before testing and (b) during testing.

## 6.4 Results and Discussion

### 6.4.1 Wrinkling Instabilities in Compression Tests

Wrinkling cracking experiments were carried out on polycarbonate thin films with thicknesses ranging from 41 nm to 250 nm. Since the film thicknesses are known, compression tests were conducted to determine the elastic modulus of the PC coating. Figure 6.5 shows the onset of wrinkles for a 191 nm thick film at relatively low levels of strain.

The compression test is a useful, non-destructive method to determine the moduli ratio of the materials in a support structure. If the moduli were known, a wrinkling wavelength can be predicted using Equation 6.5. Taking general values of moduli for polycarbonate[149,150] and PDMS[151–154] from literature, the wrinkling wavelength for PC films of a given thickness deposited onto PDMS can be determined. Conversely, the modulus for a unknown coating material can be determined if all other variables are known. Figure 6.6 shows the wrinkling wavelength predicted by Equation 6.5 is in good agreement with the experimental results across all thicknesses tested. The elastic modulus of the Lexan-130-111 polycarbonate is calculated to be $E = 1.8 \pm 0.1$ GPa, which is also in good agreement with that reported in literature.

Although Equation 6.3 predicts a much lower critical strain value at which wrinkles will form, these lower strains result in small wrinkles that are difficult to observe using the

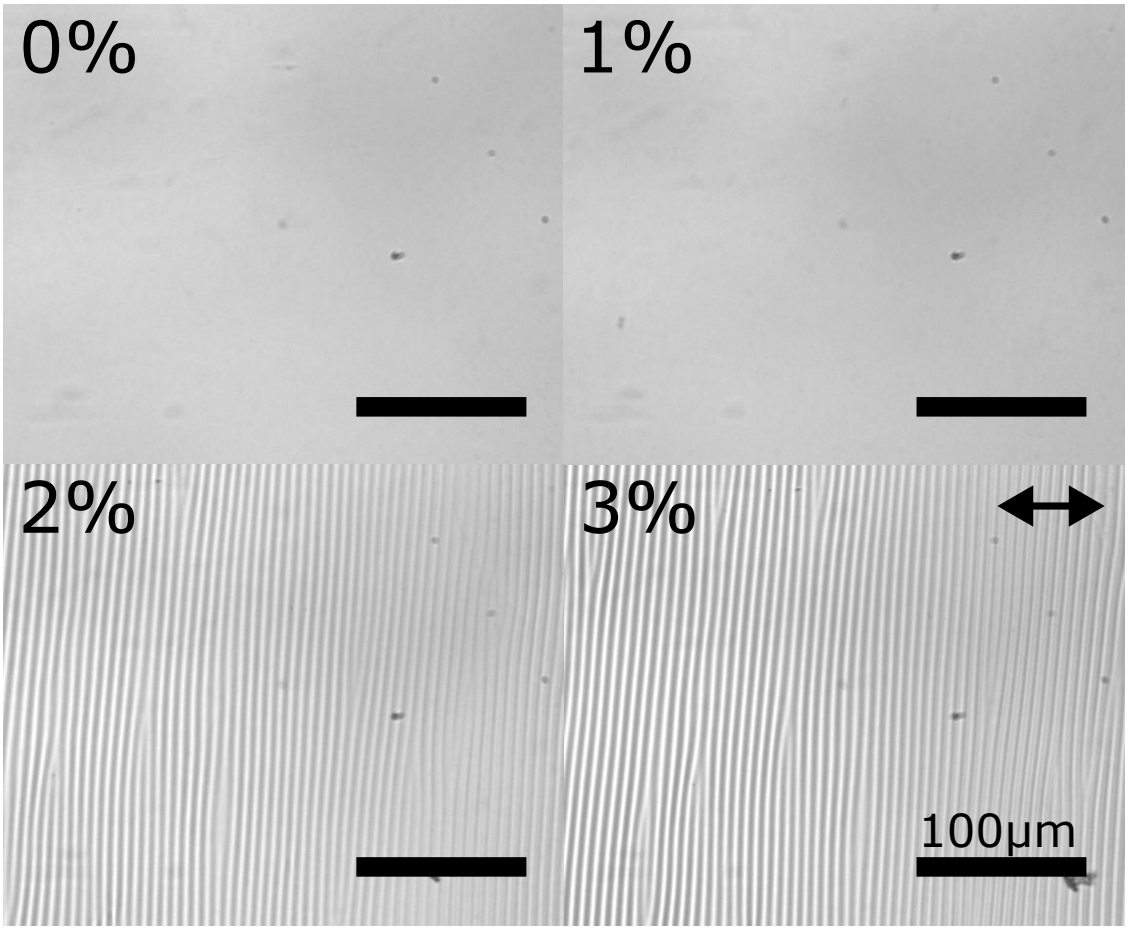


Figure 6.5: The onset of wrinkling instability for a 191 nm thick PC film under compressive strain.

optical microscope. Since this work was aimed at capturing the deformation behavior of the material, the emphasis was not put on observing the wrinkling wavelengths in compression. Nevertheless, Chung and coworkers[144] had employed a laser to create a diffraction pattern from the surface of these thin films to more accurately capture the critical wrinkling strain in a compression test.

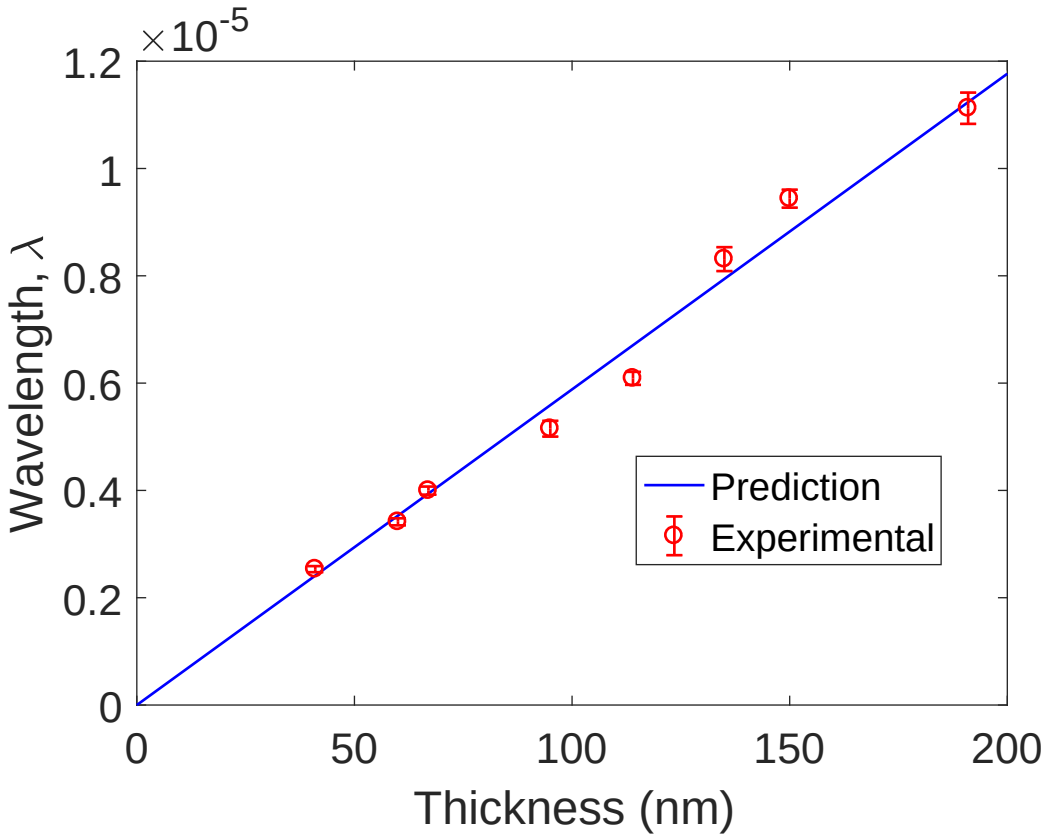


Figure 6.6: PC film thicknesses as a function of solution concentration and spin speeds. At low speeds (<1000rpm), film thicknesses vary greatly due to uneven drying.

### 6.4.2 Membrane Deformation during Uniaxial Tension

#### Deformation Zones

WC test in tension is carried out on polycarbonate thin films with thicknesses ranging from 40 nm to 200 nm. Figure 6.7 and Figure 6.8 show the deformation history of a 191 nm and a 41 nm film on PDMS substrates, respectively. The direction of stretch is denoted by the black arrows. In both cases, vertical bands appear perpendicular to the elongation direction before surface wrinkling. Again, this is in part due to the limitation of the optical microscope. These bands, though similar in appearance to the channel cracks observed in brittle films such as polystyrene, do no span the thickness of the film, nor does the film bifurcate along

these channels at increasing strains, up to 90%. These bands indicate regions at which the material has yielded in the form of a neck. These deformation zones (DZ) initiate at flaws and defects within the coating. Due to the support bilayer geometry, these flaws will propagate into long, continuous channels[155–157], as it is the most energetically favorable mode of dissipating the internal stresses caused by the applied strain.

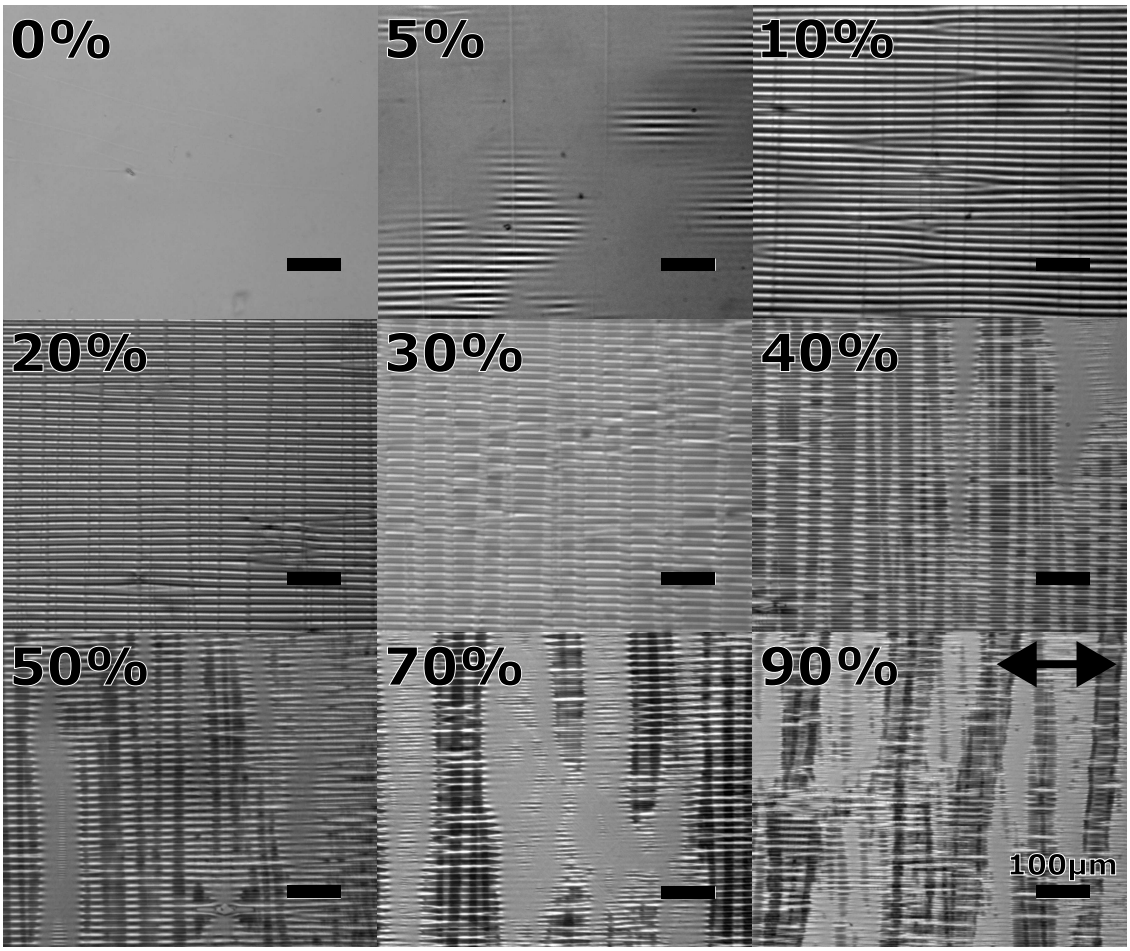


Figure 6.7: A 191 nm thick PC film under tension up to 90% strain. The direction of strain is denoted by the black arrows. Scale bar is 100$\mu$m.

For the 191 nm film, the channels grow in width as strain until neighboring yield zones connect. In contrast, the channel width for the 41 nm film does not grow significantly once formed, which suggest the film does not continue to yield at these regions, nor does the film

bifurcate along these channels, as seen in Figure 6.1. In order to accommodate the strain applied, new channels form to populate the surface of the film. The notable difference in the behavior of the channel growth suggest a bulk to thin film transition in the mechanism behind ductile yielding.

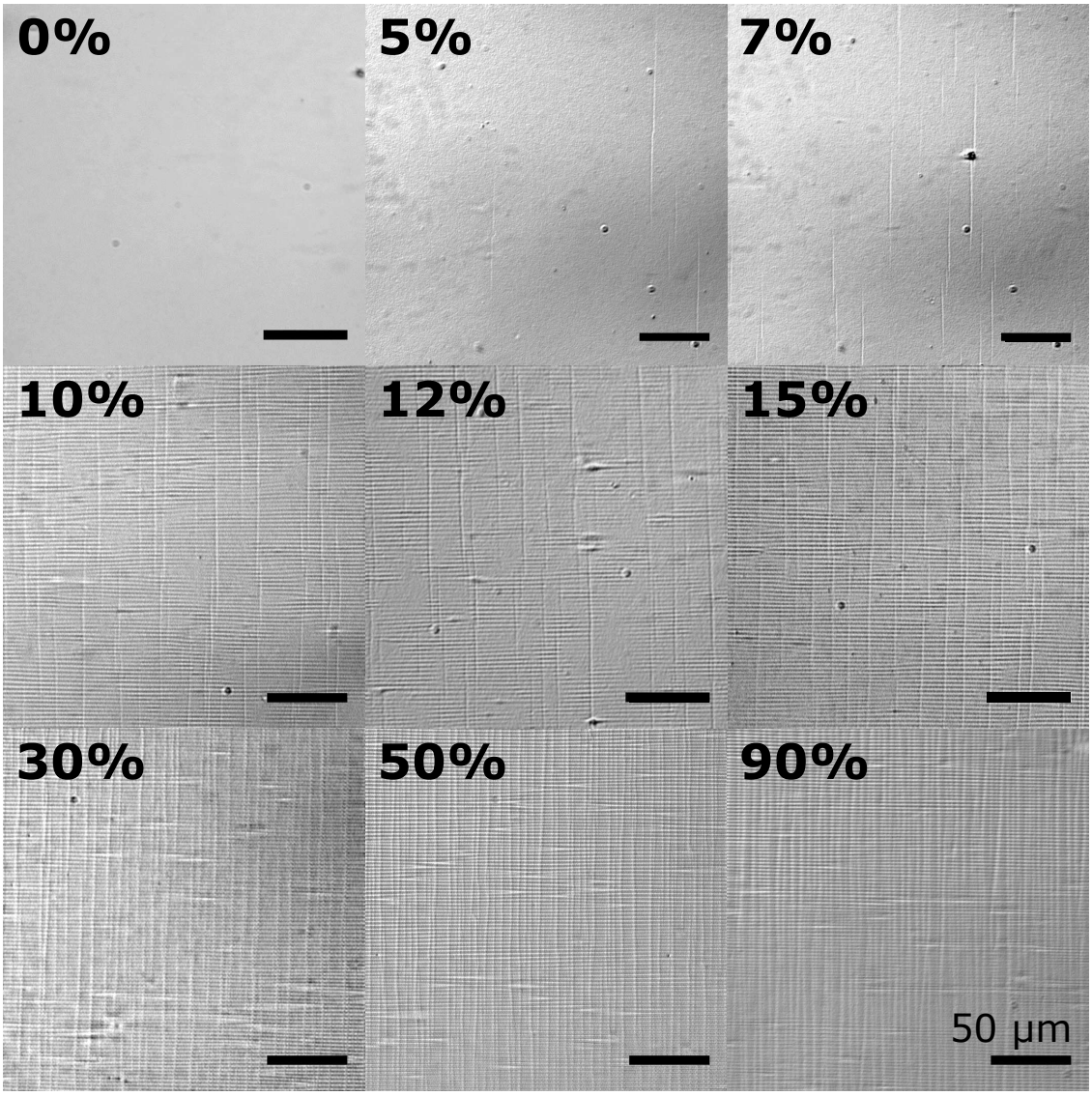


Figure 6.8: A 41 nm thick PC film under tension up to 90% strain. The direction of strain is denoted by the black arrows. Scale bar is 50$\mu$m.

An average fragment spacing, $\langle d_f \rangle$, can be extracted from the vertical channels. Figure 6.9a shows the fragment spacing between the necked regions for a 191 nm PC film. A black line with a power-law slope of 2 is plotted to guide the eye. For a typical brittle material, the measured crack spacing has a power-law of 1 relation to the applied strain. Here, due to the ductile nature of the polycarbonate, there is a much stronger dependence of the fragment spacing on the applied strain. In brittle fracture, a film will bifurcate as the applied strain doubles, and the strain energy is release in the formation of the channel crack. In ductile material, the strain energy is release through the formation of a neck. Since the neck does not span the thickness of the film, at the boundary of the neck, the material strain hardens, and the stress drops.

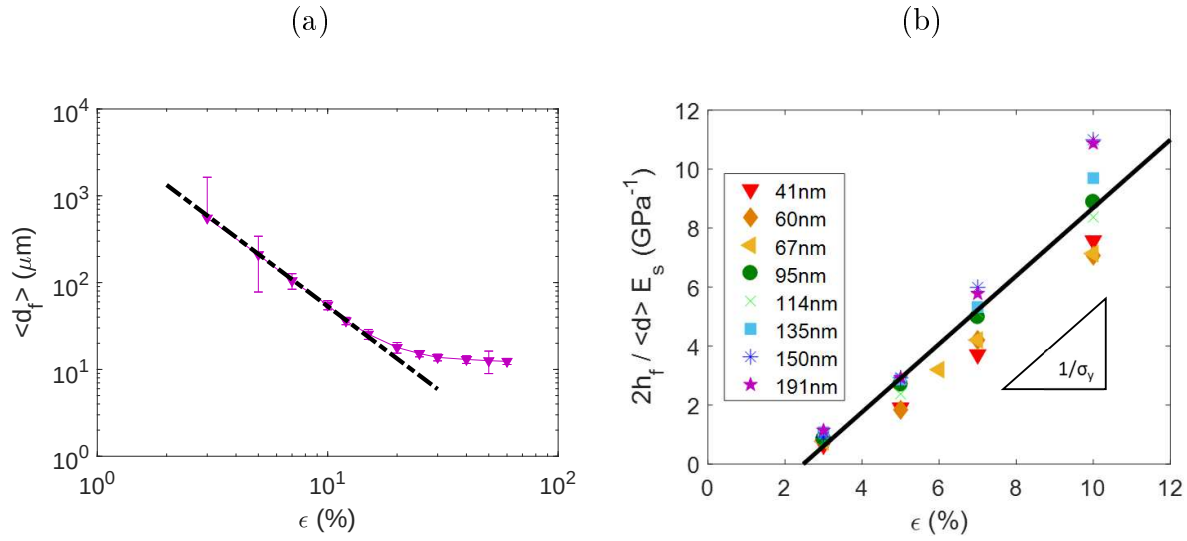


Figure 6.9: (a) The average fragment spacing between the necked regions for the 191 nm film. The black dotted line denotes a power-law fit with slope of 2. (b) Yield strength estimation for the polycarbonate films supported by a compliant substrate.

Due to the non-zero stress at the deformation zone edge, the film must undergo a greater number of necking events to accommodate the applied strain, which is why there is a stronger dependence of crack spacing on applied strain. By rearranging Equation 6.1, an estimation of yield strength of the material can be determined:

$$\frac{1}{\sigma_y} = \frac{2h_f(\varepsilon)}{\langle d_f \rangle E_s \varepsilon}$$

Of course, due to yielding of the film, the local film thickness is changing, as is denoted by the dependence of the thickness on strain, $h_f(\varepsilon)$. All film thicknesses tested exhibit a similar power-law of 2 behavior at strains below 20%. This suggests that the channel necks saturate the surface of the coating at around the same applied strain, independent of film thickness. The new equation is plotted against $\varepsilon$ in Figure 6.9b. A yield strength of $\sigma_y = 8.7$ MPa is estimated by taking the slope of the curve.

**Wrinkling Wavelength**

In both the 41nm and 191nm cases, surface instabilities begin to be apparent under an optical microscope at around 5% applied strain. This is consistent with the results collected from the compression tests, since the perpendicular compressive strain is around 2% due to PDMS having a Poisson's ratio of 0.5. Although the wrinkles develop across the entire surface of the sample, those in the 191 nm film disappear as the vertical deformation zones grow in width.

As the DZ's grow, the strain energy within the film decreases. As previously mentioned, due to yielding of the material, the wrinkling wavelength should decrease with increasing applied strain. This is especially evident in the 191nm film, where multiple wavelengths can be observed in a single snapshot (Figure 6.10).

Figure 6.10 is an image of a 191 nm thick PC film at 50% applied strain. Here, the light, smooth region is the necked deformation zones (DZ). Diagonal shear bands that are characteristic for polycarbonate materials can be observed. Surrounding these regions are wrinkles with relatively large wavelengths (denoted by the red square). Within these DZs, however, are wrinkles with wavelengths much lower than those of the surrounding area. In

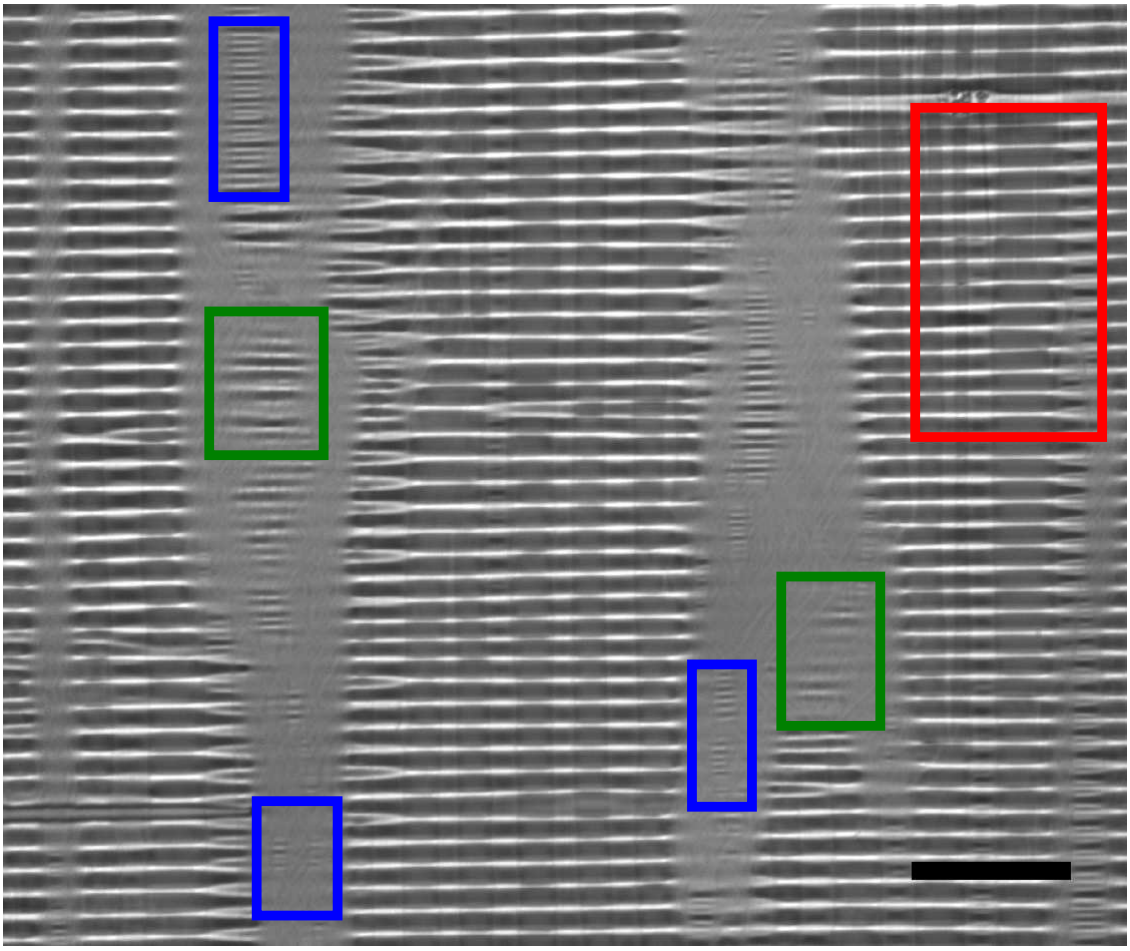

Figure 6.10: A 191 nm PC film at 50% strain. Scale bar indicates 100 $\mu$m. The different colored boxes denote regions with different wrinkling wavelengths.

the regions highlighted in blue and green, the wrinkles are of the deformed materials. If modulus was assumed to be constant, then a simple relation between wrinkling wavelength and film thickness can be used to determine the thickness at the deformed regions:

$$\frac{\lambda_1}{\lambda_2} = \frac{h_1}{h_2} \tag{6.6}$$

Table 6.1 summarizes the thickness values calculated from the wavelengths in the different deformation zones. The changes in thickness from these neighboring regions highlight the non-uniform deformation across the sample in the supported bilayer geometry. For com-

| $\lambda$ ($\varepsilon$ =50%) | Thickness (nm) |
|---|---|
| $\lambda_0$ (undeformed) | 190.4 ± 3.8 |
| $\lambda_1$ (red) | 164.2 ± 3.4 |
| $\lambda_2$ (green) | 93.0 ± 5.8 |
| $\lambda_3$ (blue) | 55.3 ± 0.4 |
| $\lambda_{min}$ ($\varepsilon$ =90%) | 27.6 ± 3.4 |

Table 6.1: Thickness measurements at deformation regions with varying wavelengths. The changes in thickness highlight the non-uniform deformation across the sample in the supported bilayer geometry. The minimum wavelength measured at 90% strain is reported for comparison.

parison, the smallest wavelength measured at 90% strain is also shown, and it shows a 85% reduction from the undeformed thickness in some extreme cases. These results showcase the extreme ductility and resistance to fracture for the PC thin films at large strains.

Outside of the necked regions, the wrinkling wavelength is an average across both the undeformed and deformed material. As a result, the average wrinkling wavelength decreases with increasing strain. In a free-standing specimen, the necked region will propagate through the length of the sample. In the bilayer structure, the substrate act to pin the coating, resulting in infinitesimally small tensile bars that yield separately. For polycarbonate samples, it is typical for the boundaries of the neck to undergo strain hardening[158–160]. Since the stresses at the deformed regions are much lower than those of the undeformed regions, and the boundaries present an extra energy barrier for the neck to propagate, it is reasonable for multiple DZs to populate the surface of the coating prior to the growth of the DZs. The small yielding and necking events contribute to the overall decrease in thickness, and by extension, the wrinkling wavelength.

This trend is apparent in all the film thicknesses tested, as shown in Figure 6.11. The undeformed wavelength measured from compression test is plotted for comparison to the results from the tension tests, and the observed results are in good agreement. The higher wavelength of thicker films indicate a greater bending stiffness, and highlight the strong

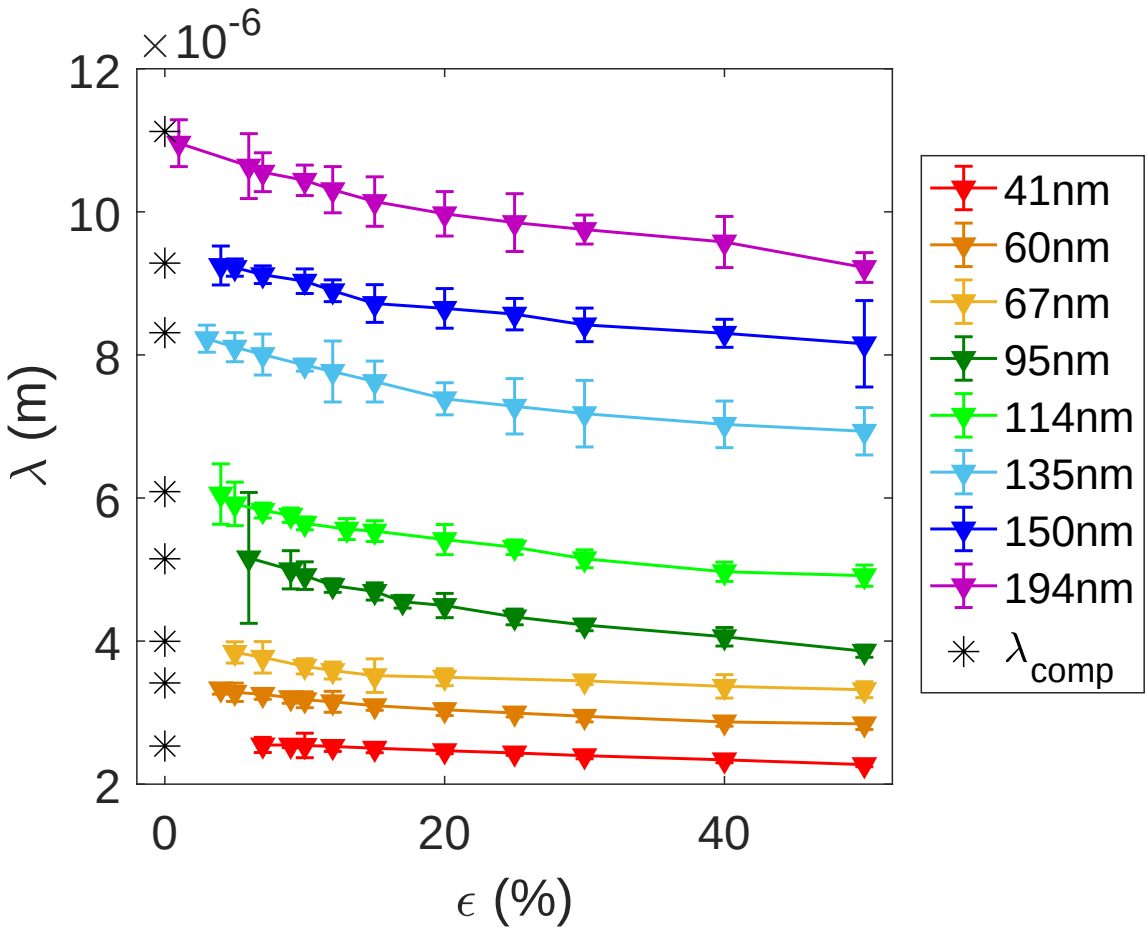


Figure 6.11: The wrinkling wavelength of PC films of different thicknesses at increasing applied strains. Black asterisks are results from the compressive tests.

thickness dependence of the wrinkling wavelength. Normalizing the wavelengths to the undeformed wavelength measured from the compression tests, an overall trend across all thicknesses can be mapped.

The decreasing in wrinkling wavelength can be viewed as the stretch ratio of the coating. As seen in Figure 6.12, across all thicknesses the stretch ratio collapses onto a single curve, with the exception of the 41 nm thick film. This deviation can be attributed to the bulk to thin film transition discussed previously, which may also contribute to the channel formation

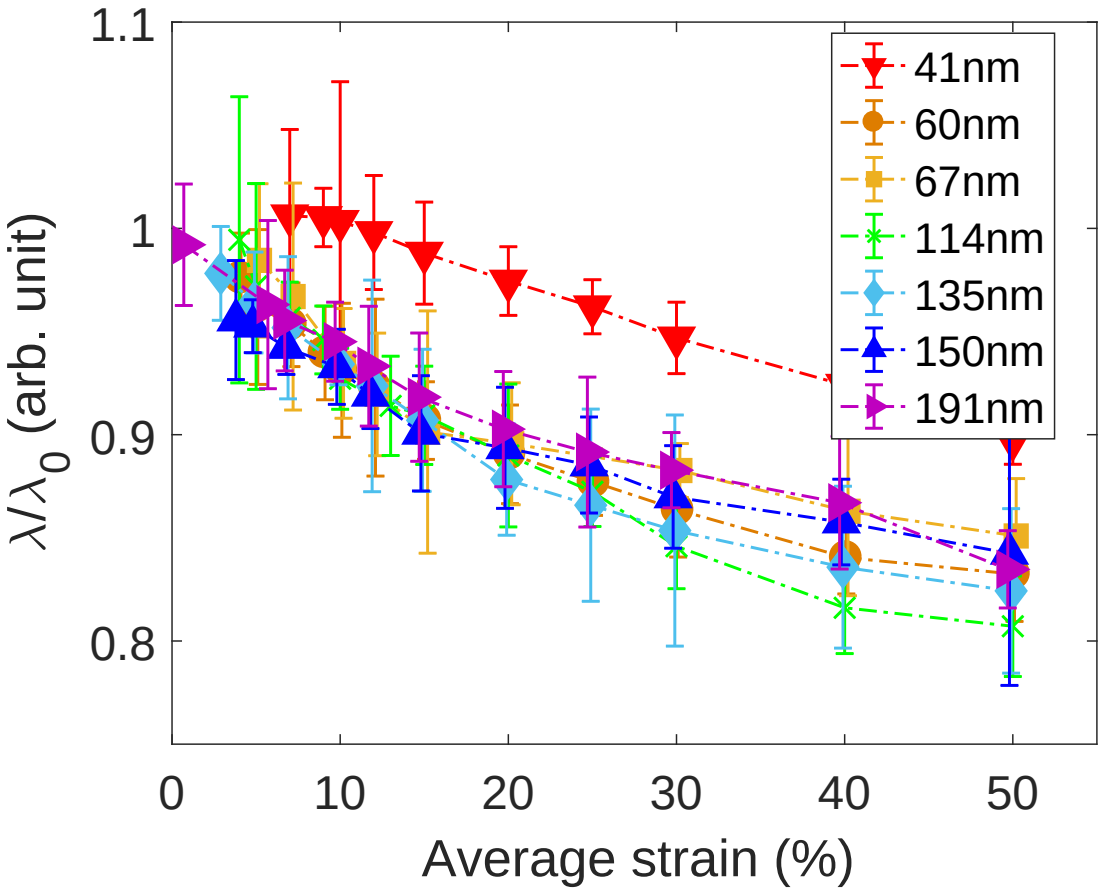


Figure 6.12: Wrinkling wavelength normalized to the undeformed wavelength, or the stretch ratio.

in the thinner films that resist further yielding. This deformation behavior is markedly different to those for PS films that undergo brittle fracture (Figure 6.1).

Another way to view this result is the decrease in the average thickness of the thin film at increasing applied strains. However, we must also consider the effect of modulus on the wrinkling wavelength in this non-linear regime, as the mechanical properties of post-yield sample may provide additional insight into the mechanism of ductile fracture in thin films. Although outside the scope of the current work, the strain-dependent amplitude of the wrinkling instabilities may contain additional useful information on the deformation histories

of the material. The amplitude can be related to the changing film thickenss and the applied strain by:

$$A_w = h(\varepsilon)\sqrt{\frac{\varepsilon - \varepsilon_c}{\varepsilon_c}} = h(\varepsilon)\sqrt{\varepsilon_0} \tag{6.7}$$

where $\varepsilon_c$ is the critical strain at which wrinkles first form, and $\varepsilon_0$ is the overstrain that make up the distance between each period. In brittle fracture materials, $h(\varepsilon) = h(0)$, and the amplitude of the wrinkles increase with increasing strain, and the wavelength remains constant. However, in materials that yield, the wavelength and the thickness both change with applied strain, and additional development to the current characterization technique is necessary to capture the amplitude information in these wrinkling-cracking experiments.

### Void Formation and Growth

The ability for PC thin films to continuously yield without catastrophic fracture make them extremely viable for applications in flexible electronic devices. For these applications, flexibility and resistance to failure under high strains is a primary focus for materials selection, since fracture or delamination of the support and protective coating may be detrimental to device operation.

Despite our best efforts during processing to avoid and remove voids and defects, some nevertheless remain within the sample structure. Figure 6.13 is a circular void found on the surface of a polycarbonate coating, a remnant of spin-coating and film transfer. The boundary of the circular void act to concentrate the stress, and in a typical fracture problem would lead to stress buildup and ultimately fracture in the direction perpendicular to the applied strain during tensile loading. Here, however, the coating does not fracture. Notably, vertical channels can be observed early on (5% strain), and these channels grow into deformation zones. As the material continues to stretch, the deformation zones merge together

to form wider bands. In the direction of the applied strain, the coating begins to delaminate from the substrate. The delaminated coating does not yield as the region experiences no stress from the strained substrate. This region to the sides of the void effectively bisects the deformation bands above and below the circle void.

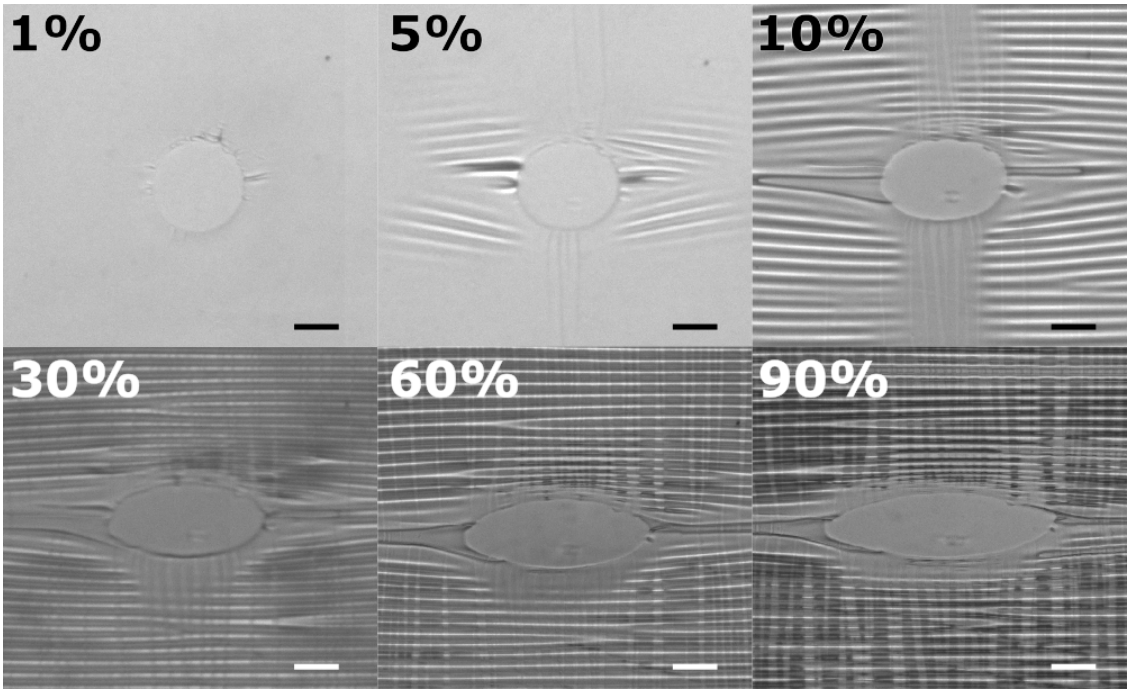


Figure 6.13: A circular void in a PC coating. Scale bar indicates 50 $\mu$m.

Sometimes an intrinsic defect will be large enough to bisect the coating. Figure 6.14 shows a more typical diamond-shaped void previously reported in literature[158,159,161]. Normally, these cracks will propagate and lead to macroscopic fracture of the material. Fortunately, in the support bilayer structure, the compliant substrate act to dissipate the stresses along the crack. Moreover, the ductile nature of the PC coating leads to a dulling of the crack tip and arrests catastrophic fracture of the material.

For applications as protective coating or transparent insulating layer in thin film electronics, this bilayer geometry of a stiff, ductile material on a compliant substrate proves to be exceptional at resisting fracture failures. The inhibition of crack propagation through

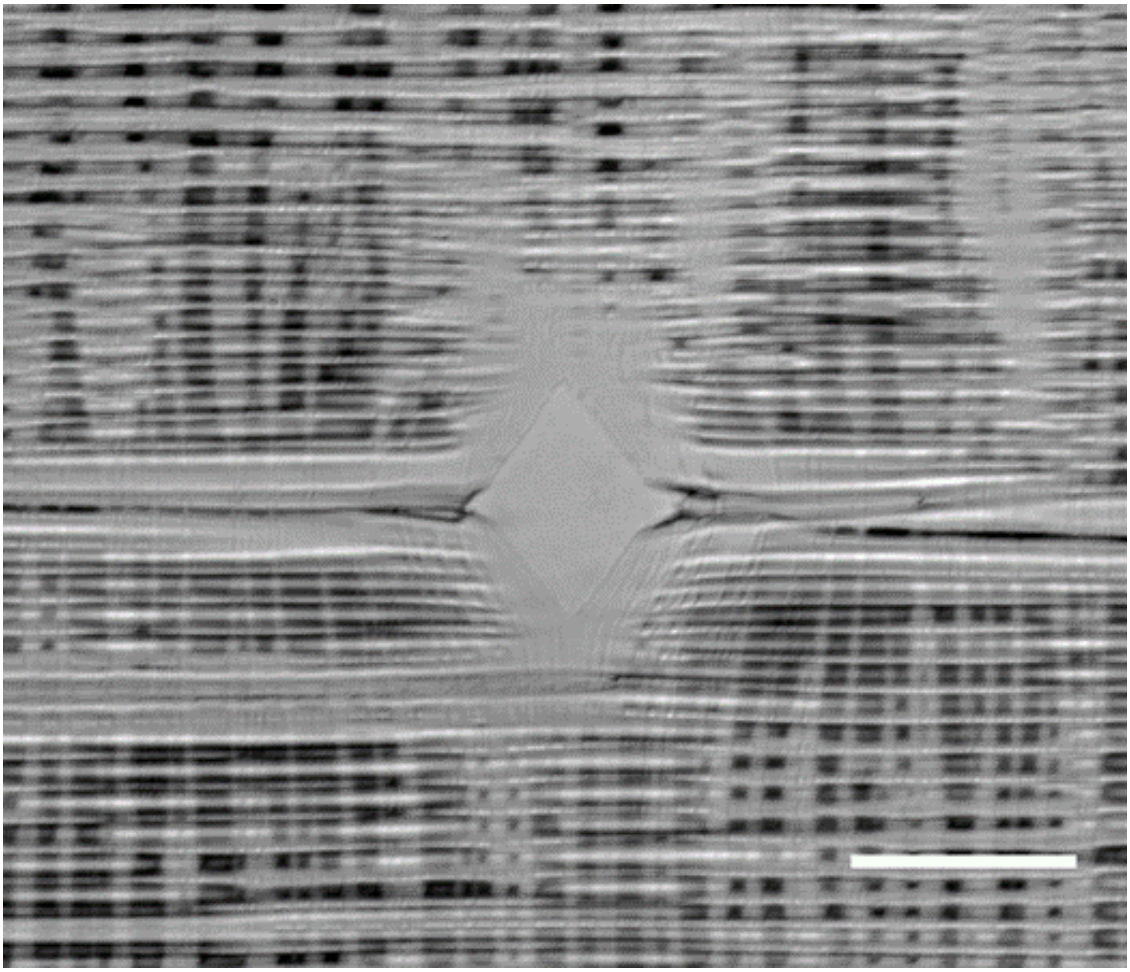

Figure 6.14: A diamond void in a PC coating at 90% applied strain. Scale bar indicates 100 $\mu$m.

exploiting the unique geometry enables materials that were previously inappropriate to be considered when designing future devices.

## 6.5 Conclusions

In this chapter large strain deformation experiments were performed on a supported bilayer of polycarbonate thin film on PDMS. A combined wrinkling-cracking method was employed to investigate the mechanical behavior of the ductile PC coating. The primary conclusions from this work are summarized as the following points:

- Wrinkling instabilities provide a simple, non-destructive method to characterize the elastic modulus of a thin coating when deposited onto a compliant substrate with a known modulus. The modulus ratio can be further used as a failure criterion for layer delamination.

- Polycarbonate thin films with thicknesses between 40 nm and 200 nm undergo primarily wrinkling instabilities instead of delamination at the applied strains tested.

- Due to material yielding, the wrinkling wavelength becomes dependent on the applied strain. As a result, changes in the wavelength can be used as a measurement of the material stretch ratio as it deforms.

- The supported bilayer geometry containing ductile polymers provides a promising engineering solution to mitigating fracture failure and circuit shorting for applications in flexible and wearable electronics. Additionally, polycarbonate thin films exhibit extraordinary ductility and stiffness at large strains, and maintain optical transparency throughout the experiments.

A combined wrinkling-cracking experiment is a useful tool for characterizing the mechanical properties of ultra thin films that are challenging to study using traditional testing methods. This simple, low-cost test can provide fast and accurate measurements of modulus and fracture toughness of any material, particularly those used in the aforementioned applications.

# Chapter 7

# Summary and Future Outlooks

## 7.1 Summary

This work opened up with a brief overview of ion-exchange membranes (IEMs), with specific considerations for proton exchange membrane found in numerous water treatment applications in Chapter 2. Membrane technology has become increasing pervasive in the modern era with the advent of portable devices and our ability to continuously shrink materials. While our materials library has exploded with new and novel materials with unique chemistry and geometries, processing-structure-properties of these new materials are still not well understood. In hoping to provide further insight on the material properties that are often overlooked, I build upon the the discussion of large deformation theory introduced in previous work by Dr. Anny Flory, Dr. David Brass, and later Dr. Evan Laprade, and expand on the development of a biaxial membrane inflation test designed to characterize the deformation behavior of thin films in aqueous environments that are relevant to industrial applications.

Applying the equibiaxial membrane inflation technique, Chapters 3 and 5 discussed investigations of materials systems designed for applications in aqueous environments. First, Chapter 3 investigates the mechanical properties and creep behavior of sulfonated pentablock copolymers with various chemical modifications in conjunction with membrane transport properties. The hydrated mechanical properties of these membranes were determined, and we found that higher degrees of sulfonation can be achieved by reducing the polymer fraction of the mid-block while maintaining comparable water transport. In addition, we found that by increasing the packing density of the pentablock copolymer by substituting the bulky t-butylstyrene with 4-methylstyrene, the mechanical strength of the membrane can be im-

proved. Chapter 5 builds upon the biaxial treatment to characterize the mechanical response of polyelectrolyte thin films in salt-containing aqueous media. The equibiaxial inflation technique enabled the characterization of polyelectrolyte complex films at the low-salt regime on the polyelectrolyte continuum. The relaxation behavior of these films in salt containing aqueous media reveal a power-law behavior similar to those previously observed in complex gels and fluids. A modified fractional Maxwell model call the fractional solid model was employed to describe and fit the relaxation behavior of these complex network solids at the limit of low-salts.

I provided additional insight on the processing-structure-property relationship of the sulfonated pentablock copolymers used in Chapter 3 using a combination of SAXS and GISAXS scattering techniques. I investigated the solution morphologies in blends of solvents with selective block solubility, as well as the effects of membrane processing methods. I found that higher-order structures of alternating lamellae and close-packed cylinders can be achieved by the use of binary solvent blends of polar and non-polar solutions, but these solution morphologies may be lost during membrane fabrication and solvent evaporation. A solvent vapor annealing process was introduced to recover the higher order structures previously observed. Additionally, preliminary results of water permeability reveal that water transport properties were independent of domain spacing and membrane morphology, and were primarily determined by the sulfonation levels.

In Chapter 6, a combined wrinkling and cracking methodology was introduced to characterize the mechanics of polycarbonate thin films. This work demonstrated that wrinkling instabilities can provide a simple, non-destructive method to characterize the elastic modulus of a thin coating when deposited onto a compliant substrate with a known modulus, and the modulus ratio can be further used as a failure criterion for layer delamination. It was found that a supported bilayer geometry provides a promising engineering solution to mitigating fracture failure and circuit shorting for applications in flexible and wearable electronics. Due

to material yielding, the wrinkling wavelength becomes dependent on the applied strain. As a result, changes in the wavelength can be used as a measurement of the material stretch ratio as it deforms.

## 7.2 Future Work

Chapters 3 and 5 demonstrated the applicability of an equibiaxial membrane inflation test in characterizing the deformation behavior of soft polymeric membranes in hydrated conditions that are are of more practical interest for many membrane materials that operate in wet conditions. The membrane inflation test is therefore a highly complimentary technique for any future membrane mechanical testing. In Chapter 5, the mechanical response of polyelectrolyte thin films in salt-containing aqueous media was investigated. In a separate work, we had found that the polyelectrolyte complex network relaxation behavior varies greatly depending on the species of salt used. Future work should systematically investigate the effect of other charged species as well as multi-valent ions on the deformation behavior PEC films in aqueous conditions, and to develop a more appropriate model for describing the relaxation behavior cross the polyelectrolyte continuum.

In Chapter 4 we demonstrated that solvent quality can have a significant effect on the morphology of the resulting polymer using a solvent blend of DMAc and toluene. Both DMAc and toluene are moderately good solvents for the non-sulfonated blocks, while only DMAc is a good solvent for the sulfonated block. It is recommended to investigate further the effects of solvent selectivity on the final morphology and properties of multiblock polymer systems that include co-solvents that more strongly contrast each other to bring about more pronounced effects in the micro-structure of polymers in solutions. The effect of volume fraction of the component blocks was also investigated, primarily of the unmodified sulfonated pentablock (P-ref) and the pentablock with a shortened sulfonated mid-block

(P-short). A more comprehensive study on the effect of block sizes (i.e. long ionic-block and short uncharged blocks) can lead the a larger variety of less common morphologies and to expand our current understanding of the structure-property relationship of ion-containing block copolymer.

Lastly in Chapter 6, we investigated the ductile fracture mechanisms in a supported bilayer geometry as a function of film thickness, and we found that the deformation behavior begins to deviate at diminishing film thicknesses starting at 40nm. It would be interesting to continue the exploration into the ultra-thin regime to see if nano-confinement effects begin to affect these ductile thin films. In addition, a single strain rate was used throughout the experiments. There is significant interest currently in the field of impact mitigation to study strain rate dependent fracture behaviors in materials. Preliminary results show a dependence of the wrinkling wavelength on the strain rate of the test, indicating that material yielding has a rate dependence.

Future testing should examine how increasing strain rates could affect the fracture behavior of the materials. A rate-dependent ductile-brittle transition could provide significant impact in our current understanding of fracture behavior in ductile materials.

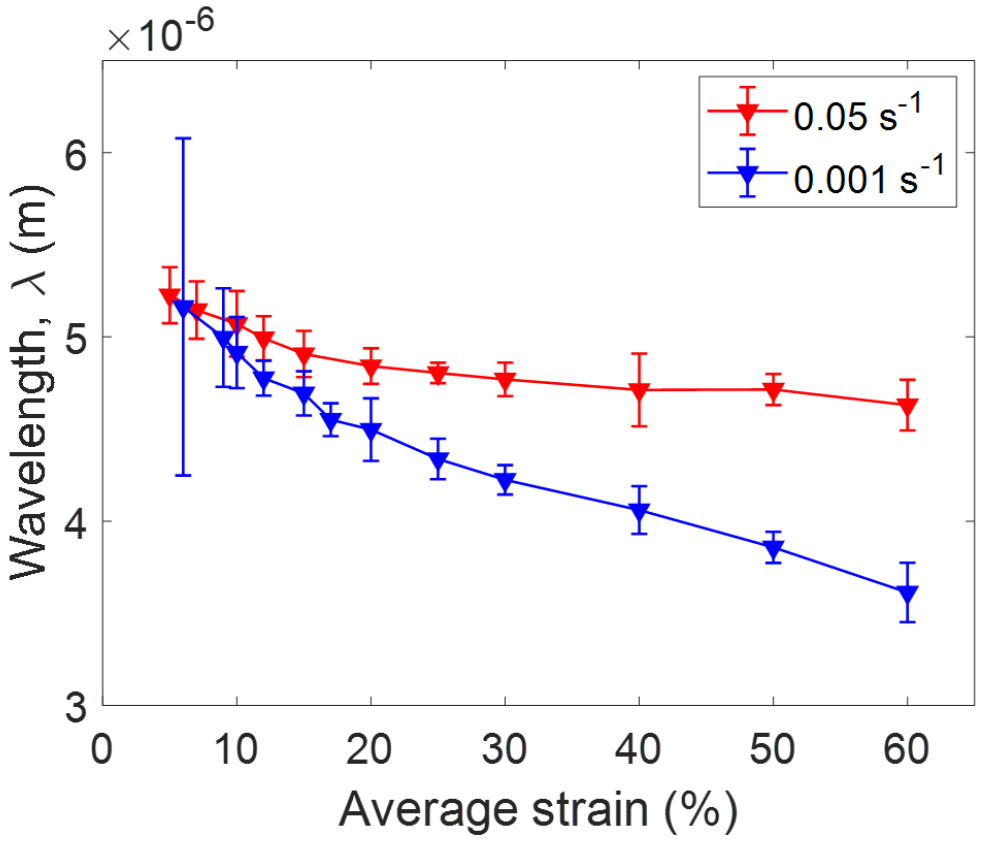


Figure 7.1: The wrinkling wavelength of a 100 nm thick PC film strained at two different rates.

# References

[1] P Genova-Dimitrova, B Baradie, D Foscallo, C Poinsignon, and J. Y Sanchez. Ionomeric membranes for proton exchange membrane fuel cell (PEMFC): sulfonated polysulfone associated with phosphatoantimonic acid. *Journal of Membrane Science*, 185(1):59–71, April 2001.

[2] M. Alger. *Polymer Science Dictionary*. Springer Science & Business Media, December 1996.

[3] Tongwen Xu. Ion exchange membranes: State of their development and perspective. *Journal of Membrane Science*, 263(1–2):1–29, October 2005.

[4] Kah Peng Lee, Tom C. Arnot, and Davide Mattia. A review of reverse osmosis membrane materials for desalination—Development to date and future potential. *Journal of Membrane Science*, 370(1–2):1–22, March 2011.

[5] Angelo Basile, Alfredo Cassano, and Navin K. Rastogi. *Advances in Membrane Technologies for Water Treatment: Materials, Processes and Applications*. Elsevier, February 2015.

[6] Juana Benavente, Jose M Garcia, Robert Riley, Angel E Lozano, and Javier de Abajo. Sulfonated poly(ether ether sulfones): Characterization and study of dielectrical properties by impedance spectroscopy. *Journal of Membrane Science*, 175(1):43–52, August 2000.

[7] Jochen Meier-Haack, Antje Taeger, Claus Vogel, Kornelia Schlenstedt, Wolfgang Lenk, and Dieter Lehmann. Membranes from sulfonated block copolymers for use in fuel cells. *Separation and Purification Technology*, 41(3):207–220, February 2005.

[8] Byungchan Bae, Kenji Miyatake, and Masahiro Watanabe. Synthesis and Properties of Sulfonated Block Copolymers Having Fluorenyl Groups for Fuel-Cell Applications. *ACS Applied Materials & Interfaces*, 1(6):1279–1286, June 2009.

[9] Michael A. Hickner. Ion-containing polymers: new energy & clean water. *Materials Today*, 13(5):34–41, May 2010.

[10] Hongyang Ma, Christian Burger, Benjamin S. Hsiao, and Benjamin Chu. Highly Permeable Polymer Membranes Containing Directed Channels for Water Purification. *ACS Macro Letters*, 1(6):723–726, June 2012.

[11] J. Yeo, S. Y. Kim, S. Kim, D. Y. Ryu, T.-H. Kim, and M. J. Park. Mechanically and structurally robust sulfonated block copolymer membranes for water purification applications. *Nanotechnology*, 23(24):245703, June 2012.

[12] Gavin J. Irvine, Sahadevan Rajesh, Michael Georgiadis, and William A. Phillip. Ion Selective Permeation Through Cellulose Acetate Membranes in Forward Osmosis. *Environmental Science & Technology*, 47(23):13745–13753, December 2013.

[13] G. Gebel. Structural evolution of water swollen perfluorosulfonated ionomers from dry membrane to solution. *Polymer*, 41(15):5829–5838, July 2000.

[14] Sumit Kundu, Leonardo C. Simon, Michael Fowler, and Stephen Grot. Mechanical properties of Nafion electrolyte membranes under hydrated conditions. *Polymer*, 46(25):11707–11715, November 2005.

[15] Jianqi Zhang, Dorthe Posselt, Alessandro Sepe, Xuhu Shen, Jan Perlich, Detlef-M. Smilgies, and Christine M. Papadakis. Structural Evolution of Perpendicular Lamellae in Diblock Copolymer Thin Films during Solvent Vapor Treatment Investigated by

Grazing-Incidence Small-Angle X-Ray Scattering. *Macromolecular Rapid Communications*, 34(16):1289–1295, August 2013.

[16] Jun Xing Leong, Wan Ramli Wan Daud, Mostafa Ghasemi, Kien Ben Liew, and Manal Ismail. Ion exchange membranes as separators in microbial fuel cells for bioenergy conversion: A comprehensive review. *Renewable and Sustainable Energy Reviews*, 28:575–587, December 2013.

[17] Hossein Ghassemi, James E. McGrath, and Thomas A. Zawodzinski. Multiblock sulfonated–fluorinated poly(arylene ether)s for a proton exchange membrane fuel cell. *Polymer*, 47(11):4132–4139, May 2006.

[18] Anke Nabe, Eberhard Staude, and Georges Belfort. Surface modification of polysulfone ultrafiltration membranes and fouling by BSA solutions. *Journal of Membrane Science*, 133(1):57–72, September 1997.

[19] Sangyoup Lee and Menachem Elimelech. Relating Organic Fouling of Reverse Osmosis Membranes to Intermolecular Adhesion Forces. *Environmental Science & Technology*, 40(3):980–987, February 2006.

[20] M. Pontié, S. Ben Rejeb, and J. Legrand. Anti-microbial approach onto cationic-exchange membranes. *Separation and Purification Technology*, 101:91–97, November 2012.

[21] Shuai Liang, Genggeng Qi, Kang Xiao, Jianyu Sun, Emmanuel P. Giannelis, Xia Huang, and Menachem Elimelech. Organic fouling behavior of superhydrophilic polyvinylidene fluoride (PVDF) ultrafiltration membranes functionalized with surface-tailored nanoparticles: Implications for organic fouling in membrane bioreactors. *Journal of Membrane Science*, 463:94–101, August 2014.

[22] Geoffrey M. Geise, Hae-Seung Lee, Daniel J. Miller, Benny D. Freeman, James E. McGrath, and Donald R. Paul. Water purification by membranes: The role of polymer science. *Journal of Polymer Science Part B: Polymer Physics*, 48(15):1685–1718, June 2010.

[23] Thomas A. Zawodzinski, Michal Neeman, Laurel O. Sillerud, and Shimshon Gottesfeld. Determination of water diffusion coefficients in perfluorosulfonate ionomeric membranes. *The Journal of Physical Chemistry*, 95(15):6040–6044, July 1991.

[24] Thomas A. Zawodzinski, Charles Derouin, Susan Radzinski, Ruth J. Sherman, Van T. Smith, Thomas E. Springer, and Shimshon Gottesfeld. Water Uptake by and Transport Through Nafion® 117 Membranes. *Journal of The Electrochemical Society*, 140(4):1041–1047, April 1993.

[25] Thomas M. Quinn and Alan J. Grodzinsky. Longitudinal modulus and hydraulic permeability of poly(methacrylic acid) gels: effects of charge density and solvent content. *Macromolecules*, 26(16):4332–4338, August 1993.

[26] Liesl K. Massey. *Permeability Properties of Plastics and Elastomers, 2nd Ed.: A Guide to Packaging and Barrier Materials*. William Andrew, January 2003.

[27] Laurence W. McKeen. *Permeability Properties of Plastics and Elastomers*. William Andrew, September 2011.

[28] David A. Brass and Kenneth R. Shull. Contact Studies of Weakly Compressed PEG Brushes with a Quartz Crystal Resonator. *Langmuir*, 22(22):9225–9233, October 2006.

[29] M.A. Biot. General Theory of Three-Dimensional Consolidation. *Journal of Applied Physics*, 12(2):155–164, February 1941.

[30] M. Adam and M. Delsanti. Dynamical properties of polymer solutions in good solvent by Rayleigh scattering experiments. *Macromolecules*, 10(6):1229, 1977.

[31] G.M. Geise, B.D. Freeman, and D.R. Paul. Characterization of a sulfonated pentablock copolymer for desalination applications. *Polymer*, 51(24):5815–5822, November 2010.

[32] Wei-Chun Lin, Kenneth R. Shull, Chung-Yuen Hui, and Yu-Yun Lin. Contact measurement of internal fluid flow within poly(n-isopropylacrylamide) gels. *The Journal of Chemical Physics*, 127(9):094906, September 2007.

[33] MaryTheresa M. Pendergast and Eric M.V. Hoek. A review of water treatment membrane nanotechnologies. *Energy & Environmental Science*, 4(6):1946, 2011.

[34] Yuyan Shao, Geping Yin, Zhenbo Wang, and Yunzhi Gao. Proton exchange membrane fuel cell from low temperature to high temperature: Material challenges. *Journal of Power Sources*, 167(2):235–242, May 2007.

[35] Saswata Bose, Tapas Kuila, Thi Xuan Hien Nguyen, Nam Hoon Kim, Kin-tak Lau, and Joong Hee Lee. Polymer membranes for high temperature proton exchange membrane fuel cell: Recent advances and challenges. *Progress in Polymer Science*, 36(6):813–843, June 2011.

[36] Robert J. Petersen. Composite reverse osmosis and nanofiltration membranes. *Journal of Membrane Science*, 83(1):81–150, August 1993.

[37] Federico A. Pacheco, Ingo Pinnau, Martin Reinhard, and James O. Leckie. Characterization of isolated polyamide thin films of RO and NF membranes using novel TEM techniques. *Journal of Membrane Science*, 358(1–2):51–59, August 2010.

[38] Joung-Eun Gu, Seunghye Lee, Christopher M. Stafford, Jong Suk Lee, Wansuk Choi, Bo-Young Kim, Kyung-Youl Baek, Edwin P. Chan, Jun Young Chung, Joona Bang,

and Jung-Hyun Lee. Molecular Layer-by-Layer Assembled Thin-Film Composite Membranes for Water Desalination. *Advanced Materials*, 25(34):4778–4782, 2013.

[39] Gui Min Shi, Jian Zuo, Shyuan Hong Tang, Shawn Wei, and Tai Shung Chung. Layer-by-layer (LbL) polyelectrolyte membrane with Nexar polymer as a polyanion for pervaporation dehydration of ethanol. *Separation and Purification Technology*, 140:13–22, January 2015.

[40] Lu Yan, Yu Shui Li, Chai Bao Xiang, and Shun Xianda. Effect of nano-sized Al2o3-particle addition on PVDF ultrafiltration membrane performance. *Journal of Membrane Science*, 276(1-2):162–167, May 2006.

[41] Carmen Manea and Marcel Mulder. Characterization of polymer blends of polyethersulfone/sulfonated polysulfone and polyethersulfone/sulfonated polyetheretherketone for direct methanol fuel cell applications. *Journal of Membrane Science*, 206(1-2):443–453, August 2002.

[42] Jae-Hong Choi, Carl L. Willis, and Karen I. Winey. Structure-property relationship in sulfonated pentablock copolymers. *Journal of Membrane Science*, 394-395:169–174, March 2012.

[43] Jonghyun Choi, Kyung Min Lee, Ryszard Wycisk, Peter N. Pintauro, and Patrick T. Mather. Nanofiber Network Ion-Exchange Membranes. *Macromolecules*, 41(13):4569–4572, July 2008.

[44] Carl Willis, Dale Handlin, Scott TRENOR, and Brian MATHER. Sulfonated block copolymers, method for making same, and various uses for such block copolymers, January 2007. U.S. Classification 525/314; International Classification C08F297/00; Cooperative Classification Y10T428/31855, Y10T442/387,

Y10T442/3886, Y10T442/20, Y10T428/31938, Y10T442/3976, Y10T442/676, Y10T428/31931, Y10T442/668, Y10T428/249921, Y10T442/678, Y02E60/522, H01M2/1633, B01D71/28, H01M4/661, B01D71/82, Y02E60/122, B01D71/80, A61F2013/530489, H01M2004/027, C08F8/36, B01D71/40, B01D71/26, Y02E60/523, H01M4/131, B01D69/10; European Classification C08F8/36, B01D69/10, H01M2/16B5, H01M4/66A, B01D71/82, B01D71/80, H01M4/131.

[45] Sudhir Mani, R. A. Weiss, C. E. Williams, and S. F. Hahn. Microstructure of Ionomers Based on Sulfonated Block Copolymers of Polystyrene and Poly(ethylene-alt-propylene). *Macromolecules*, 32(11):3663–3670, June 1999.

[46] Bokyung Kim, Jinhwan Kim, and Bumsuk Jung. Morphology and transport properties of protons and methanol through partially sulfonated block copolymers. *Journal of Membrane Science*, 250(1-2):175–182, March 2005.

[47] Evan J. Laprade, Chya-Yan Liaw, Zhang Jiang, and Kenneth R. Shull. Mechanical and microstructural characterization of sulfonated pentablock copolymer membranes. *Journal of Polymer Science Part B: Polymer Physics*, 53(1):39–47, January 2015.

[48] Philip J. Griffin, Grace B. Salmon, Jamie Ford, and Karen I. Winey. Predicting the solution morphology of a sulfonated pentablock copolymer in binary solvent mixtures. *Journal of Polymer Science Part B: Polymer Physics*, 54(2):254–262, January 2016.

[49] Tomonori Saito, Hunter D. Moore, and Michael A. Hickner. Synthesis of Midblock-Sulfonated Triblock Copolymers. *Macromolecules*, 43(2):599–601, January 2010.

[50] B. K. Vaĭnshteĭn, 1921, B. K. Vaĭnshteĭn, and 1921. Diffraction of X-rays by chain molecules. 1966.

[51] Y. K. Levine. X-ray diffraction studies of membranes. *Progress in Surface Science*, 3:279–352, January 1973.

[52] Detlef-M. Smilgies, Peter Busch, Christine M. Papadakis, and Dorthe Posselt. Characterization of polymer thin films with small-angle X-ray scattering under grazing incidence (GISAXS). *Synchrotron Radiation News*, 15(5):35–42, September 2002.

[53] Marvin Y. Paik, Joan K. Bosworth, Detlef-M. Smilges, Evan L. Schwartz, Xavier Andre, and Christopher K. Ober. Reversible Morphology Control in Block Copolymer Films via Solvent Vapor Processing: An in Situ GISAXS Study. *Macromolecules*, 43(9):4253–4260, May 2010.

[54] Laura Mazzola. Commercializing nanotechnology. *Nature Biotechnology*, 21:1137, October 2003.

[55] Mihail C Roco. Nanotechnology: convergence with modern biology and medicine. *Current Opinion in Biotechnology*, 14(3):337–346, June 2003.

[56] Alkhateb Hunain, Al-Ostaz Ahmed, Cheng Alexander H.-D., and Li Xiaobing. Materials Genome for Graphene-Cement Nanocomposites. *Journal of Nanomechanics and Micromechanics*, 3(3):67–77, September 2013.

[57] Juan J. de Pablo, Barbara Jones, Cora Lind Kovacs, Vidvuds Ozolins, and Arthur P. Ramirez. The Materials Genome Initiative, the interplay of experiment, theory and computation. *Current Opinion in Solid State and Materials Science*, 18(2):99–117, April 2014.

[58] Z. Bartczak, A. S. Argon, R. E. Cohen, and M. Weinberg. Toughness mechanism in semi-crystalline polymer blends: I. High-density polyethylene toughened with rubbers. *Polymer*, 40(9):2331–2346, April 1999.

[59] Erich D. Bain, Daniel B. Knorr, Adam D. Richardson, Kevin A. Masser, Jian Yu, and Joseph L. Lenhart. Failure processes governing high-rate impact resistance of epoxy resins filled with core-shell rubber nanoparticles. *Journal of Materials Science*, 51(5):2347–2370, March 2016.

[60] Joanna Pach, Dariusz Pyka, Krzysztof Jamroziak, and Paulina Mayer. The experimental and numerical analysis of the ballistic resistance of polymer composites. *Composites Part B: Engineering*, 113:24–30, March 2017.

[61] Zvi Rosenberg and Roman Kositski. Deep indentation and terminal ballistics of polycarbonate. *International Journal of Impact Engineering*, 103:225–230, May 2017.

[62] Paul Podsiadlo, Ellen M. Arruda, Eugene Kheng, Anthony M. Waas, Jungwoo Lee, Kevin Critchley, Ming Qin, Eric Chuang, Amit K. Kaushik, Hyoung-Sug Kim, Ying Qi, Si-Tae Noh, and Nicholas A. Kotov. LBL Assembled Laminates with Hierarchical Organization from Nano- to Microscale: High-Toughness Nanomaterials and Deformation Imaging. *ACS Nano*, 3(6):1564–1572, June 2009.

[63] J. M. Serpico, S. G. Ehrenberg, J. J. Fontanella, X. Jiao, D. Perahia, K. A. McGrady, E. H. Sanders, G. E. Kellogg, and G. E. Wnek. Transport and Structural Studies of Sulfonated Styrene-Ethylene Copolymer Membranes. *Macromolecules*, 35(15):5916–5921, July 2002.

[64] Donald D. Joye, Gary W. Poehlein, and Costel D. Denson. A Bubble Inflation Technique for the Measurement of Viscoelastic Properties in Equal Biaxial Extensional Flow. *Transactions of The Society of Rheology (1957-1977)*, 16(3):421–445, September 1972.

[65] Maria N. Charalambides, Leonard Wanigasooriya, Gordon J. Williams, and Sumana Chakrabarti. Biaxial deformation of dough using the bubble inflation technique. I. Experimental. *Rheologica Acta*, 41(6):532–540, January 2002.

[66] S. M. Goh and B. S. Cheng. Extracting the stress-strain properties of non-linear viscoelastic materials using the bubble inflation test. *Rheologica Acta*, 53(4):295–301, March 2014.

[67] Rong Long, Kenneth R. Shull, and Chung-Yuen Hui. Large deformation adhesive contact mechanics of circular membranes with a flat rigid substrate. *Journal of the Mechanics and Physics of Solids*, 58(9):1225–1242, September 2010.

[68] C. D. Denson and R. J. Gallo. Measurements on the biaxial extension viscosity of bulk polymers: The inflation of a thin polymer sheet. *Polymer Engineering & Science*, 11(2):174–176, March 1971.

[69] Carl R. Mcmillin. Characterization of Hexsyn, a Polyolefin Rubber. *Journal of Biomaterials Applications*, 2(1):3–99, January 1987.

[70] M. Cakmak, Y. D. Wang, and M. Simhambhatla. Processing characteristics, structure development, and properties of uni and biaxially stretched poly(ethylene 2,6 naphthalate) (PEN) films. *Polymer Engineering & Science*, 30(12):721–733, June 1990.

[71] M. Rachik, F. Schmidtt, N. Reuge, Y. Le Maoult, and F. Abbeé. Elastomer biaxial characterization using bubble inflation technique. II: Numerical investigation of some constitutive models. *Polymer Engineering & Science*, 41(3):532–541, March 2001.

[72] N. Reuge, F. M. Schmidt, Y. Le Maoult, M. Rachik, and F. Abbé. Elastomer biaxial characterization using bubble inflation technique. I: Experimental investigations. *Polymer Engineering & Science*, 41(3):522–531, 2001.

[73] C. Galliot and R.H. Luchsinger. Uniaxial and biaxial mechanical properties of ETFE foils. *Polymer Testing*, 30(4):356–365, June 2011.

[74] P. A. O'Connell and G. B. McKenna. Novel nanobubble inflation method for determining the viscoelastic properties of ultrathin polymer films. *Review of Scientific Instruments*, 78(1):013901, January 2007.

[75] Yongqiang Li, David A. Dillard, Scott W. Case, Michael W. Ellis, Yeh-Hung Lai, Craig S. Gittleman, and Daniel P. Miller. Fatigue and creep to leak tests of proton exchange membranes using pressure-loaded blisters. *Journal of Power Sources*, 194(2):873–879, December 2009.

[76] Evan J. Laprade, Rong Long, Jonathan T. Pham, Jimmy Lawrence, Todd Emrick, Alfred J. Crosby, Chung-Yuen Hui, and Kenneth R. Shull. Large Deformation and Adhesive Contact Studies of Axisymmetric Membranes. *Langmuir*, 29(5):1407–1419, February 2013.

[77] Shawn H. Chen, Carl Willis, and Kenneth R. Shull. Water transport and mechanical response of block copolymer ion-exchange membranes for water purification. *Journal of Membrane Science*, 544(Supplement C):388–396, December 2017.

[78] A. H. Bloksma. A calculation of the shape of the Alveograms of some rheological model substances. *Cereal Chem.*, 34:126–136, 1957.

[79] Maria N. Charalambides, Leonard Wanigasooriya, J. Gordon Williams, Suk M. Goh, and Sumana Chakrabarti. Large deformation extensional rheology of bread dough. *Rheologica Acta*, 46(2):239–248, April 2006.

[80] Moon Jeong Park and Nitash P. Balsara. Phase Behavior of Symmetric Sulfonated Block Copolymers. *Macromolecules*, 41(10):3678–3687, May 2008.

[81] Vivek Kapur, John C. Charkoudian, Stephen B. Kessler, and John L. Anderson. Hydrodynamic Permeability of Hydrogels Stabilized within Porous Membranes. *Industrial & Engineering Chemistry Research*, 35(9):3179–3185, January 1996.

[82] L. Pisani. Simple Expression for the Tortuosity of Porous Media. *Transport in Porous Media*, 88(2):193–203, June 2011.

[83] Onnuri Kim, Sung Yeon Kim, Joungphil Lee, and Moon Jeong Park. Building Less Tortuous Ion-Conduction Pathways Using Block Copolymer Electrolytes with a Well-Defined Cubic Symmetry. *Chemistry of Materials*, 28(1):318–325, January 2016.

[84] Masayuki Tokita and Toyoichi Tanaka. Friction coefficient of polymer networks of gels. *The Journal of Chemical Physics*, 95(6):4613–4619, September 1991.

[85] Masayuki Tokita. Friction between polymer networks of gels and solvent. In Prof K. Dušek, editor, *Responsive Gels: Volume Transitions II*, number 110 in Advances in Polymer Science, pages 27–47. Springer Berlin Heidelberg, 1993.

[86] Carl Lesley Willis, Dale Lee Handlin Jr, Scott Russell Trenor, and Brian Douglas Mather. Sulfonated block copolymers having acrylic esterand methacrylic ester interior blocks, and various uses for such blocks, and various uses for such block copolymers, July 2011. U.S. Classification 525/330.4, 525/315, 526/329, 525/313, 526/329.7, 526/328, 526/329.2, 525/316, 526/319, 525/333.5, 526/328.5, 525/314, 525/330.3, 526/287, 525/291; International Classification C08F8/34; Cooperative Classification Y10T428/31855, Y10T442/387, Y10T442/668, Y10T428/31931, Y10T442/678, Y10T442/3886, Y10T442/3976, Y10T442/20, Y10T428/249921, Y10T442/676, Y10T428/31938, Y02E60/522, C08F8/36, B01D71/80, Y02E60/523, H01M4/661, B01D71/26, Y02E60/122, H01M4/131, H01M2004/027, A61F2013/530489,

H01M2/1633, B01D71/40, B01D71/28, B01D69/10, B01D71/82; European Classification C08F8/36, B01D71/80, H01M2/16B5, H01M4/66A, B01D69/10, B01D71/82, H01M4/131.

[87] Christopher J. Ellison, Manish K. Mundra, and John M. Torkelson. Impacts of Polystyrene Molecular Weight and Modification to the Repeat Unit Structure on the Glass Transition-Nanoconfinement Effect and the Cooperativity Length Scale. *Macromolecules*, 38(5):1767–1778, March 2005.

[88] A. C. Puleo, N. Muruganandam, and D. R. Paul. Gas sorption and transport in substituted polystyrenes. *Journal of Polymer Science Part B: Polymer Physics*, 27(11):2385–2406, October 1989.

[89] Nancy C. Zhou, Christopher D. Chan, and Karen I. Winey. Reconciling STEM and X-ray Scattering Data To Determine the Nanoscale Ionic Aggregate Morphology in Sulfonated Polystyrene Ionomers. *Macromolecules*, 41(16):6134–6140, August 2008.

[90] D. R Paul. Reformulation of the solution-diffusion theory of reverse osmosis. *Journal of Membrane Science*, 241(2):371–386, October 2004.

[91] W. Richard Bowen and Hilmi Mukhtar. Characterisation and prediction of separation performance of nanofiltration membranes. *Journal of Membrane Science*, 112(2):263–274, April 1996.

[92] Gregory R. Guillen, Yinjin Pan, Minghua Li, and Eric M. V. Hoek. Preparation and Characterization of Membranes Formed by Nonsolvent Induced Phase Separation: A Review. *Industrial & Engineering Chemistry Research*, 50(7):3798–3817, April 2011.

[93] Hang Gao and Julie P. Harmon. Para-substituted polystyrenes: Stress relaxation, creep, dynamic mechanical and dielectric analyses. *Thermochimica Acta*, 284(1):85–102, July 1996.

[94] Benjamin R. Caire. Mechanical Characterization of Anion Exchange Membranes Under Controlled Environmental Conditions. Technical report, May 2015.

[95] Eda Ayse Aksoy, Burcu Akata, Nurcan Bac, and Nesrin Hasirci. Preparation and characterization of zeolite beta–polyurethane composite membranes. *Journal of Applied Polymer Science*, 104(5):3378–3387, June 2007.

[96] Mark G. Allen, Mehran Mehregany, Roger T. Howe, and Stephen D. Senturia. Microfabricated structures for the insitu measurement of residual stress, Young's modulus, and ultimate strain of thin films. *Applied Physics Letters*, 51(4):241–243, July 1987.

[97] Jun Young Chung, Jung-Hyun Lee, Kathryn L. Beers, and Christopher M. Stafford. Stiffness, Strength, and Ductility of Nanoscale Thin Films and Membranes: A Combined Wrinkling-Cracking Methodology. *Nano Letters*, 11(8):3361–3365, August 2011.

[98] Ganpat J. Dahe, Rohit S. Teotia, and Jayesh R. Bellare. The role of zeolite nanoparticles additive on morphology, mechanical properties and performance of polysulfone hollow fiber membranes. *Chemical Engineering Journal*, 197:398–406, July 2012.

[99] Yilun Liu and Xi Chen. High permeability and salt rejection reverse osmosis by a zeolite nano-membrane. *Physical Chemistry Chemical Physics*, 15(18):6817–6824, April 2013.

[100] Cailing Lv, Yanlei Su, Yanqiang Wang, Xiaole Ma, Qiang Sun, and Zhongyi Jiang. Enhanced permeation performance of cellulose acetate ultrafiltration membrane by incorporation of Pluronic F127. *Journal of Membrane Science*, 294(1–2):68–74, May 2007.

[101] Hosam A. Shawky, So-Ryong Chae, Shihong Lin, and Mark R. Wiesner. Synthesis and characterization of a carbon nanotube/polymer nanocomposite membrane for water treatment. *Desalination*, 272(1–3):46–50, May 2011.

[102] Natalia Widjojo, Tai-Shung Chung, Martin Weber, Christian Maletzko, and Volker Warzelhan. The role of sulphonated polymer and macrovoid-free structure in the support layer for thin-film composite (TFC) forward osmosis (FO) membranes. *Journal of Membrane Science*, 383(1–2):214–223, November 2011.

[103] Qing Hua Zeng, Qing Lin Liu, Ian Broadwell, Ai Mei Zhu, Ying Xiong, and Xing Peng Tu. Anion exchange membranes based on quaternized polystyrene-block-poly(ethylene-ran-butylene)-block-polystyrene for direct methanol alkaline fuel cells. *Journal of Membrane Science*, 349(1–2):237–243, March 2010.

[104] M. E. Seitz, W. R. Burghardt, K. T. Faber, and K. R. Shull. Self-Assembly and Stress Relaxation in Acrylic Triblock Copolymer Gels. *Macromolecules*, 40(4):1218–1226, 2007.

[105] Michelle E. Seitz, Wesley R. Burghardt, and Kenneth R. Shull. Micelle Morphology and Mechanical Response of Triblock Gels. *Macromolecules*, 42(22):9133–9140, November 2009.

[106] M. E. Seitz, K. R. Shull, and K. T. Faber. Acrylic Triblock Copolymer Design for Thermoreversible Gelcasting of Ceramics: Rheological and Green Body Properties. *Journal of the American Ceramic Society*, 92(7):1519–1525, July 2009.

[107] Chya Yan Liaw, Kevin J. Henderson, Wesley R. Burghardt, Jin Wang, and Kenneth R. Shull. Micellar Morphologies of Block Copolymer Solutions near the Sphere/Cylinder Transition. *Macromolecules*, 48(1):173–183, January 2015.

[108] J. E. Enderby and D. M. North. Percus-Yevick Structure Factors for Liquid Alloys. *Physics and Chemistry of Liquids*, 1(1):1–11, January 1968.

[109] J. Ilavsky and P. R. Jemian. Irena: tool suite for modeling and analysis of small-angle scattering. *Journal of Applied Crystallography*, 42(2):347–353, April 2009.

[110] Jianqi Zhang, Dorthe Posselt, Detlef-M. Smilgies, Jan Perlich, Konstantinos Kyriakos, Sebastian Jaksch, and Christine M. Papadakis. Lamellar Diblock Copolymer Thin Films during Solvent Vapor Annealing Studied by GISAXS: Different Behavior of Parallel and Perpendicular Lamellae. *Macromolecules*, 47(16):5711–5718, August 2014.

[111] David J. Kinning and Edwin L. Thomas. Hard-sphere interactions between spherical domains in diblock copolymers. *Macromolecules*, 17(9):1712–1718, September 1984.

[112] Kenneth P. Mineart, Byeongdu Lee, and Richard J. Spontak. A Solvent-Vapor Approach toward the Control of Block Ionomer Morphologies. *Macromolecules*, 49(8):3126–3137, April 2016.

[113] Shichen Dou and Ralph H. Colby. Charge density effects in salt-free polyelectrolyte solution rheology. *Journal of Polymer Science Part B: Polymer Physics*, 44(14):2001–2013, July 2006.

[114] Evan Spruijt, Martien A. Cohen Stuart, and Jasper van der Gucht. Linear Viscoelasticity of Polyelectrolyte Complex Coacervates. *Macromolecules*, 46(4):1633–1641, February 2013.

[115] Kazi Sadman, Qifeng Wang, Shawn H. Chen, David E. Delgado, and Kenneth R. Shull. pH-Controlled Electrochemical Deposition of Polyelectrolyte Complex Films. *Langmuir*, 33(8):1834–1844, February 2017.

[116] Qifeng Wang and Joseph B. Schlenoff. The Polyelectrolyte Complex/Coacervate Continuum. *Macromolecules*, 47(9):3108–3116, May 2014.

[117] S. Förster and M. Schmidt. Polyelectrolytes in solution. In *Physical Properties of Polymers*, Advances in Polymer Science, pages 51–133. Springer, Berlin, Heidelberg, 1995.

[118] Herbert Dautzenberg. Polyelectrolyte Complex Formation in Highly Aggregating Systems. 1. Effect of Salt: Polyelectrolyte Complex Formation in the Presence of NaCl. *Macromolecules*, 30(25):7810–7815, December 1997.

[119] D. Rout, R. Verma, and S. K. Agarwal. Polyelectrolyte treatment – an approach for water quality improvement. *Water Science and Technology*, 40(2):137–141, July 1999.

[120] Soheil Boddohi, Nicholas Moore, Patrick A. Johnson, and Matt J. Kipper. Polysaccharide-Based Polyelectrolyte Complex Nanoparticles from Chitosan, Heparin, and Hyaluronan. *Biomacromolecules*, 10(6):1402–1409, June 2009.

[121] Heide-Marie Buchhammer, Mandy Mende, and Marina Oelmann. Formation of monosized polyelectrolyte complex dispersions: effects of polymer structure, concentration and mixing conditions. *Colloids and Surfaces A: Physicochemical and Engineering Aspects*, 218(1–3):151–159, May 2003.

[122] Xuejian Lyu, Brandon Clark, and Amy M. Peterson. Thermal transitions in and structures of dried polyelectrolytes and polyelectrolyte complexes. *Journal of Polymer Science Part B: Polymer Physics*, 55(8):684–691, April 2017.

[123] Yalin Liu, Brian Momani, H. Henning Winter, and Sarah L. Perry. Rheological characterization of liquid-to-solid transitions in bulk polyelectrolyte complexes. *Soft Matter*, 13(40):7332–7340, 2017.

[124] Kazi Sadman, Qifeng Wang, Yaoyao Chen, Bavand Keshavarz, Zhang Jiang, and Kenneth R. Shull. Influence of Hydrophobicity on Polyelectrolyte Complexation. *Macromolecules*, 50(23):9417–9426, December 2017.

[125] J. D. Mendelsohn, C. J. Barrett, V. V. Chan, A. J. Pal, A. M. Mayes, and M. F. Rubner. Fabrication of Microporous Thin Films from Polyelectrolyte Multilayers. *Langmuir*, 16(11):5017–5023, May 2000.

[126] Jad A. Jaber and Joseph B. Schlenoff. Recent developments in the properties and applications of polyelectrolyte multilayers. *Current Opinion in Colloid & Interface Science*, 11(6):324–329, December 2006.

[127] ChengJun Sun, Georg E. Fantner, Jonathan Adams, Paul K. Hansma, and J. Herbert Waite. The role of calcium and magnesium in the concrete tubes of the sandcastle worm. *Journal of Experimental Biology*, 210(8):1481–1488, April 2007.

[128] Josias H. Hamman. Chitosan Based Polyelectrolyte Complexes as Potential Carrier Materials in Drug Delivery Systems. *Marine Drugs*, 8(4):1305–1322, April 2010.

[129] Sudhakara Rao Pattabhi, Ali M. Lehaf, Joseph B. Schlenoff, and Thomas C. S. Keller. Human mesenchymal stem cell osteoblast differentiation, ECM deposition, and biomineralization on PAH/PAA polyelectrolyte multilayers. *Journal of Biomedical Materials Research Part A*, 103(5):1818–1827, May 2015.

[130] Peter Schuetz and Frank Caruso. Multilayer thin films based on polyelectrolyte-complex nanoparticles. *Colloids and Surfaces A: Physicochemical and Engineering Aspects*, 207(1–3):33–40, July 2002.

[131] Huan Zhang, Chao Wang, Geyunjian Zhu, and Nicole S. Zacharia. Self-Healing of Bulk Polyelectrolyte Complex Material as a Function of pH and Salt. *ACS Applied Materials & Interfaces*, 8(39):26258–26265, October 2016.

[132] Samim Ali and Vivek M. Prabhu. Relaxation Behavior by Time-Salt and Time-Temperature Superpositions of Polyelectrolyte Complexes from Coacervate to Precipitate. *Gels*, 4(1):11, January 2018.

[133] Nadia Ladhari, Joseph Hemmerlé, Youssef Haikel, Jean-Claude Voegel, Pierre Schaaf, and Vincent Ball. Stability of embossed PEI-(PSS–PDADMAC)20 multilayer films versus storage time and versus a change in ionic strength. *Applied Surface Science*, 255(5, Part 1):1988–1995, December 2008.

[134] Grégory Francius, Angélina Razafitianamaharavo, Mariam Moussa, Manuel Dossot, Erwan André, Jalal Bacharouche, Bernard Senger, Vincent Ball, and Jérôme F.L. Duval. Remarkable Structure and Elasticity Relaxation Dynamics of Poly(diallyldimethylammonium chloride)–Poly(acrylic acid) Multilayer Films. *The Journal of Physical Chemistry C*, 120(10):5599–5612, March 2016.

[135] Pierre Schaaf and Joseph B. Schlenoff. Saloplastics: Processing Compact Polyelectrolyte Complexes. *Advanced Materials*, 27(15):2420–2432, April 2015.

[136] Lu Li, Samanvaya Srivastava, Marat Andreev, Amanda B. Marciel, Juan J. de Pablo, and Matthew V. Tirrell. Phase Behavior and Salt Partitioning in Polyelectrolyte Complex Coacervates. *Macromolecules*, 51(8):2988–2995, April 2018.

[137] Kristopher D. Kelly and Joseph B. Schlenoff. Spin-Coated Polyelectrolyte Coacervate Films. *ACS Applied Materials & Interfaces*, 7(25):13980–13986, July 2015.

[138] Katsuhiko Ariga, Jonathan P. Hill, and Qingmin Ji. Layer-by-layer assembly as a versatile bottom-up nanofabrication technique for exploratory research and realistic application. 9(19):2319–2340, May 2007.

[139] Tarek Farhat, Ghada Yassin, Stephan T. Dubas, and Joseph B. Schlenoff. Water and Ion Pairing in Polyelectrolyte Multilayers. *Langmuir*, 15(20):6621–6623, September 1999.

[140] Aditya Jaishankar and Gareth H. McKinley. Power-law rheology in the bulk and at the interface: quasi-properties and fractional constitutive equations. *Proc. R. Soc. A*, 469(2149):20120284, January 2013.

[141] Lele Mathis, Yaoyao Chen, and Kenneth R. Shull. Tuning the Viscoelasticity of Hydrogen-Bonded Polymeric Materials through Solvent Composition. *Macromolecules*, May 2018.

[142] Kyungjin Kim, Hao Luo, Ankit K. Singh, Ting Zhu, Samuel Graham, and Olivier N. Pierron. Environmentally Assisted Cracking in Silicon Nitride Barrier Films on Poly(ethylene terephthalate) Substrates. *ACS Applied Materials & Interfaces*, 8(40):27169–27178, October 2016.

[143] E. Cerda, K. Ravi-Chandar, and L. Mahadevan. Thin films: Wrinkling of an elastic sheet under tension. *Nature*, 419(6907):579–580, October 2002.

[144] Jun Young Chung, Adam J. Nolte, and Christopher M. Stafford. Surface Wrinkling: A Versatile Platform for Measuring Thin-Film Properties. *Advanced Materials*, 23(3):349–368, January 2011.

[145] A. L. Volynskii, S. Bazhenov, O. V. Lebedeva, and N. F. Bakeev. Mechanical buckling instability of thin coatings deposited on soft polymer substrates. *Journal of Materials Science*, 35(3):547–554, February 2000.

[146] A. L. Volynskii, D. A. Panchuk, S. V. Moiseeva, A. S. Kechek'yan, A. I. Dement'ev, L. M. Yarysheva, and N. F. Bakeev. New approach to evaluation of the stress-strain properties of nanolayers of solid materials. *Russian Chemical Bulletin*, 58(5):865–882, May 2009.

[147] Haixia Mei, Yaoyu Pang, and Rui Huang. Influence of interfacial delamination on channel cracking of elastic thin films. *International Journal of Fracture*, 148(4):331, December 2007.

[148] Jerold M Schultz. *Polymer Materials Science*. Prentice-Hall, Englewood Cliffs, N.J., 1974. OCLC: 601241.

[149] Tariq M. Malik, Pierre J. Carreau, and Nathalie Chapleau. Characterization of liquid crystalline polyester polycarbonate blends. *Polymer Engineering & Science*, 29(9):600–608, May 1989.

[150] Nathalie Chapleau, Pierre J. Carreau, Carmen Peleteiro, Paul-André Lavoie, and Tariq M. Malik. Properties of a thermotropic liquid crystalline polymer blended with different thermoplastics. *Polymer Engineering & Science*, 32(24):1876–1885, December 1992.

[151] J. C. Lötters, W. Olthuis, P. H. Veltink, and P. Bergveld. The mechanical properties of the rubber elastic polymer polydimethylsiloxane for sensor applications. *Journal of Micromechanics and Microengineering*, 7(3):145, September 1997.

[152] J. C. Lötters, W. Olthuis, P. H. Veltink, and P. Bergveld. Polydimethylsiloxane, a photocurable rubberelastic polymer used as spring material in micromechanical sensors. *Microsystem Technologies*, 3(2):64–67, February 1997.

[153] Jessamine Ng Lee, Cheolmin Park, and George M. Whitesides. Solvent Compatibility of Poly(dimethylsiloxane)-Based Microfluidic Devices. *Analytical Chemistry*, 75(23):6544–6554, December 2003.

[154] John H. Koschwanez, Robert H. Carlson, and Deirdre R. Meldrum. Thin PDMS Films Using Long Spin Times or Tert-Butyl Alcohol as a Solvent. *PLOS ONE*, 4(2):e4572, February 2009.

[155] J. W. Hutchinson and Z. Suo. Mixed Mode Cracking in Layered Materials. In John W. Hutchinson and Theodore Y. Wu, editors, *Advances in Applied Mechanics*, volume 29, pages 63–191. Elsevier, January 1991.

[156] Audrey Favache, Laure Libralesso, Pascal J. Jacques, Jean-Pierre Raskin, Christian Bailly, Bernard Nysten, and Thomas Pardoen. Fracture toughness measurement of ultra-thin hard films deposited on a polymer interlayer. *Thin Solid Films*, 550(Supplement C):464–471, January 2014.

[157] Tao Guo, Xiaolu Pang, Yeting Xi, Alex A. Volinsky, and Lijie Qiao. Externally applied stress sign and film elastic properties effects on brittle film fracture. *Philosophical Magazine*, 96(5):447–458, February 2016.

[158] R. P. Kambour. Structure and properties of crazes in polycarbonate and other glassy polymers. *Polymer*, 5:143–155, January 1964.

[159] R. P. Kambour. Stress-strain behavior of the craze. *Polymer Engineering & Science*, 8(4):281–289, October 1968.

[160] L. E. Govaert and T. A. Tervoort. Strain hardening of polycarbonate in the glassy state: Influence of temperature and molecular weight. *Journal of Polymer Science Part B: Polymer Physics*, 42(11):2041–2049, June 2004.

[161] R. P. Kambour. Stumbling upon the nature of crazes and their importance to crack toughness in glassy polymers. *Journal of Polymer Science Part B: Polymer Physics*, 37(7):626–628, April 1999.